

**Applied Magnetic Forces Enhance Nanoparticle Based Gene Delivery and
Characterize Intracellular Rheology and Transport**

Kris Iniko Ford

A dissertation submitted to the faculty of the University of North Carolina at Chapel Hill
in partial fulfillment of the requirements for the degree of Doctor of Philosophy in the
Department of Biomedical Engineering.

Chapel Hill
2013

Approved by:

Richard Superfine, Ph.D.

Rudolph Juliano, Ph.D.

Shawn Gomez, Ph.D.

Oleg Favorov, Ph.D.

Edward T. O'Brien, Ph.D.

Abstract

**KRIS I. FORD: Applied Magnetic Forces Enhance Nanoparticle Based Gene Delivery
and Characterize Intracellular Rheology and Transport
(Under the direction of Richard Superfine)**

Magnetically applied forces present the ability to manipulate paramagnetic nanoparticles for a wide variety of biomedical applications. In vivo gene delivery offers the promise of new ways to treat disease at a genetic level, but it unfortunately suffers from low efficiencies. Nanoparticles present a platform for non-viral gene therapy but delivery must be optimized to make them a viable option for treatment. This work describes how magnetic forces can be applied to paramagnetic nanoparticles to enhance the delivery of antisense oligonucleotides for correction of mRNA splicing errors. Applied oscillating forces can be used to stimulate certain endocytic pathways, which acts to more than double transfection efficiency. Once a nanoparticle enters the cell, it is surrounded by the complex intracellular environment. To understand the environment that the nanoparticle enters, intracellular rheology is probed with paramagnetic microbeads. A protocol for introducing 1 micron microbeads into cells is presented. By manipulation with 3-dimensional force microscopy, the mechanical features of the cell can be characterized. Additionally, the in vivo transport due to molecular motors is also characterized. Stall force on an intracellular 1 micron bead, caused by dynein motors, is determined. This represents the force exerted on a vesicle by the motors, as it is being transported towards the nucleus, the target of the oligonucleotide delivery.

Acknowledgements

I have truly enjoyed my years in graduate school and the time I have spent in NSRG/CISMM. Everyone I have worked with has been a pleasure to work with and know every day, and I could not have asked for a better group of individuals to be surrounded by. I have progressed personally and professionally in my time here, and a great portion of that growth is due to being around so many people that are striving to achieve excellence in their work and being inspired by their words and efforts. I cannot suitably put into words the tremendous impact this group has had on me, but I will take the lessons and the people with me everywhere I go from this point forward.

I would like to thank the committee members for their wisdom and guidance during my graduate school career. Rich, thank you for providing me an opportunity to work in NSRG during my time at UNC. You provided a wealth of scientific knowledge and expertise to me, but perhaps more importantly, you taught me how to ask the right questions and how to think about problems. Thank you for your leadership, counsel, and support that allowed me to get to this point. Tim, thanks for your all of the biology conversations that we've had over the years. Your insight has helped me to better understand the problems I have worked on, and inspired me to delve deeper into the biological systems that I am studying. Dr. Juliano, thank you for allowing me to come into your lab and learn about gene delivery at a very high level. The work in your lab

was something that I was very interested in at the beginning of my time here and the opportunity to learn about it first hand was truly incredible. Dr. Gomez, thank you for your time and insight, and for helping me to get organized in the process of fulfilling my requirements. Dr. Favorov, thank you for your time and contributions to my dissertation and defense, and for the support you have given me as a teacher and BME adviser.

I would like to thank the funding agencies who have helped to support me during my time at UNC, making my studies here possible. I would like to thank the National Institutes of Health for funding my research project. I would like to thank the UNC Board of Governors for providing funding during my first year. Additionally I would like to thank the Carolina Center of Cancer Nanotechnology excellence for funding several years of my research. I would also like to thank the Initiative for Maximizing Student Diversity at UNC Chapel Hill for several years of support during my graduate career.

All of the members of NSRG have contributed to my success as a graduate student. To Lamar Mair, I enjoyed working together on the projects we shared and I enjoyed our conversations and having you as a friend. To Jeremy Cribb, thanks for all of the work you put into the MATLAB programs that make so much of everyone's work possible and for all the assistance and answered questions as a post-doc. To Luke Osborne, thanks for being a friend, for all of our conversations (scientific and otherwise), and for the UNC basketball games for which you managed to acquire tickets. To Jerome Carpenter, thanks for being a friend during all these years and congratulations to you on your defense also. To Nathan Hudson, thanks for all of the chess and Heroclix matches, all of which were epic, and for being a good friend also. To Nadira Williams, thanks for

being a friend and bringing the pastries to the defense. To Lauren, thanks for all of the help with experiments, which made possible the completion of the dissertation and the paper. It has been really good working with you and congratulations on your own graduation. Thanks also go out to Robert Judith, Suzy Lynch, Kellie Pickler, Ben Evans, Jay Fisher, Adam Shields, Vinay Swaminathan, Briana Fiser, Ashley Estes, Cory Quammen, Joe Ping-Lin Hsiao, and David Marshburn.

Thanks also go to Leandra Vicci, for all of the electronics and magnetics wisdom you have shared with me. Thanks go to Mike Falvo, who has always offered support and counsel on research and graduate school. Thanks go to Sean Washburn who sets the bar high for our scientific rigor, and won't let us settle for anything less. Thanks go to Russ Taylor who always makes us ask difficult questions in our research and for the wide range of computer science assistance. Thanks to everyone at the Chapel Hill Analytical and Nanofabrication Laboratory (CHANL), especially Carrie Donley and Wallace Ambrose for their microscopy assistance. Special thanks go to Mike Fisher, who trained me in tissue culture and cell transfection, which became key tools in my graduate school career. Thank you for your wisdom, time, and friendship through the years.

I would like to thank the UNC Biomedical Engineering Department for the opportunity to study here and complete a Ph.D. I would like to thank all of the faculty for all of the courses and knowledge they shared with all of the students. I would like to thank all of the current and former staff for assisting me during my time here, including Nancy McKinney, Sharon Womble, Vilma Berg, and Harriet Brewer.

I would like to thank my family for all of the support and love they have given me for my entire life. Nothing I do would be possible without you. Thanks to my Mom and Dad for all of the guidance they have given me throughout the years. This work is dedicated to you and I hope to take what I have learned and make the most of all that you have invested in me. Thank you to my sister, Keisha, who has also supported me throughout the years. I love you, I truly appreciate it, and hope I can be a support for you also in your future endeavors. Thanks to my brother-in-law Joel, for the encouragement since I have been in graduate school. Finally, I would like to thank my wife Vidya, who has been there for the majority of my time in graduate school. I love you very much and I wouldn't be where I am without your love and support. Graduate school has been a challenging and rewarding time. Now that we've finished this phase, I'm ready for us to move to the next and start building towards the dreams we have shared together and reaching the goals we've set.

Table of Contents

List of Figures	xii
Chapter 1 Introduction.....	1
1.1 Thesis Statement and Contributions	1
1.2 Outline	2
Chapter 2 Paramagnetic Nanoparticle Transfection	4
2.1 Overview	4
2.2 Vector Selection	7
2.2.1 Particle Functionalization	9
2.2.2 DNA Binding Verification	9
2.2.3 DNA Binding Quantification	11
2.2.4 Polyethylenimine Properties	13
2.3 Size Dependent Nanoparticle Transfection	14
2.3.1 Permanent Magnet Array	15
2.3.2 Nanoparticle/Lipofectamine Dosage	16
2.3.3 The Sub-200nm Particles are Most Effective for Oligo Delivery	17
2.4 130nm Nanoparticle Dosage Response	19
2.4.1 Transfection	20
2.4.2 BCA Results	22
2.4.3 A 50-100nM Dosage Yields Optimal Results with Minimal Toxicity	23
2.5 Transfection with Size-Uniform 200nm Fe Post Particles	24
2.5.1 Transfection	24
2.5.2 Our Size-Uniform Nanoparticle Effectively Delivery the Antisense Oligos	25
Chapter 3 Development of an Oscillating Magnetic Field Transfection Device.....	28
3.1 Overview	28
3.2 Oscillating Magnetic Force Transfection Device	30
3.2.1 Cell Culture Holder	31
3.2.2 Magnet Geometry	32

3.2.3	Force Calibration	34
3.2.4	Rotating Magnetic Array	38
3.2.5	Frequency Calibration	39
3.2.6	Force Determination	41
Chapter 4	Transfection is Enhanced with Oscillating Magnetic Fields	48
4.1	Overview	48
4.2	Published Oscillating Field Transfections have not Revealed Mechanisms Responsible for Enhancing Effects.....	49
4.3	Protocol to Effectively Study Oscillating Force Effects.....	50
4.4	Frequency Response Experiments.....	53
4.5	Oscillating Field Transfections.....	55
4.5.1	Magnetic Field Application.....	55
4.5.2	2Hz Oscillation Produces an Increase in Relative Fluorescence Intensity of Transfected Cells.....	57
4.5.3	Frequency Response Transfection.....	58
4.5.4	Oscillating Field Enhancement is Frequency Dependent, and Peaks at 10Hz	60
Chapter 5	Oscillating Magnetic Field Transfection Enhances Specific Endocytic Pathways.....	62
5.1	Overview	62
5.2	Endocytosis Pathways	63
5.2.1	Clathrin Mediated Endocytosis	64
5.2.2	Caveolae Mediated Endocytosis.....	64
5.2.3	Macropinocytosis	65
5.2.4	Non-Caveolae/Clathrin Mediated Endocytosis	65
5.3	Experiment	66
5.4	Actin Inhibition of Transfection	66
5.4.1	Latrunculin B Dose Determination.....	67
5.4.2	Determination of Lat B Incubation Time	69
5.4.3	Expression is Restored Unless Lat B Remains in Culture Several Hours after Transfection.....	70
5.4.4	Oscillating Fields do not Enhance Transfection via Membrane Fusion.....	72

5.4.5	Actin Inhibition Results.....	74
5.5	Endocytic Pathway Inhibition	77
5.5.1	No Inhibitors were Toxic in any Samples	78
5.5.2	Endocytic Inhibition Results	79
5.5.3	Macropinocytosis is Up-Regulated by Oscillating Forces, and does not Contribute to Transfection Efficiency Without Them	82
5.5.4	Caveolae/Lipid raft Pathways Increase in Efficiency due Oscillating Forces	82
5.5.5	Clathrin-Mediated Endocytosis is not Affected by Oscillating Forces.....	83
5.5.6	Oscillating Force Enhancement is not seen without Dynamin	83
5.5.7	“No Field” and Lipofectamine Controls.....	84
5.5.8	Possible Mechanisms of Force Sensitivity: Flexing of Membrane Ruffles.....	85
5.5.9	Possible Mechanisms of Force Sensitivity: Increased and Faster Binding with Trans-membrane Proteins	90
5.5.10	Possible Mechanisms of Force Sensitivity: Improved Transport Through the Glycocalyx	92
5.5.11	Advantages to stimulating macropinocytosis and caveolae/lipid raft pathways ...	94
5.6	Conclusion.....	96
Chapter 6	<i>In vivo</i> Molecular Motor Transport and Force Response	98
6.1	Introduction	98
6.2	Intracellular Constituents.....	103
6.2.1	Actin	103
6.2.2	Microtubules.....	104
6.2.3	Intermediate Filaments	104
6.2.4	Organelles.....	105
6.3	Process of Microbead Internalization and Intracellular Fate	106
6.4	Molecular Motor Transport Experiments	108
6.4.1	1 μ m Microsphere Functionalization to Achieve Internalization	108
6.4.2	Microbeads are Tracked and Mean-Squared Displacement Can Show Driven vs. Passive Transport	111
6.4.3	3-D Isosurfaces Can Show the Position of the Microbead and Verify Internalization.....	113
6.4.4	Active Microbead Transport is Temperature Dependent	114
6.4.5	The Probability Distribution of a Diffusing Bead Shows that the Microbead Transport is Active	120

6.5	<i>in vivo</i> Motor Stalling Results in Different Microbead Displacement Phenomena.....	124
6.5.1	Case 1: The Motor Stall.....	127
6.5.2	Case 2: The Viscoelastic Response	128
6.5.3	Case 3: Direction Reversal	130
6.5.4	Case 4: Assisting Transport.....	131
6.5.5	Case 5: Breaking Through.....	133
6.5.6	Case 6: Translation.....	134
6.6	A Maximum of 6 Dynein Motors act on a Single Microbead.....	136
6.7	Conclusion.....	140
Chapter 7	Probing Intracellular Mechanics with 1mm Paramagnetic Microspheres	142
7.1	Overview	142
7.2	Mechanical Models	143
7.2.1	Springs.....	144
7.2.2	Dashpots	145
7.2.3	Kelvin-Voight Model	146
7.3	Intracellular Rheology Measurements.....	146
7.4	Cytoplasm Rheology	147
7.5	Cytoskeletal Disruption	150
7.6	Probing of the Cortical Actin of the Inner Cell Membrane	153
7.7	Conclusion.....	155
Chapter 8	Appendix.....	156
8.1	Appendix One: Instrumentation	156
8.1.1	3-Dimensional Force Microscope	156
8.1.2	Nikon Eclipse TE 2000-E.....	160
8.1.3	Environmental Microscope.....	161
8.1.4	Motorized 3DFM Stage.....	161
8.2	Appendix Two: Cell Lines	169
8.2.1	HeLa Wild Type, Luc-705 and EGFP-654.....	169
8.2.2	HeLa GFP-Actin and RFP Tubulin	170
8.3	Appendix Three: Chapter 2	173
8.3.1	Polyethylenimine/Nanoparticle Functionalization	173
8.3.2	Cell Plating	174
8.3.3	Cell Culture	174

8.3.4	Luciferase Assay	175
8.3.5	BCA Protein Assay.....	176
8.3.6	Transfection Reagent Preparation	176
8.3.7	Dose Response Reagent Preparation	177
8.3.8	Imaging/Segmentation.....	178
8.3.9	Size Uniform 200nm Fe Post Particles.....	178
8.4	Appendix Four: Chapter 4	179
8.4.1	Cell Plating	179
8.4.2	Transfection Reagent Preparation	180
8.4.3	Cell Imaging and Counting Assay.....	180
8.4.4	Oscillating Field Effects are not Due to Vibration of the Sample	185
8.5	Appendix Five: Chapter 5	186
8.5.1	Cell Plating	186
8.5.2	Transfection Reagent Preparation.....	187
8.5.3	Endocytic Pathway Inhibition	188
8.5.4	Cell Staining and Imaging	188
8.5.5	Imaging and Cell Counting	189
8.6	Appendix Six: Chapter 6	190
8.6.1	Cell Culture and Plating	190
8.6.2	1 μ m Bead Dosing and Imaging	190
	Bibliography.....	192

List of Figures

2.1 Sample micrographs of the particles	8
2.2 Schematic of a 12-well cell culture plate and 12-magnet array	10
2.3 Luciferase expression from size dependent nanoparticle transfection	13
2.4 Schematic of a 12-well cell culture plate and 4 magnets per well array.....	16
2.5 Dose response of 130nm particles	17
2.6 Images and data from size-uniform 200nm particle transfection	21
2.7 Verification of DNA Binding	23
2.8 Oligo binding per nanoparticle	26
3.1 Drawings of plate holder.....	31
3.2 1" Disk magnet calibration	33
3.3 0.25" Disk magnet calibration	36
3.4 Force vs. distance of single 0.25"magnet	37
3.5 Rotating magnet array.....	39
3.6 Frequency vs. voltage	40
3.7 Frequency vs. voltage 2	41
3.8 Rectangular magnet field calibration	41
3.9 Vertical magnetic field and gradient vs. angle.....	43
3.10 Vertical force vs. time.....	44
3.11 Horizontal magnetic field and gradient vs. angle	45
3.12 Horizontal force vs. time.....	46
4.1 Typical oscillating field transfection protocol	51
4.2 My oscillating field transfection protocol.....	52

4.3 Calibration of 1” disk magnet	54
4.4 Initial oscillating field transfection results.....	57
4.5 Transfection in 96 well plate.....	59
4.6 Frequency response data	60
5.1 Illustration of endocytosis pathways.....	63
5.2 Bright field images of Lat B treated cells	68
5.3 Lat B transfection results 1	69
5.4 Lat B transfection results 2	71
5.5 Lat B transfection schematic.....	73
5.6 Oscillating field Lat B transfection results	74
5.7 Schematic for pathway inhibition studies	77
5.8 Cell viability.....	79
5.9 Pathway inhibition controls	80
5.10 Pathway inhibition relative transfection efficiency	81
5.11 Pathway inhibition transfection efficiency	81
5.12 Buckling force of actin filaments.....	87
5.13 Schematic of possible macropinocytosis enhancement	89
5.14 Schematic of possible caveolae enhancement	91
5.15 Theoretical velocity vs. force plots	93
6.1 Process of 1 μ m microbead cellular uptake	107
6.2 Microbead SEM images.....	109
6.3 Fluorescently labeled microbead images	110
6.4 Radial displacement and MSD of microbeads.....	112

6.5 Images and Isosurfaces of fluorescent beads in cells.....	114
6.6 Temperature dependence of transport on a single microbead	116
6.7 Active transport temperature dependence.....	117
6.8 Probability distribution functions for 1-D diffusion	123
6.9 Probability distribution for 1-D diffusion	124
6.10 Typical 3DFM experiment.....	125
6.11 Motor stall example	127
6.12 Viscoelastic example	129
6.13 Direction reversal example	131
6.14 Assisted transport example	132
6.15 Break through example	133
6.16 Translation example.....	135
6.17 3DFM force calibration.....	136
6.18 Displacement and velocity vs. force	137
6.19 Max motor stall force.....	138
7.1 Schematic diagram of a spring.....	144
7.2 Schematic diagram of a dashpot	145
7.3 Schematic drawing the Kelvin-Voight model.....	146
7.4 Image of 3DFM cytoplasm rheology measurement.....	148
7.5 The elastic moduli and viscosity of 6 cells	149
7.6 The elastic moduli and viscosity of single cell	150
7.7 Images from cytoskeletal disruption	151
7.8 Data of cytoskeletal disruption	152

7.9 Probing of cortical actin from the interior of the cell	154
8.1 3DFM lid and stage.....	157
8.2 3DFM voltage signal and calibration curve.....	160
8.3 Schematic drawings of the 3DFM lid adapter	164
8.4 Stage adapter for the Olympus IX81	165
8.5 Assembly of the motorized 3DFM	166
8.6 Assembled motorized stage	166
8.7 Installation of the motorized 3DFM	168
8.8 Images to verify efficacy of fluorescent actin and tubulin transfection.....	172
8.9 Micrograph of size uniform 200nm particles.....	179
8.10 Image of Syto 82 stained cells	181
8.11 ImageJ screenshot of cell counting process	182
8.12 ImageJ screenshot of cell counting process 2	183
8.13 Images of EGFP expressing in the cell counting pipeline	184
8.14 Data from vibration effects test.....	186

Chapter 1

Introduction

Cell transfection involves the introduction of exogenous genes into a cell of interest for the purpose of affecting some aspect of the cell's gene expression. Introduction of exogenous genes is done to up-regulate the expression of a gene, knockdown expression of a gene, or correct a pre-existing genetic error. The use of magnetic nanoparticles offers the possibility of targeted localized delivery to cells and tissues. To fulfill the promise of this technology, the aspects of transport and delivery must be fully understood to be optimized for clinical applications.

1.1 Thesis Statement and Contributions

The two primary areas of focus of this dissertation involve transfection of cells using paramagnetic nanoparticles and their active transport once in the intracellular environment. The process begins with the proper selection and functionalization of nanoparticles to serve as non-viral vectors. The paramagnetic nanoparticles are loaded with genes and magnetic fields are applied to them to manipulate their transport to cells and influence their uptake into cells. I present the first data using lithographically produced size-uniform metallic nanoparticles as transfection reagents. Oscillating

magnetic fields have been shown to enhance transfection efficiency of paramagnetic nanoparticles, and I present a protocol to better study the phenomenon. I demonstrate frequency dependence and show for the first time that oscillating forces enhance transfection by stimulating certain endocytic pathways.

The second area of focus examines the active transport of a nanoparticle once it is in the intracellular environment. I present a method for introducing 1 μ m microbeads to the interior of cells. I characterize transport of microbeads by kinesin and dynein molecular motors and its temperature dependence. I present for the first time characteristic responses that occur when attempting to stall molecular motors *in vivo*. I also show for the first time the maximal force exerted by dynein motors on microbeads as it is transported towards the nucleus, a primary target for gene delivery. I will also present data on the rheology of the cell interior, which help to describe the environment that surround the nanoparticle after internalization.

1.2 Outline

This work is outlined as follows:

Chapter 2 introduces the selection and functionalization of paramagnetic nanoparticles to use as non-viral vectors. I quantify their ability to bind DNA and show their effectiveness in delivering antisense oligonucleotides to cells. I show the first time that size-uniform 200nm lithographically produced metallic nanoparticles are used as transfection reagents.

Chapter 3 details the development of a device to apply oscillating magnetic fields to nanoparticles in cell cultures. This device is designed to apply oscillating fields of varying frequencies to enhance the transfection of paramagnetic nanoparticles.

Chapter 4 presents the protocol to effectively study oscillating field effects on nanoparticle transfection. The frequency dependence on transfection efficiency is established.

Chapter 5 discusses the enhancement of transfection with oscillating forces through specific endocytic pathways. I show for the first time that certain pathways are sensitive to force stimulation and propose mechanisms to explain how the enhancement is achieved.

Chapter 6 presents the data on the active transport of microbeads after they have been internalized into cells. I characterize the displacements and velocities of microbeads transported via molecular motors. I demonstrate for the first time transport phenomena that can occur when externally applied forces are applied to transported microbeads *in vivo*. I also characterize the maximum forces applied to a microbead by dynein motors *in vivo*, which are responsible for transporting cargoes to the nucleus.

Chapter 7 describes some of the rheology data that has been collected in the midst of motor stalling experiments and descriptions of phenomena that could be of interest in future studies.

Chapter 2

Paramagnetic Nanoparticle Transfection

2.1 Overview

In this chapter I will detail the selection and functionalization of non-viral vectors for delivery of antisense oligonucleotides. I will describe the necessary considerations that go into the proper selection of vectors. Taking unmodified nanoparticles, I am able to select an appropriate moiety and conjugate it with the nanoparticle, turning it into a gene binding non-viral vector. I then characterize its binding capacity as well as its ability to release the genes after introduction into the cell culture. I show how the particles are effective for delivery to HeLa EGFP-654 for correction of splice altering mutations. I also describe a novel variety of 200nm Fe_3O_4 nanoparticles that have the unique feature of being size-uniform, a feature that is difficult to achieve for particles in that size range. This work represents the first instance in which metal evaporation onto post structures was used for the formation of released shape-defined metal particles. Also, our work represents the first use of lithographically defined particles as agents of magnetofection.

Nanoparticles can be used in biomedical research as vectors for gene delivery and as probes of intracellular rheology. Nanoparticles can be fabricated in a variety of materials, sizes, and a multiplicity of functionalizations. The proper selection of vector is a key step in any experiment, as the wrong vector can produce unfavorable or misleading results. The nanoparticle must be must be designed for the particular biomedical application in order to be successful for the chosen purpose. For gaining entry into the cell, size is a key feature in achieving entry into the cell. For gene delivery, the ability to conjugate polymers and nucleic acids is the significant feature of concern. Proper attention to these details is the beginning steps to successful non-viral vector delivery.

Paramagnetic nanoparticles offer the potential to exert control over non-viral vectors by applying a magnetic field and field gradient to the particle, focusing particles for transfection to a site of interest. Magnetofection, as it has been termed, was introduced in the early 2000's as a means to transfect a variety of cells types and show proof of concept of particle uptake in rats. (Scherer, Anton et al. 2002) The basic concept of magnetofection is this: applying a magnetic force to the particle will cause it to sediment onto the cell membrane much more quickly than would occur due to gravitational attraction. Once at the cell membrane, the nanoparticle is available to the cell for uptake though one of the several endocytosis mechanisms that are constantly active in the cell. So with the paramagnetic particle one important issue regarding the use of non-viral vectors can be solved. It is possible to use a magnet to localize the vectors to a region of interest so that they are not completely at the mercy of the *in vivo* system. The ability to do so is a function of the fields and gradients that can be produced at the site of delivery, which becomes an issue with tissues deep within the body, but at least in

theory a sufficient magnetic force can achieve this localization. So then it becomes possible to optimize delivery of the vectors to the desired cells, while minimizing the amount of vector that is lost to untargeted sites. Moreover, in the case of a deleterious drug or gene, the reagent can be localized at the site of interest, reducing unintended side effects to other cells. For example, chemotherapy to treat cancer is delivered systemically to patients, and the compounds, which target rapidly reproducing cells, target cancer cells (the intended target) as well as cells of the bone marrow, digestive tract, and hair follicles (the healthy, unintended targets). These effects produce a number of harmful side effects to the patient making the treatment often extremely difficult to undergo. Potentially, such effects could be localized to the site of the tumor, leaving healthy cells unharmed, and increasing the effectiveness in treating the tumor.

The second thing that the non-viral vector must be able to do is gain entry into the cell. A particle of sufficiently small diameter ($\sim 1\mu\text{m}$ or less) can come into contact with a cell membrane and gain entry to the lumen of the cell via endocytosis. A particle contact one of the regions of the membrane that is designed for endocytosis and becomes engulfed in a portion of the cell membrane that invaginates itself into the cell and becomes pinched off into the cytoplasm. This vesicle encapsulates the particle in what is called an early endosome. Proton pumps that were once directed to the extracellular space are now directed inwardly to the early endosome. H^+ ions from the cytoplasm are pumped into the lumen of the early endosome resulting in a lowering of the internal pH. Vesicles from the endoplasmic reticulum containing digestive enzymes merge with the endosome and this vesicle becomes a lysosome. The digestive enzymes combined with low pH, work to digest any foreign particle that has gained access to the cell interior in

this way. Any particle that is intended to act as a non-viral gene vector must be able to, at some point, escape this digestive pathway in order to effectively deliver the gene payload. If it does not, the genes to be delivered will be subject to lysosomal degradation and unable to effect the expression they are meant to produce or modify.

2.2 Vector Selection

In order to transfect cells non-virally, an appropriate vector must be chosen. At the beginning of the transfection project a wide variety of particles and sizes were considered as possible vectors. There are a number of companies that commercially produce nanoparticles. All particles are not created equal however, and there will be differences in uniformity, functionalization, and composition. Size-uniformity is ideal in particle fabrication, but difficult to achieve in particles less than 500nm. Although ideal, size-uniformity is not necessary to achieve transfection. Based on the fabrication process, nanoparticles will have differences in iron oxide percent composition, and as such will vary in magnetization. The ability for nanoparticles to bind moieties is also not the same among all varieties. For this reason a reasonably broad selection of particles is chosen to determine which types will be effective for transfection. Particles should generally be smaller than 1 micron in diameter in order to be effective for uptake into the cell. (Desai, Labhasetwar et al. 1997; Prabha, Zhou et al. 2002) Particles larger than this are generally excluded for endocytosis, with the exception being phagocytic cells.

I chose the following particles, shown in Table 2.1. Scanning electron micrographs are shown in Figure 2.1.

Brand	Size	Functionalization
Micromod Nanomag	20,50,100,130, 250nm	COOH, (1 type of 250nm made with PEI)
Spherotech	200, 510nm	COOH
Dynal Dynabeads	1 μ m	COOH
Kisker	50nm	COOH
Chemicell PolyMag	100nm	PEI

Table 2.1. Nanoparticle selection for initial transfection experiments

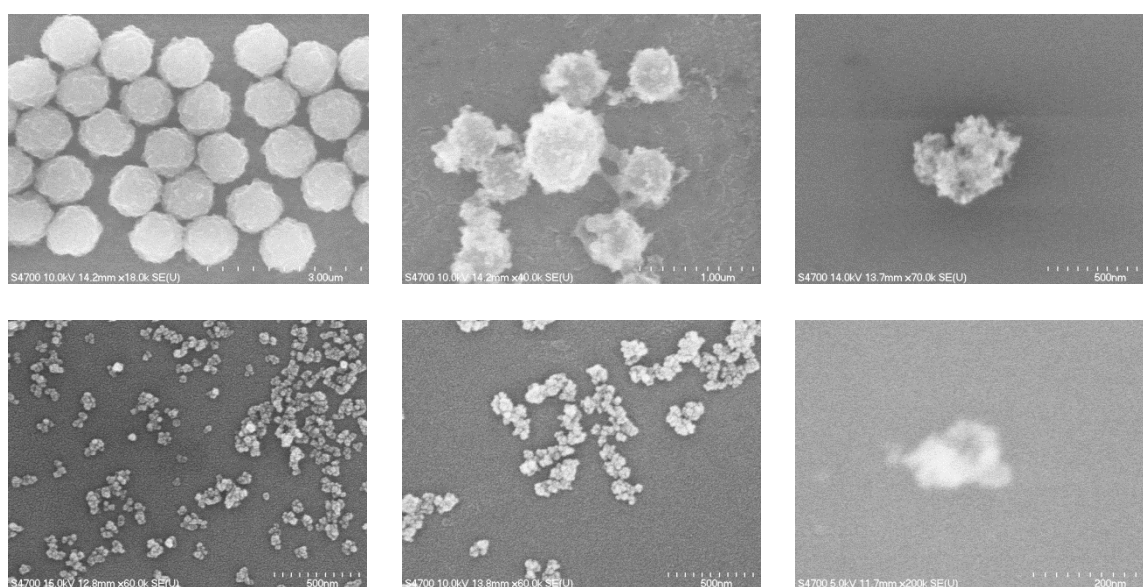


Figure 2.1 Sample micrographs of the particles used in transfection experiments. (Top Left) Dynal 1 μ m Dynabeads. (Top Middle) Spherotech 510nm. (Top Right) Micromod 250nm COOH. (Bottom Left) Micromod 250nm PEI. (Bottom Middle) Micromod 130nm. (Bottom Right) Chemicell 100nm. At the 100nm level and smaller, clear images were difficult to acquire.

Particles were selected from Invitrogen (Dynal), Micromod, Spherotech, Kisker, and Chemicell. I chose a wide selection from several companies because there is a great deal of variability in the composition and functionalization among nanoparticles. The magnetic susceptibility will vary among them, based on the size and density of iron oxide. The level of carboxyl functionalization will vary and thus will affect my ability to

bind additional moieties to the surface. The sizes ranged from 20-1000nm in diameter and were carboxyl group functionalized on the surface. The carboxyl functionalization was chosen to enable a wide variety of secondary functionalizations, such as proteins or polymers, especially with its ability to form amine bonds.

2.2.1 Particle Functionalization

In order to be effective as a non-viral vector these particles need to be further surface functionalized with a moiety to bind DNA. Reviewing literature revealed 2 potential options for DNA binding, poly-lysine and polyethylenimine (PEI). Poly-lysine is a homopolymer consisting of the amino acid L-lysine. It has been shown to be effective as a transfection reagent and a valid option for functionalizing with a carboxyl group. PEI is also shown to be effective as a transfection reagent. (Boussif, Lezoualch et al. 1995) PEI also has the additional feature of helping a so-coated particle to escape the lysosomal degradative pathway. (Akinc, Thomas et al. 2005) PEI was chosen as the polymer of choice because of this feature. The nanoparticles were functionalized via an EDAC reaction as is described in the appendix in section 2.6.1.

2.2.2 DNA Binding Verification

To verify that PEI labeled beads were effective at binding DNA, 1 μ m MyOne microbeads were functionalized with PEI and mixed with calf thymus DNA (Invitrogen™). Twenty-five μ l of 1 mg/ml MyOne beads were mixed with 50 μ l of calf thymus and rotated for 2 hours. After rotating, the beads are spun down in a centrifuge, decanted, and re-suspended in 50 μ l of MES buffer. To these beads are added 100 μ l of

Sytox Green Nucleic Acid Stain (Invitrogen™, 5mM concentration in DMSO) at a 1/1000 concentration. These beads are then washed twice and re-suspended in 50 µl of MES. Another sample of beads, without calf thymus DNA, also is mixed with Sytox Green, at similar volume and concentration. This sample is also washed twice and re-suspended in MES. The Sytox Green Nucleic Acid Stain is designed to adhere to nucleic acids and fluoresce. Beads with the DNA will fluoresce green and those without DNA will not. This is shown in Figure 2.2:

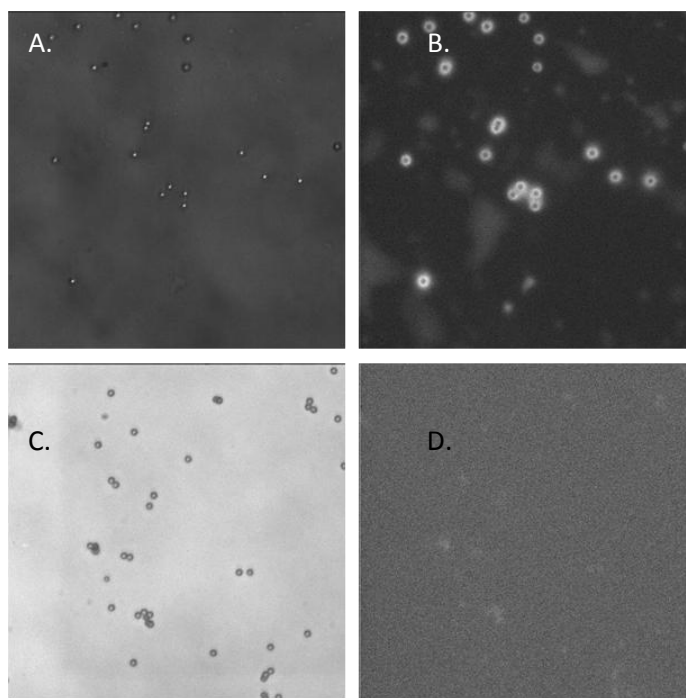


Figure 2.2 (A) Bright field image of 1µm beads functionalized with PEI, DNA, and Sytox Green. (B) Fluorescent image of same field of view as (A) verifying attachment of DNA to the beads. (C) Bright field image of 1µm beads mixed with DNA and Sytox Green. Without the PEI functionalization, no DNA is seen attached to the beads

The images on the left are bright field images taken at 100X magnification. On the right are fluorescent images taken of the exact same field of view as the bright field images. The sample of beads that were mixed with DNA show clear fluorescence localized at the beads from the nucleic acid stain. The beads without the DNA do not show any

fluorescence from the stain. This experiment verified that my protocol of binding DNA to beads was effective.

2.2.3 DNA Binding Quantification

An important question to answer regarding the efficacy of a particle for oligo delivery is the capacity of the individual particle to bind the oligo effectively. A particle is meant to enter the cytoplasm of a cell and release some portion of its payload to the cytoplasm, making it available for gene correction in the cell. The bead must bind the molecules strongly enough to remain attached while suspended in fluid, such as blood or cell culture media. On the other hand, it must not bind to them so strongly so as to prevent their release into the cell. To determine the extent to which the PEI coated particles bind the oligos, I performed a series of experiments to empirically determine the average number of oligonucleotide molecules attached to the bead and the average number released over the duration of a typical experiment. Absorbance of DNA in the electromagnetic spectrum is at a maximum for the UV wavelength. This enables the use of UV-vis spectrophotometry for measurement of DNA concentrations experimental samples. The Beer-Lambert law states that the transmission of light through a substance is logarithmically dependent on the product of the absorption coefficient of the substance and the path length of the light through the substance. This can be shown in the below equation.

$$T = \frac{I}{I_0} = e^{-\alpha l} \quad (2.1)$$

Here, I_0 and I are the intensities of the incident and transmitted light respectively, α is the absorption coefficient of the liquid, and l is the path length of the light. The absorption

coefficient of the light can be expressed as the product of the extinction coefficient (ϵ) of the absorbing molecules and their concentration (c) in solution.

$$\alpha = \epsilon c \quad (2.2)$$

Taking the log of the Beer-Lambert equation yields the quantity known as absorbance A .

$$A = -\log_{10} \frac{I}{I_0} = \epsilon lc \quad (2.3)$$

Therefore if path length and extinction coefficient are known, the concentration of the absorbing molecule can be determined.

For our studies, the oligonucleotide is provided at 5250 $\mu\text{g/mL}$ or 210 OD/mL. A sample is drawn from this stock and diluted to 50 μM . Ten μL of the 50 μM is added to 990 μL for a dilution factor 100. Theoretically this formulation should give an absorbance reading of 0.1155 on a UV spectrophotometer set to read at 260nm. From this same stock 10 μL of DNA are added to 20 and 30 μL of the magnetic particles that are at a mass density of 1 mg/ml. PBS is added to make a total volume of 260 μL and this is allowed to rotate for 1 hour. The beads are spun down in a centrifuge to separate the beads from the unattached molecules. The supernatant is removed from the spun down beads and to this is added 740 μL of TE (Tris/EDTA 10:1) buffer, making a total volume of 1ml. The beads are re-suspended in 1 mL of TE buffer and allowed to rotate for 24 hours. This re-suspension done to represent the introduction of the particle/oligo complexes being introduced cell culture media. At the end of the 24 hour period the beads are drawn down and the supernatant is removed. The fraction of oligos in the supernatant is representative of the oligos that would be released over the duration of the transfection

experiment. The original DNA formulation is measured at 260nm as a standard. The supernatant of the initial binding to the particles is measured and by subtraction with the standard formulation a determination is made of how much of the DNA has been bound to the particles. The 24 hour supernatant is measured and a determination is made of how much of the DNA is released after 24 hours. Results are shown in Figure 2.3.

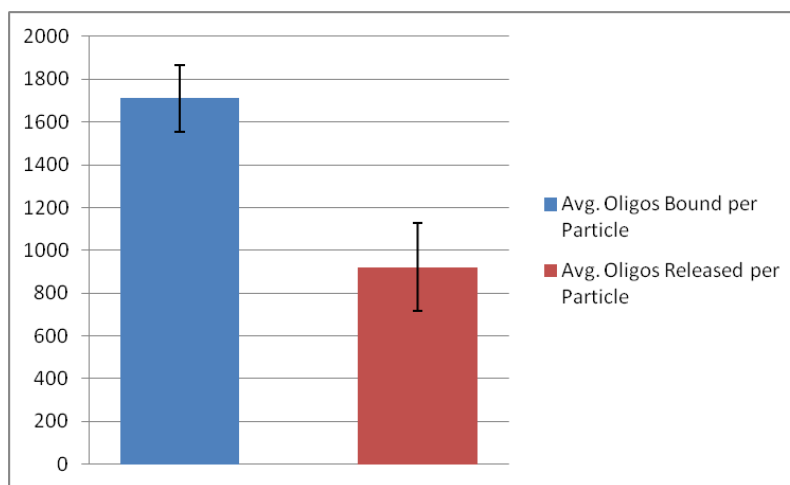


Figure 2.3 Plot of average oligos bound and released per 130nm nanoparticle

Data show that on average 1710 ± 155 (mean \pm SE) molecules were bound to a single 130nm particle, and that over a 24 hour duration, 921 ± 207 molecules were released per particle. This resulted in an average bioavailability of 52% of the oligos originally bound to the particle.

2.2.4 Polyethylenimine Properties

To achieve gene binding to the particles and effective intracellular release, the polymer polyethylenimine (PEI, 60,000 MW, Sigma Aldrich) was chosen. This substance is a highly branched polymer that has been used effectively as a transfection agent due to its ability to electrostatically bind to the sugar phosphate backbones of

nucleic acids. PEI has been also found to be one of the compounds able to escape lysosomal degradation via the so-called “proton sponge effect”. (Akinc, Thomas et al. 2005) PEI is a highly branched polymer containing amine groups able to accept H^+ ions. Because of this PEI possesses a high buffering capacity and acts as a buffering agent within the endosome. Proton pumps, which were once facing the extracellular space, are now pointed into the interior of the early endosome once the particle is fully enveloped into the endosome. The buffering capacity of the PEI, combined with the continued influx of H^+ from the proton pumps, causes the endosome to osmotically swell, to the point of rupturing the membrane. This enables the particle and genes to escape what would be inevitable degradation. This capability also makes PEI useful reagent for delivery of genes. This is not to say that PEI is without issues. In spite of its promise, this PEI has been shown to induce cytotoxicity based on in-sample concentration and polymer structure. (Kafil and Omid 2011) Modifications to polymer structure have been shown to improve cytotoxicity and improve delivery, (Kafil and Omid 2011) so properly balanced, PEI can be an incredibly useful carrier.

2.3 Size Dependent Nanoparticle Transfection

All of the particles listed in section 2.2 were used initially to determine which would be useful for transfection experiments. Chemicell PolyMag particles were acquired and were the only particles that were pre-functionalized for use as a non-viral vector. The Micromod PEI 250nm particles were used without further functionalization to their surface.

2.3.1 Permanent Magnet Array

The array of permanent magnets was constructed from the lid of a one of the 12-well cell culture plates. Twelve circular magnets of diameter $3/4$ inches and thickness of $1/32$ inches were affixed such that when placed under the 12-well plate the magnets would be underneath each well. The magnets are approximately 2 mm from the cells. The magnetic field of the magnets were measured at the centers with a F.W. Bell Model 5080 gaussmeter and was found to be 77.4 ± 3.5 mT (mean \pm SE). The magnets were measured at the z-height of the level of the cells, which is approximate 2mm. To place the gaussmeter probe into the wells of the plate, a Dremel hand tool was used to remove portions of the sides of the plate to allow access of the probe. The magnetic field at this height was found to be 18.1 ± 3.4 mT. This results in a magnetic gradient of 29.7 T/m. The array is depicted schematically in Figure 2.4.

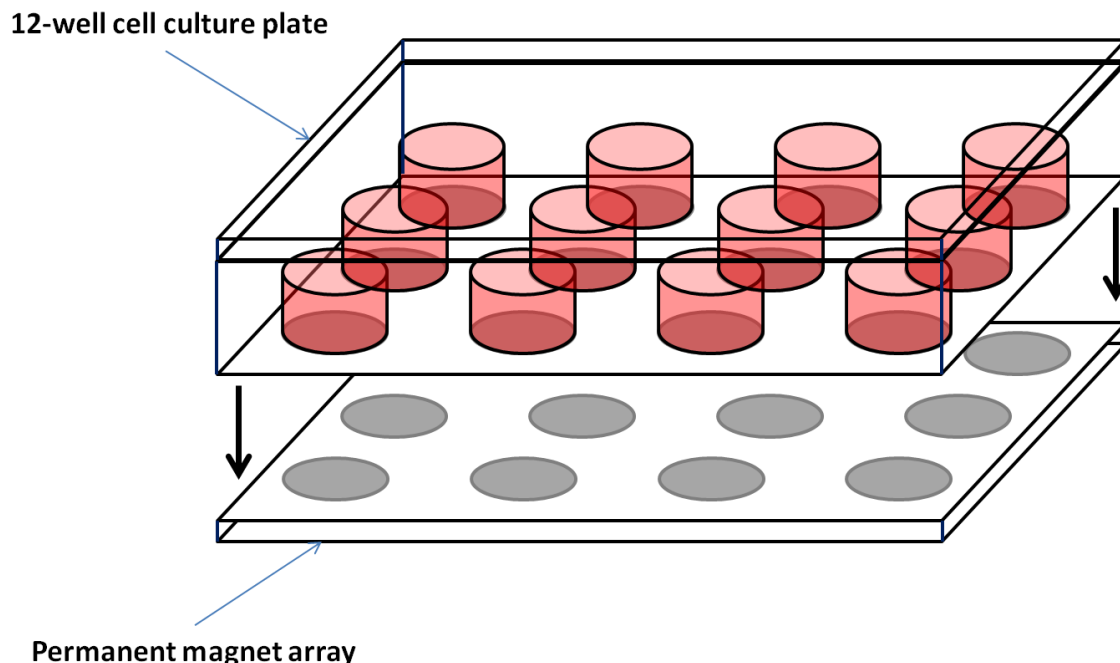


Figure 2.4 Schematic of a 12-well cell culture plate and 12-magnet array used in early transfection experiments. Modeled after commercially available kits, the magnets were approximately the same diameter as the cell culture wells.

2.3.2 Nanoparticle/Lipofectamine Dosage

A full description of the nanoparticle/oligo binding protocol is described in the appendix in sections 8.3.6. Cell culturing is described in section 8.3.2. Each well was dosed with a 500nM concentration of oligo except for the Chemicell sample which contained 250nM. The Lipofectamine 2000 sample was dosed at a 50nM concentration. This was a standard control dosage for transfection experiments as was explained during my training with Mike Fisher of the UNC pharmacology department. (Ming, Sato et al. 2011) This dosage was not meant to directly correlate to the nanoparticle dosages but to serve as a positive control for the experiment in general. The dosages and nanoparticle to oligo ratios were not optimized at the time of these experiments, but as this was an early

stage in my attempts these variables were still being fine tuned. All transfections were performed in the presence of Opti-MEM media, as described in section 8.3.2.

The first cell plate was placed over the magnetic plate and both cell plates were placed in an incubator at 37°C. The plates were placed at different ends of the incubator on separate shelves to negate the influence of the magnets on the control samples. After 4 hours media was replaced with 1 ml of DMEM and allowed to incubate for another 20 hours. The total incubation time was 24 hours. The magnets were present for the duration of the 24 hour incubation period.

2.3.3 The Sub-200nm Particles are Most Effective for Oligo Delivery

Transfection results are shown in Figure 2.5:

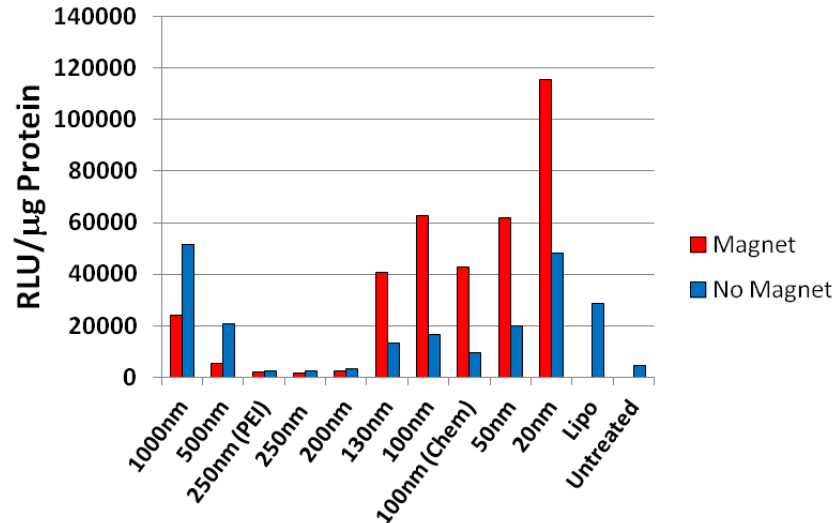


Figure 2.5 Luciferase expression from transfection of multiple nanoparticle sizes. The sub-200nm particles achieve the best delivery.

The 1 μ m and 500nm particle samples produced higher transfection rates in the non magnetic controls (magnetic samples 24086 and 5238 respectively versus non-magnetic 51400 and 20711). The reason for this is the ability of the particles of this size to sediment over the 4 hours of the transfection. The second reason would be the geometry of the magnetic plate. The magnets are roughly the diameter of the cell culture well. As they are disk magnets the regions of highest field and gradient are near the circumference of the disk. Microspheres of this size have significantly more volume than their smaller counterparts (0.53 μm^3 for 1 micron particle vs. 0.00053 μm^3 for a 100nm particle, a factor of 1000 difference) producing an increase in the $V\Delta\chi$ component of equation 3.5. This combined with the high fields and gradients would tend to draw the microspheres to the outer edge of the well preferentially, with fewer vectors going to the rest of the well. The 250nm and 200nm samples produced no transfection result whatsoever. I believed this to be due to the inability of the particles to bind with the PEI, perhaps due to issues with their carboxyl coating. The EDAC protocol worked for the other particle types so the reagents were not believed to be the cause of the failure to transfect. The 250nm PEI were not functionalized with further PEI, so it can be concluded that they are not suitable to transfect particles in their native state. The 20-130nm particle sizes all produced a promising transfection result with the greatest result occurring at the 20nm size level. This is to be expected as the 20nm particles should be the easiest particles to achieve uptake by the cell, due to their small size. As a result this is the range of particle sizes that is focused on for future transfections, to the exclusion of the others. The 1 μ m microspheres showed promise as a potential vector, particularly with modification to the

dosage and magnet geometry. However, in practical terms, as a model for potential *in vivo* application, the smaller sized particles are better suited as a vector choice.

2.4 130nm Nanoparticle Dosage Response

A dosage response is necessary to understand the optimal dose to achieve transfection. As dosage is increased it should be expected that the expression level of the target gene should also increase. There is a point at which optimal levels of expression are reached and beyond this point diminishing returns would be expected as the dosage is increased. Additionally, transfection reagents, as with any drug or compound, will become toxic in a cell culture and cells will begin to die from the exposure.

The 130nm Micromod particles were selected for usage in continuing transfection experiments based on the previous results. All of the carboxylic acid particles are functionalized with PEI via a similar protocol, however, the 130nm particles were chosen for several reasons. In the process of binding with PEI, the particles must be spun down several times with a centrifuge and re-suspended. The 130nm particles were easiest to spin down with the smaller sizes being more difficult to spin down and decant without significant loss of particles. Additionally, to characterize the oligo binding, the particles must be removed from concentration to leave unbound oligonucleotides in the supernatant. This step was difficult using the 100nm and smaller particles, so the 130nm particles became the particle of choice. It will be shown in future experiments that these particles are well suited as non-viral vectors.

2.4.1 Transfection

One cell culture dish was placed over the array of permanent magnets and the other did not receive any magnet application. This array is different than the previous array instead of a single magnet underneath the cell culture dish; this array was composed of an array of smaller magnets arrayed such that there are 4 underneath each well. They are arranged in strictly alternating polarity. This was done to increase the dispersion of the particles more evenly throughout the well. Experimental observations of particle distribution in the well due to the single larger diameter magnets confirmed that the particles did in fact sediment preferentially towards the outer perimeter of the well. This led me to use smaller magnets to produce more even delivery of the particles. It would be expected that an array of a greater number of smaller diameter magnets would produce a more even distribution of the particles, but for my purposes 4 magnets per well would be suitable. This is depicted in Figure 2.6.

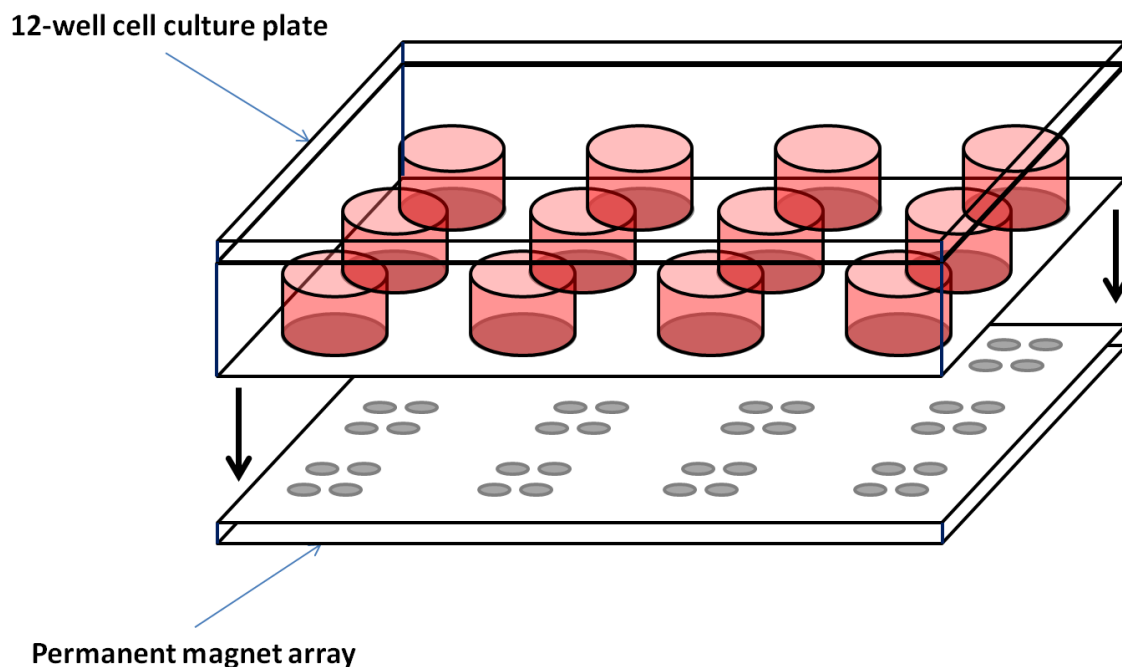


Figure 2.6 Schematic of a 12-well cell culture plate and 4 magnet array

As in the previous magnetic array, the magnets are arranged in a strictly alternating polarity.

Both 12 well plates were placed in an incubator at 37°C and 5% CO₂ for a period of 1 hour. At the end of 1 hour the magnetic plate is removed and the Opti-MEM media in both plates was replaced with DMEM with 10% FBS. After 24 hours the cells are then ready to be assayed for transfection results.

2.4.2 BCA Results

The results of the BCA test are shown in Table 2.2:

BCA Results ($\mu\text{g Protein}/\mu\text{l}$)			
Lipo 130nm Nanoparticles	Dosage	Magnet	No Magnet
	6.25 nM	3.388	2.34
	12.5 nM	3.562	3.078
	25 nM	2.762	3.055
	50 nM	2.751	NA
	75 nM	2.509	NA
	100 nM	2.875	3.061
	125 nM	1.946	1.951
	250 nM	1.461	1.794
	500 nM	1.934	1.653
	Lipofectamine 1 50 nM	NA	2.948
	Lipofectamine 2 50 nM	NA	2.661
	Lipofectamine 3 50 nM	NA	3.303
	Untreated	NA	3.297

Table 2.2. BCA Results of Dose Response. Toxicity was observed above 125nM

No significant toxicity is observed in the nanoparticle samples for the 6.25nM-100nM concentrations, based on scanning the wells through bright field microscopy. Toxicity is observed in the 125-500nM samples, as evidenced by a decreased number of healthy cells in those wells.

2.4.3 A 50-100nM Dosage Yields Optimal Results with Minimal Toxicity

The results of the nanoparticle dose response are shown in Figure 2.7.

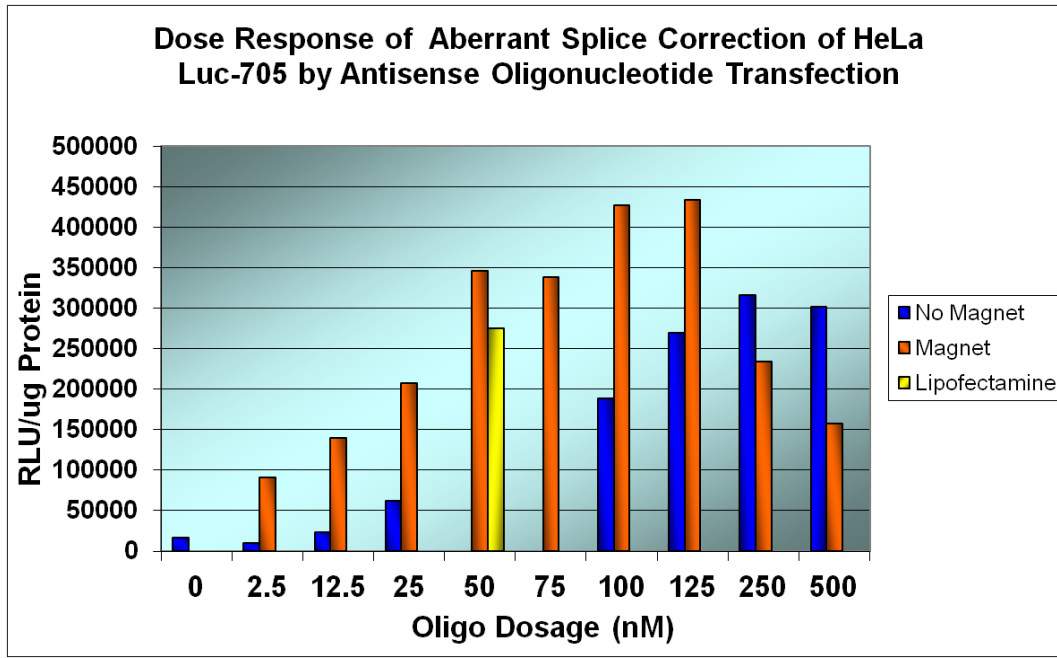


Figure 2.7 Dose response of 130nm particles. Best results were seen in the 50-100nM dosages

The data show significant Luciferase expression levels for the 2.5-125nM samples receiving the magnetic field application. All samples in this range showed significant increase in Luciferase expression over the non-magnetic controls. The greatest percent increase in transfection over the non-magnetic control is seen at the lowest concentration, 2.5nM (860.6%), and this improvement remains high for the rest of the samples but decreases monotonically with increasing dose (506% for 12.5nM, 234% for 25nM, 127% for 100nM, and 61% for 125nM). Non-magnetic controls were unfortunately not performed for the 50 and 75nM due to insufficient volume of nanoparticle reagent at the time of the experiment, although theoretical values could be interpolated based on the other data points. The 50nM magnetic treatment exceeded the expression level of the

comparable Lipofectamine dosage (345516 versus 275121 RLU/ μ g protein, a 26% improvement). For the 250 and 500 nM dosages, the no magnet controls exceeded the magnet samples. This is due to the high dosages of particles in those samples causing significant toxicity and reducing the overall transfection. The high dosage combined with the increased sedimentation by the magnets induces high levels of toxicity and is likely harsher on the cells than the non-magnetic sample. This study established the optimal dosage range for transfecting with 130nm particles. Prior experimentation was focused on establishing the capacity of various particle types to transfect the antisense oligos. This study informed for the first time the appropriate dosage to achieve expression and minimize toxicity.

2.5 Transfection with Size-Uniform 200nm Fe Post Particles

A novel type of size uniform Fe post particles was fabricated as described in section 2.6.10. This work represents the first instance in which metal evaporation onto post structures was used for the formation of released, shape-defined metal particles. This was the first use of lithographically defined particles as agents of magnetofection (Mair, Ford et al. 2009).

2.5.1 Transfection

The cells were treated for 1 hour with a 200 nM dose of antisense ODN complexed with 200 nm Fe nanoparticles with and without a permanent magnetic field. Control experiments were performed using untreated and Lipofectamine treated (no particles) HeLa EGFP-654 cells in order to compare the efficacy of gene transfection using these particles. Also, in order to assess the differences between free-floating PEI-ODN complex and particle and Lipofectamine transfections, PEI (50% w/w, 60,000 MW) was

diluted 1:5000 and conjugated with the antisense oligonucleotide. It was also added to the cell culture at 200 nM and allowed to incubate for 1 hour, at which time the media was replaced with fresh media. For magnetic nanoparticle transfections one sample was placed over the NdFeB magnets for 1 hour and a second sample did not receive an external magnetic field. The media was changed in all samples to D-MEM F-12 with 10% FBS after 1 hour. Replacing media after the field application removed free-floating ODN-laden particles from the solution, as well as any free ODN remaining in solution. The cells were incubated for an additional 23 hours before imaging. The total duration of the experiment was 24 hours. After 24 hours fluorescence microscopy was used to quantify the transfection efficacy. The imaging and segmentation process is described in section 2.6.9.

2.5.2 Our Size-Uniform Nanoparticle Effectively Delivery the Antisense Oligos

Figure 2.8 shows representative images from each treatment course along with segmentation data.

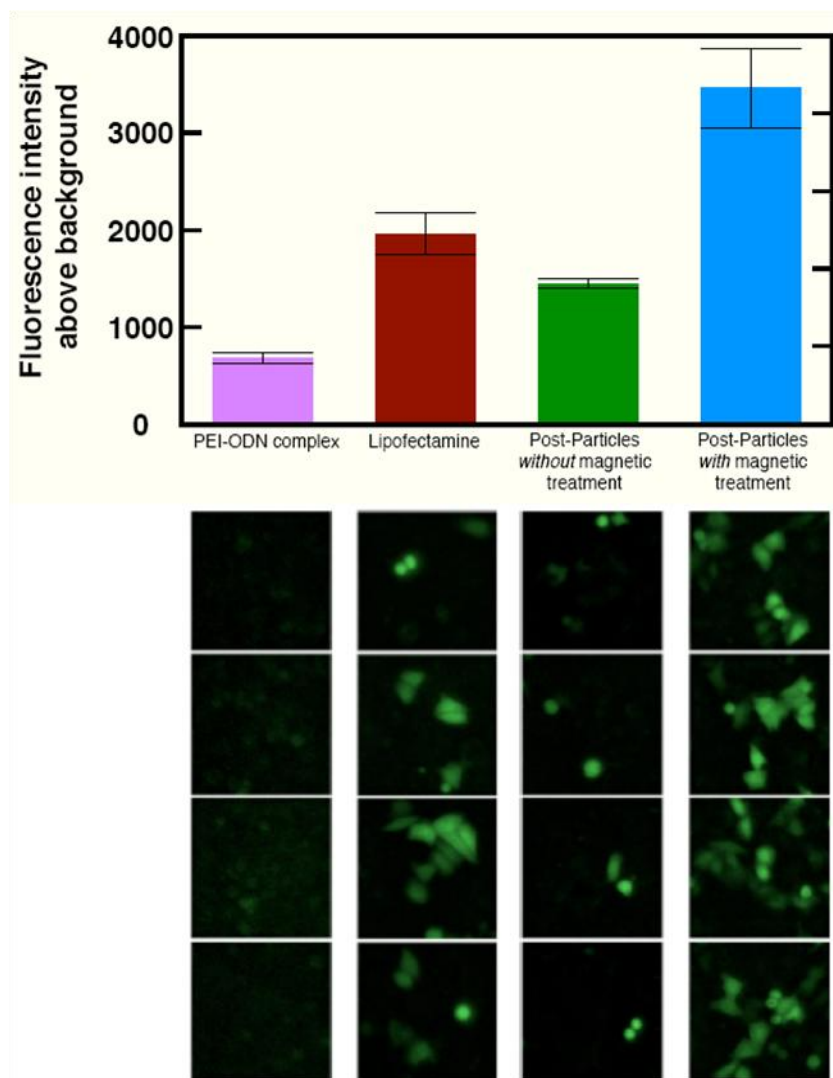


Figure 2.8 Representatives images of cells transfected with PEI-ODN, Lipofectamine, and nanoparticles with and without an applied magnetic field. Oligonucleotide concentrations were all 200 nM. Average fluorescence intensities are calculated based on image segmentation collected across the wells.

The efficacy of magnetofection using our post-particles is clearly evidenced by the increased expression of EGFP. The increased fluorescence is a product of particles penetrating the cell membrane, delivering antisense ODNs to the cell nucleus, and aberrant splicing of EGFP pre-mRNA being corrected. Results from segmentation analysis of EGFP-expressing cells indicate a 76% increase in fluorescence intensity of ODN-loaded magnetic particles (with magnetic gradient applied) over Lipofectamine as

well as a 139% increase in intensity over the non-magnetic control. Also, as evidenced by images taken throughout the well, the rate of transfection was significantly higher in the magnetic sample over the non-magnetic control. Magnetofection experiments exhibited only low levels of cell death (less than 5% overall) as observed through bright field microscopy and no evidence was seen that our particles increased cytotoxicity. However, our transfection times were 1 hour, and as such, possibly not a long enough time frame to accurately gauge toxicity levels. Toxicity experiments performed over extended periods would provide greater information regarding the comparative toxicity of our particles. Likewise, untreated HeLa EGFP-654 cells were unresponsive to the applied magnetic field and showed no visible signs of increased cytotoxicity during the experiment. It has been noted previously that an applied magnetic field enhances the transfection rate. The general mechanism by which this increased endocytosis is not clear. It is clear that the process of magnetofection decreases the time necessary for cell particle interactions to occur by magnetically placing the ODN-laden particles onto the cell membrane. The next phase in the evolution of this field is the use of magnetic fields to enhance delivery of non-viral vectors beyond increased sedimentation time. This is explored in the following chapters.

Chapter 3

Development of an Oscillating Magnetic Field Transfection Device

3.1 Overview

Ideally, an oscillating magnetic force system should apply forces in a uniform fashion across the cell culture dish. It should also be able to probe a significant range of frequencies in order to adequately study frequency dependence. A commercially available oscillating magnetic field system exists that has been used in several published studies of how oscillating fields affect nanoparticle transfection. (McBain, Griesenbach et al. 2008; Pickard and Chari 2010; Jenkins, Pickard et al. 2011) Although this system has yielded enhanced nanoparticle transfections, it is limited in the frequency and amplitude of the oscillation it can probe, which limits its effectiveness. It is also unable to apply uniform forces across the entire cell culture dish, which means that only a subset of the cell culture receives the maximum force application. It is limited in frequency range, and is only able to probe 1-5Hz. A better testing range would incorporate a more logarithmic scale, for instance 1, 10, and 100Hz. This gives a more thorough examination of any frequency dependence that may exist. In this chapter I will describe the design of my

own oscillating magnetic force device. My first iteration was modeled after the commercially available device as I attempted to improve upon its design. This device produced the initial results presented in section 4.5.2. My second iteration sought to improve upon this, and was designed to produce uniform forces across the well and the desired higher frequency range. This device produced all of the transfection results after section 4.5.2.

To design a platform to test the effects of alternating fields on non-viral magnetic particle transfection, a crucial factor in the design is the distance of the magnets from the cell culture. The magnetic force exerted on a paramagnetic bead is governed by the equation:

$$F = \frac{\pi d^3}{4\mu_0} \left\{ \frac{\mu_r - 1}{\mu_r + 2} \right\} \nabla(B^2) \quad (3.1)$$

where F is force, d is the diameter of the bead, μ_0 is the permeability of free space (in SI units), μ_r is the relative permeability of the bead, and B is the magnetic field. A bead's permeability is related to its susceptibility by the equation:

$$\mu_r = \mu_0(1 + \chi_v) \quad (3.2)$$

where χ_v is the volumetric susceptibility of the bead. According to equation 3.1, there are 3 ways to increase the force on a particle. First, the diameter of the bead can be increased. A greater diameter will result in a greater volume, and therefore more magnetic material to respond to an external magnetic field. Microbeads can be produced to be tens of microns in diameter; however beads on this size scale would be ineffective for gene delivery. Their size will exclude them from entry into the cell. Beads or particles for drug delivery are typically sub-micron in diameter. Secondly, the relative

permeability of the particle can be adjusted to increase force. This is done by adjusting the material composition of the particles. As the relative permeability μ_r increases, the limit of the quantity $\frac{\mu_r-1}{\mu_r+2}$ increases asymptotically to 1, placing an upper bound on the contribution permeability makes to the overall force. Lastly the force is dependent upon the field and field gradient. In order to apply a force to a paramagnetic particle a magnetic field alone is not sufficient to induce translational motion a field gradient must also be present. To achieve this, the magnet must be placed in closest practical proximity to the sample in order to be in the region of highest gradient.

The importance of distance from the magnetic pole can be shown in the equation:

$$\nabla(B^2) = \frac{-4B^2}{r^5} \quad (3.3)$$

where r is the distance between the magnetic pole and the bead. The force on a bead decays by a factor of $1/r^5$ so the distance between pole and sample is one of the primary factors when designing such a system.

3.2 Oscillating Magnetic Force Transfection Device

I designed a device to apply oscillating magnetic fields to enhance nanoparticle transfection. It is comprised of a holder for the cell culture plate and an array of permanent magnets to be oscillated underneath the cell culture. The first magnetic array oscillates magnets laterally under the cell culture and the second one rotates the magnets. Both served to enhance transfection but for several reasons the rotating array provides a more effective treatment, for reasons that will be explained in the following sections.

3.2.1 Cell Culture Holder

To control the distance of the cell culture and the magnetic plate, I employed an XYZ translation stage. I used a Thorlabs ½” XYZ translation stage as a basis for the transfection device. A stage was designed to hold standard 6 or 12 well tissue culture dishes. It is designed to allow access to the bottom of the cell culture dish, enabling the magnets to physically contact the bottom of the wells. It is screwed into the translator stage and the distance between the dish and the magnets can be vertically adjusted with the micrometer. The micrometers have a resolution of 10 μm and the distance of the travel can be shown by the tick marks labeling the micrometer. This enables easily reproducible adjustments for z-distance between the plate and magnets, and allows us to bring the cell culture dish as close to the magnets as possible and still allow for free translation of the magnetic plate.

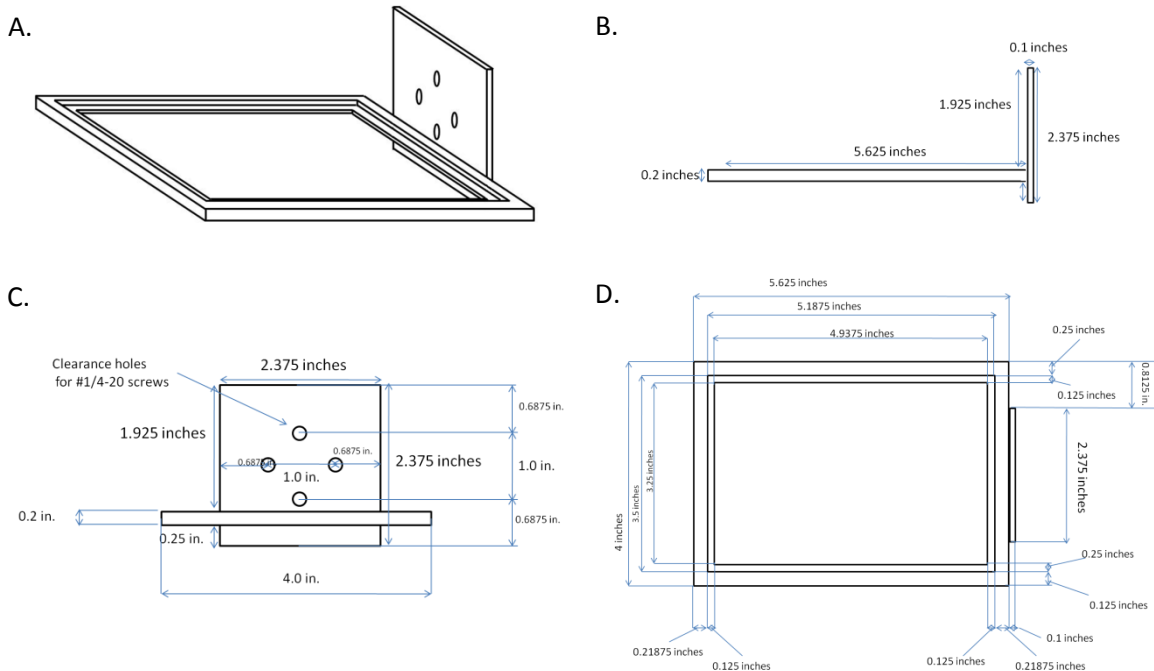
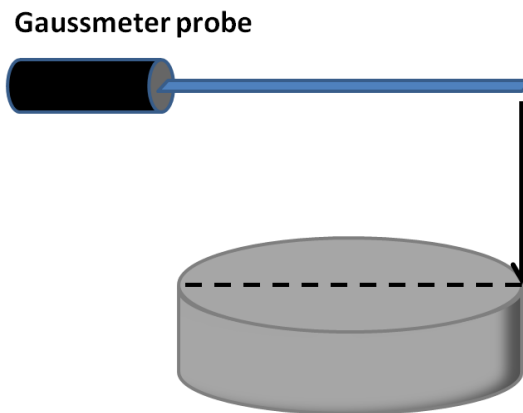


Figure 3.1 (A) Isometric view of cell culture plate holder. (B) Side view. (C) Front view. (D) Top view.

3.2.2 Magnet Geometry

The magnetic plate is composed of a lid of a standard 6-well tissue culture dish. Its similarity in size to the tissue culture plate made it a simple yet effective component for making the plate. Magnets were acquired from K and J Magnetics Inc. (Jamison, PA). The magnets chosen were axially magnetized 0.25" diameter by 0.2" height cylindrical magnets. These magnets' diameters are significantly smaller than the diameter of a 6-well (~1.4") or 12-well (~0.9") plate. These magnets are rare earth magnets composed of Neodymium, Iron, and Boron ($\text{Nd}_2\text{Fe}_{14}\text{B}$) with nickel-copper composite plating. Other commercially available magnetic plates offer plates that have a single magnet designated for a single cell culture well. For example if you desired to do a transfection in a 12-well plate, the commercial product would have a magnet of the same diameter positioned in the same conformation as the dish. Such plates are able to enhance transfection, however I contend that this is not the most favorable geometry for transfection in cell culture dishes of this size. The gradient of the cylindrical magnet is greatest around the edge of the magnet. This can be seen in the calibration of 1" disk magnet shown in Figure 3.2.



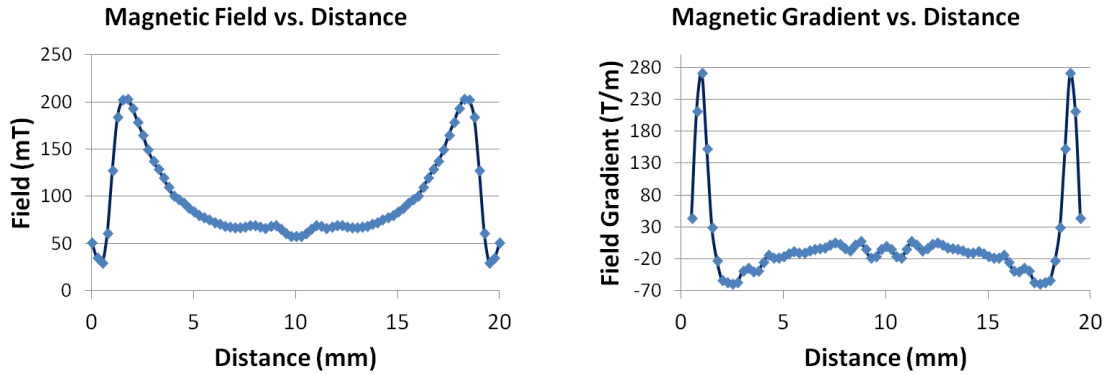


Figure 3.2 (Top) Disk magnet calibrated across the diameter. The probe is actually in contact with the surface during measurement. (Bottom Left) Magnetic field along the top surface of a 1" neodymium magnet, along the diameter. (Bottom Right) Calculation of the magnetic gradient. The biggest changes in field and gradient occur at the edges of the magnet.

Each data point is 250 μ m apart which is smaller than the reported magnet displacement of 200 μ m. While the change in gradient is relatively high at the edges of the magnet, for roughly 75% of the diameter of the magnet the change in gradient on average is only 5 T/m. Therefore, oscillating a magnet with an amplitude of 200 μ m would only produce a minimal change in force application for the majority of the cells which are not at the periphery of the magnet edge. This does not optimize the field effects. Alternately, sweeping a magnet underneath the entire cell culture will allow all of the cells to experience the full range of magnetic gradients from the maximum to zero. The oscillating effect, that is, changing the force application upon the magnetic vectors, is only optimized by applying the full range forces including the zero force range. Otherwise, the change in gradient will be orders of magnitude smaller for the majority of the cells.

If the magnet of the same diameter as the cell culture well, then the points of greatest attraction for the particles will be around the perimeter of the dish, away from the

vast majority of the cells. It stands to reason that a more favorable geometry would be composed of a series of smaller magnets arrayed over the surface of the well. This would provide for higher gradients throughout a greater percentage of the cell culture and thus higher forces applied to more particles over a greater portion of the well.

3.2.3 Force Calibration

To calibrate the forces on a particle by a magnet it is standard to mix the particles into a Newtonian fluid, and measure the velocity and calculate the force based on Stokes' law:

$$F_d = 6\pi r\eta v \quad (3.4)$$

However, the particles used in these transfection experiments are below the diffraction limit of an optical microscope (200nm). So we refer to physical laws of magnetism to give us estimations for the forces the particles experience. We do this based on the equation:

$$F = \frac{V \cdot \Delta\chi}{2\mu_0} (B \cdot \nabla) B \quad (3.5)$$

which tells us that the force on a particle depends on its volume (V), volume magnetic susceptibility ($\Delta\chi$), the permeability of free space (μ_0), the magnetic field (B), and field gradient. The particles are not perfectly spherical, but for calculation purposes, we will treat them as an idealized sphere of volume:

$$V_{sphere} = \frac{4}{3}\pi r^3 \quad (3.6)$$

The magnetization of the 130nm particles is reported by the manufacturer as 53 emu/g (electromagnetic units per gram) when $H = 1000$ Oe (Oersted). The conversion to SI units, magnetization is one to one, so this is equivalent to 53 Am²/kg (Amperes meters

squared per meter). To convert the H field, $1 \text{ Oe} = 1000/4\pi \text{ A/m}$, so then 1000 Oe is equal to $250000/\pi \text{ A/m}$. Magnetization is described mathematically by:

$$\mathbf{M} = \chi_m \mathbf{H} \quad (3.7)$$

where χ_m is the mass magnetic susceptibility and \mathbf{H} is the magnetic field. Solving for susceptibility yields:

$$\chi_m = \frac{53\pi}{250000} \frac{m^3}{kg} \quad (3.8)$$

The conversion for volumetric susceptibility is:

$$\chi_m = \frac{\chi_v}{\rho} \quad (3.9)$$

The bead density is 3.0 g/ml^3 ($3,000,000 \text{ g/m}^3$) as reported by the manufacturer. This yields a susceptibility of:

$$\chi_v = 2.0 \quad (3.10)$$

In order to calculate the force we must also know the field and the field gradient of the applied magnetic field. To do this I used a F.W. Bell Model 5080 gaussmeter to measure the field at $250 \mu\text{m}$ increments from the face of the magnet. A plot of the magnetic field vs. distance is shown in Figure 3.3:

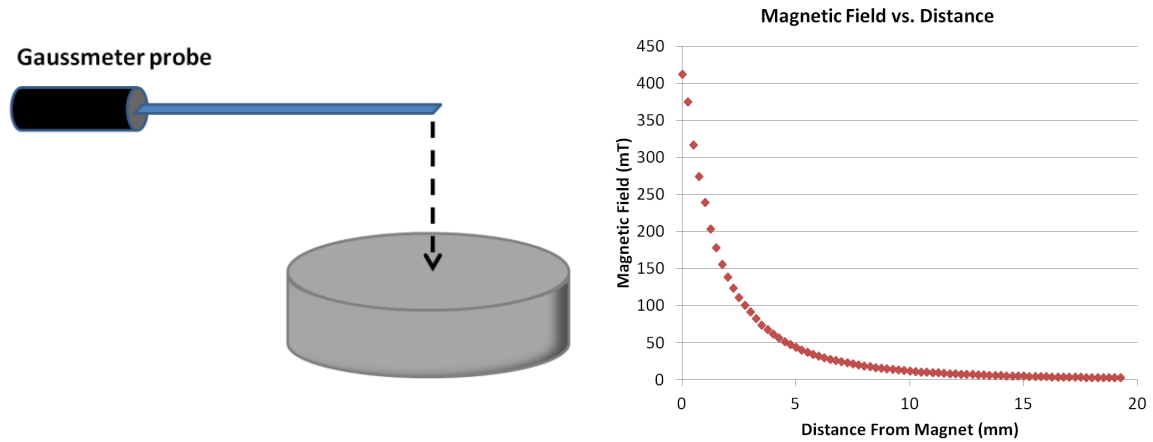


Figure 3.3 (Left) Magnetic field is measured from the center of the disk magnet. (Right) Field vs. distance of single 0.25" diameter by 0.2" height cylindrical magnets

Taking the particle to be an idealized sphere of radius 65nm yields a volume of $1.15 \times 10^{-21} \text{ m}^3$. To calculate the gradient we use a five point stencil method:

$$f'(x) \approx \frac{-f(x + 2h) + 8f(x + h) - 8f(x - h) + f(x - 2h)}{12h} \quad (3.11)$$

The permeability of free space $\mu_0 = 4\pi \times 10^{-7} \text{ V}\cdot\text{s}/(\text{A}\cdot\text{m})$. The theoretical force is then calculated and shown below.

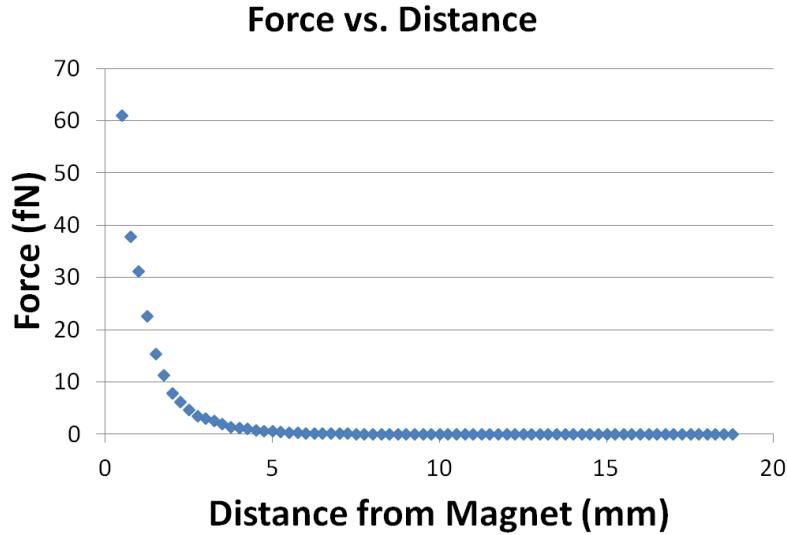


Figure 3.4 Force vs. distance of single 0.25" diameter by 0.2" height cylindrical magnets.

The magnets were arrayed in such a manner that an equal number of magnets would be underneath each well. For the 6-well cell culture dish, the magnetic plate had 9 equally spaced magnets arranged under each well. The magnets are positioned in alternating north/south polarity, with no two poles being similar in an adjacent left/right or up/down position.

The magnetic plate is attached to a linear induction motor to produce the oscillations in the X-Y plane. A stage was designed to screw into the motor that would hold the magnetic plate in place underneath the cell plate. The linear motor is controlled using a Wavtek Model 801 50MHz Pulse Generator. Connections are made to the motor using fully insulated 5/16" alligator clips via the 50 Ω output connector. With the device fully assembled, testing was performed to test the magnitude and frequency that the motor would drive the plate. A square wave signal was sent to the motor and the width was varied from 10 μ s to 100ms. The delay was set to 0s, and the period was adjusted from 10 μ s to 100ms. One minute of video was captured of the magnetic plate

undergoing oscillating motions while driven by the pulse generator at different settings. Video was taken using a Sony Cyber-shot® W510 digital camera. Video was captured at 30 frames per second and analyzed using Video Spot Tracker.

3.2.4 Rotating Magnetic Array

An alternate means of producing the oscillating magnetic field was produced using a rotating DC motor. Previous studies have reported enhanced transfection producing an oscillating field with a rotating magnet array. (D. Vainauska 2011) In light of the issues faced with the previous set up, this methodology proved to be a way to continue experiments without significant loss of time. The motor is connected as previously described to the Wavtek pulse generator. The magnetic array consists of 4 Neodymium block magnets arranged at 45° angles at the vertices and along the diagonals of a square. The block magnets are rectangular prism with dimensions of 1"× 1/4" × 1/2" (l×w×h). Magnets are arranged in an alternating polarity configuration. A diagram is shown in Figure 3.5 with an image and schematic of the experimental setup.

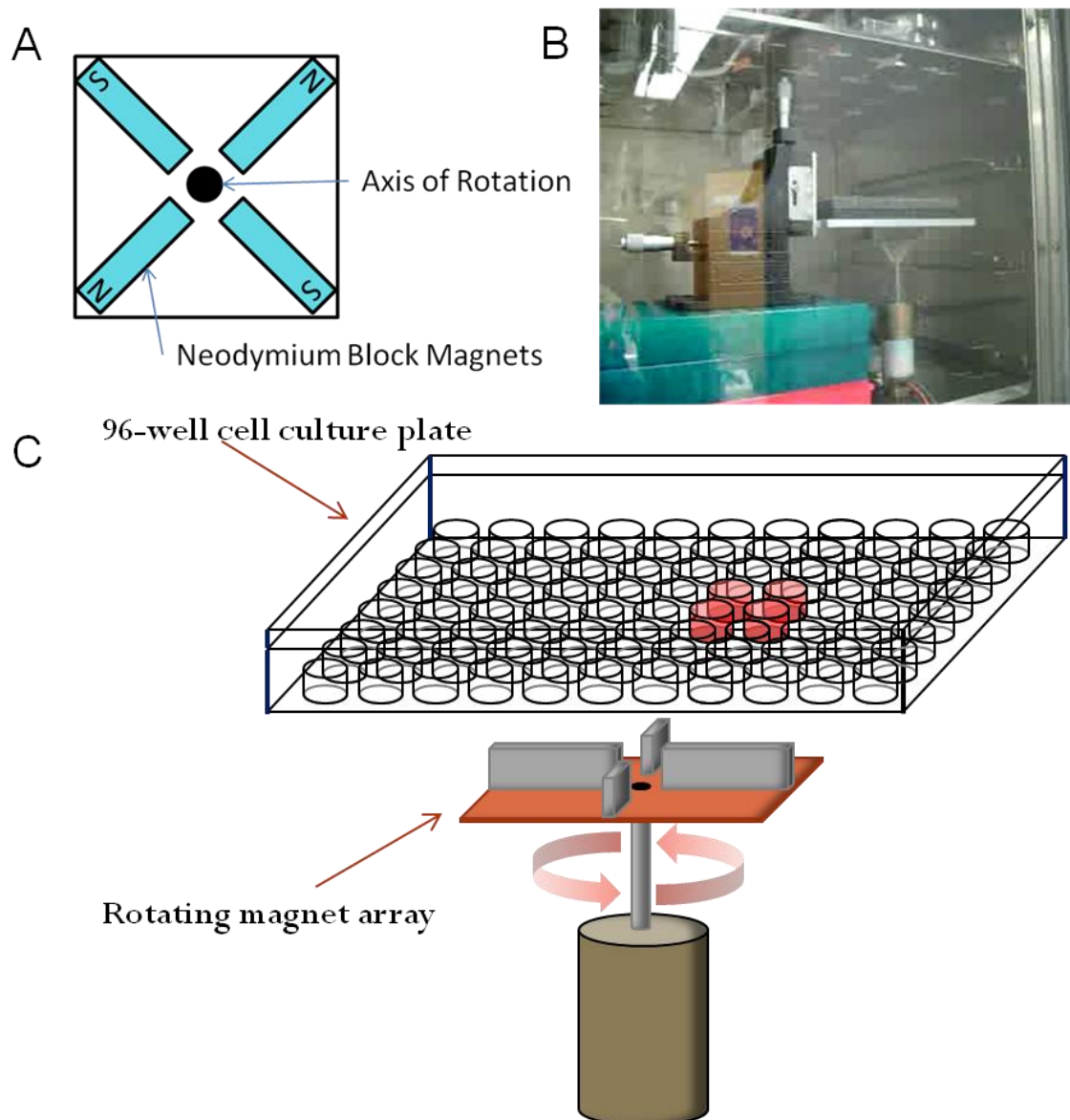


Figure 3.5 (A) Top view of magnet array (B) Image of magnetic system as it is setup in the cell culture incubator (C) Schematic of experiment in 96 well plate.

3.2.5 Frequency Calibration

The motor is driven between 8.2 and 12 volts and video is captured at 30 fps while it is operating. The video is tracked using video spot tracker. From tracking the

video, the dependence of voltage vs. rotational frequency is established. A plot of this is shown below.

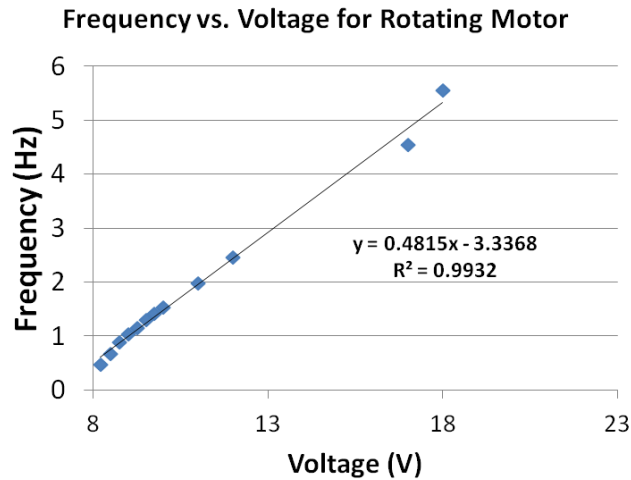


Figure 3.6 Calibration of motor to determine rotational frequency vs. voltage. Because there are 4 magnets attached to the motor, magnets actually pass under the sample at 4X the calibrated frequency.

The frequency of rotation was shown to be between 0.5Hz and 5.5Hz. Because of the positioning of the magnets the sample receives a magnetic field 4 times per rotation of the motor. Therefore the frequencies at which the magnets pass under the sample range between 2 Hz and 22Hz as shown in the Figure 3.7.

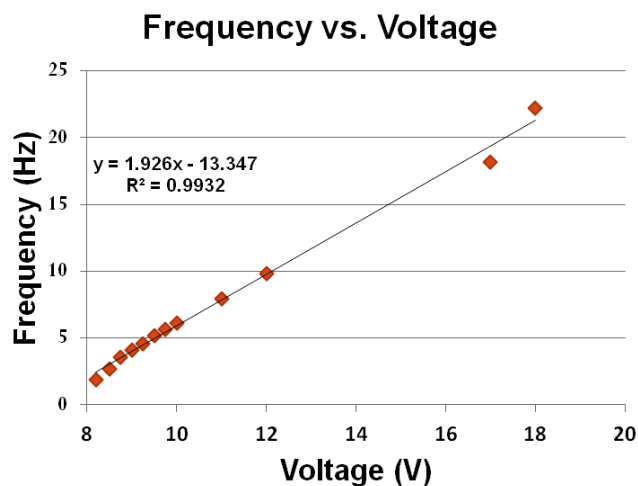


Figure 3.7 Magnet frequency vs. voltage

3.2.6 Force Determination

The magnets are calibrated with a F.W. Bell Model 5080 gaussmeter to measure the field at 250 μm increments from the face of the magnet. This gives information about the point that the particles experience the greatest z-component of the force. A plot of the magnetic field vs. distance is shown below:

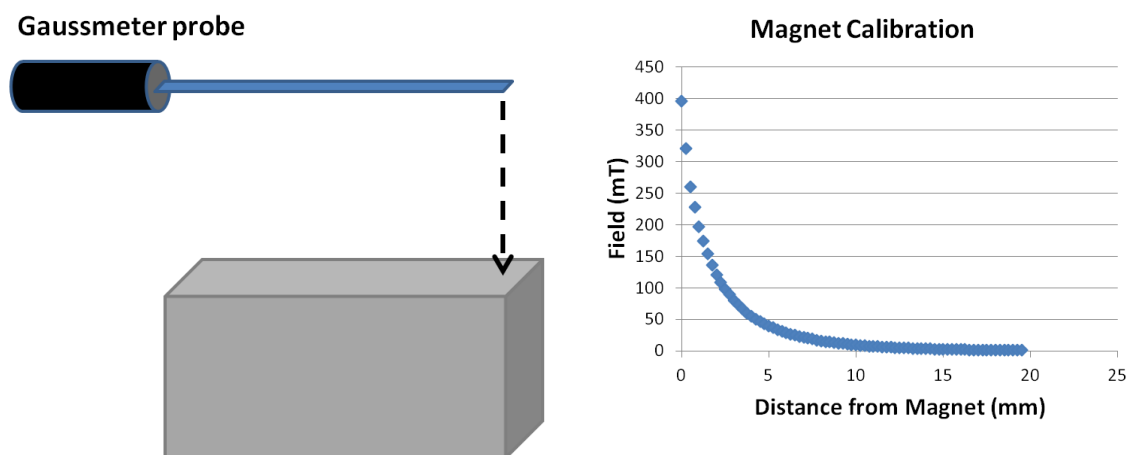


Figure 3.8 Vertical component of magnetic field of single rectangular magnet

Because of the rotation of the motor the magnetic field, force, and gradient at the sample follow a periodic wave pattern. The distance between the magnets and the underside of the cell culture dish is determined to be 0.015". This is determined by placing the magnet underneath a sample 96 well plate, and then using the micrometer to move the plate down to the magnets to the point at which the plate contacts the magnets. The Thorlabs MT3 XYZ translation stage has micrometers with tick marks that provide 0.001" resolution. The NUNC 96-well plate specifications indicate that the thickness of the polymer surface is 0.01", and therefore the sum of these measurements gives us the total of 0.025" or 6.35mm distance between the magnets and the cells.

The magnets are moving radially about the axis of the motor, so that the field at the sample has time dependence. To calibrate for this feature of the magnets must be calibrated not only in the z direction, but radially in the X-Y plane. To do this the motor is clamped to a stage at the vertex of a protractor. A small ruler is affixed to the motor, as if extending from the axis of rotation of the motor. This enables me to measure the angle of the motor as it turns about the vertex of the protractor. The gaussmeter probe is placed over the center of the magnet. The magnet is then turned at angles which are multiples of 7.5°. Following each 7.5° measurement, a second measurement is done 3° from that measurement. The field is then measured at 0°, 3°, 7.5°, 10.5°, 15°, 18° and so on through 45°. Due to the symmetry of the magnet geometry, and uniformity of the individual magnets it is clear that continuing through a full 90° or even 360° would produce results similar to the measurements made through the 45° sweep, the only difference being the alternating polarity of the magnets. Therefore for purposes of approximating the forces on the particles I take the measurements taken through 45° and extend it through the full

360°. These measurements were done at the z-height of the magnet and at a height twice the distance the magnets would be from the cells in an experiment. This was done so that a z-gradient could be calculated at the location of the cells during an experiment. Given this field and gradient is calculated as previously described. (Figure 3.9)

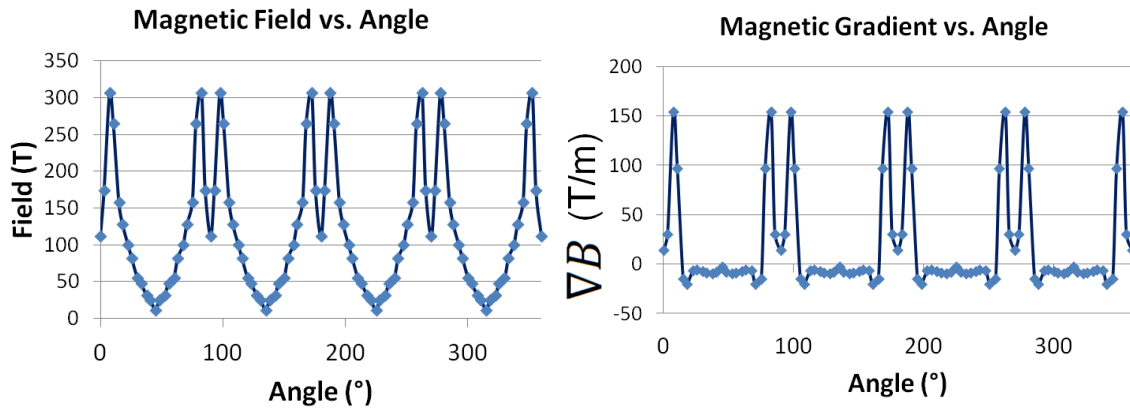


Figure 3.9 Measurements of the magnetic field vs. rotation angle. (Right) Calculation of the magnetic gradient vs. rotation angle. The two peaks are a result of high field and gradient at the top two edges of the rectangular magnet.

Force vs. time is also calculated. (Figure 3.10)

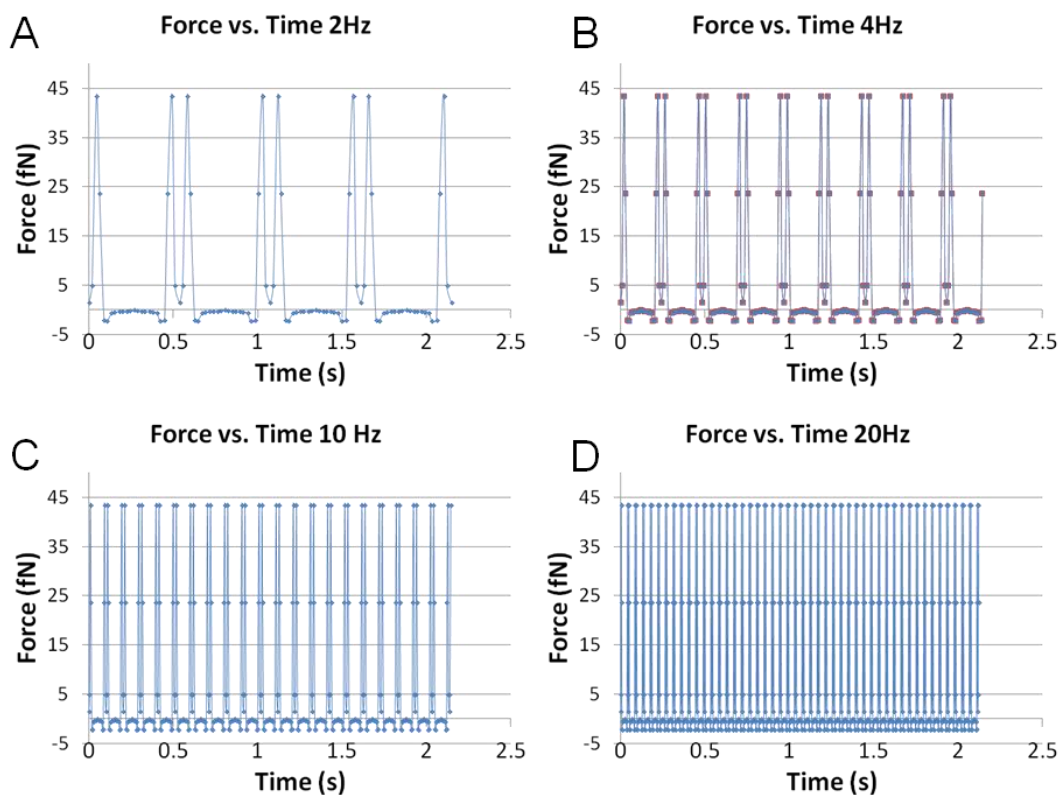


Figure 3.10 Derived vertical magnetic force vs. time. (A) 2Hz (B) 4Hz (C) 10Hz (D) 20Hz

The magnetic field gradient reached a peak of 154.8 (T/m). The point of highest gradient is of course the place where the highest force is achieved. The force on the particles due to the magnetic field and gradient reached a peak of 43.4 fN and reached a minimum of essentially zero.

The magnetic array also contributes a horizontal component of force on the X-Y plane. To calibrate this, the gauss meter probe is turned 90° to measure the horizontal component of the magnetic field. The probe is placed in contact with the magnet the closest possible distance achievable to get the sensor in range of where the cell culture would be. The motor was then rotated underneath the probe in the same manner as

described for the vertical calibration. The field is measured and the gradient is calculated and shown in Figure 3.11:

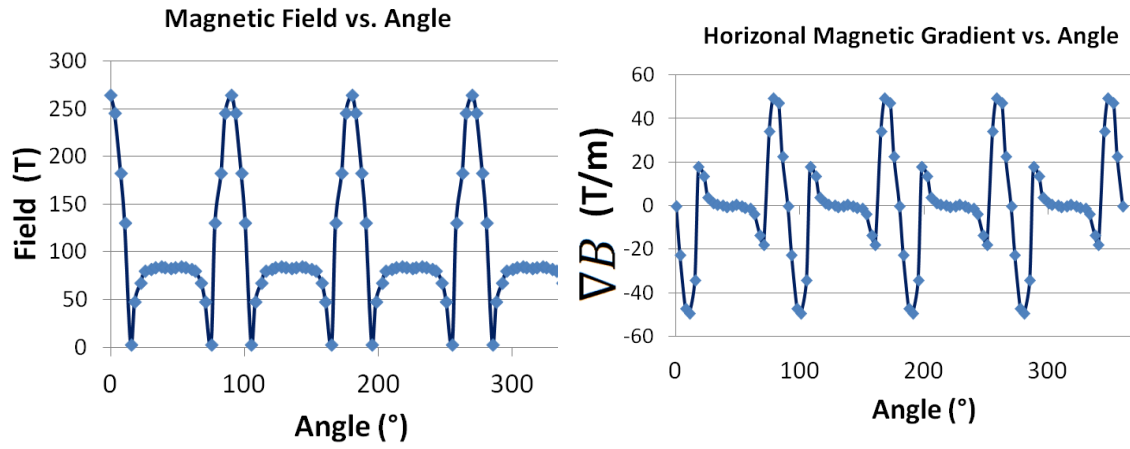


Figure 3.11 (Left) Measurements of the horizontal magnetic field vs. rotation angle. (Right) Calculation of the horizontal magnetic gradient vs. rotation angle.

The horizontal component of force is also calculated. (Figure 3.12)

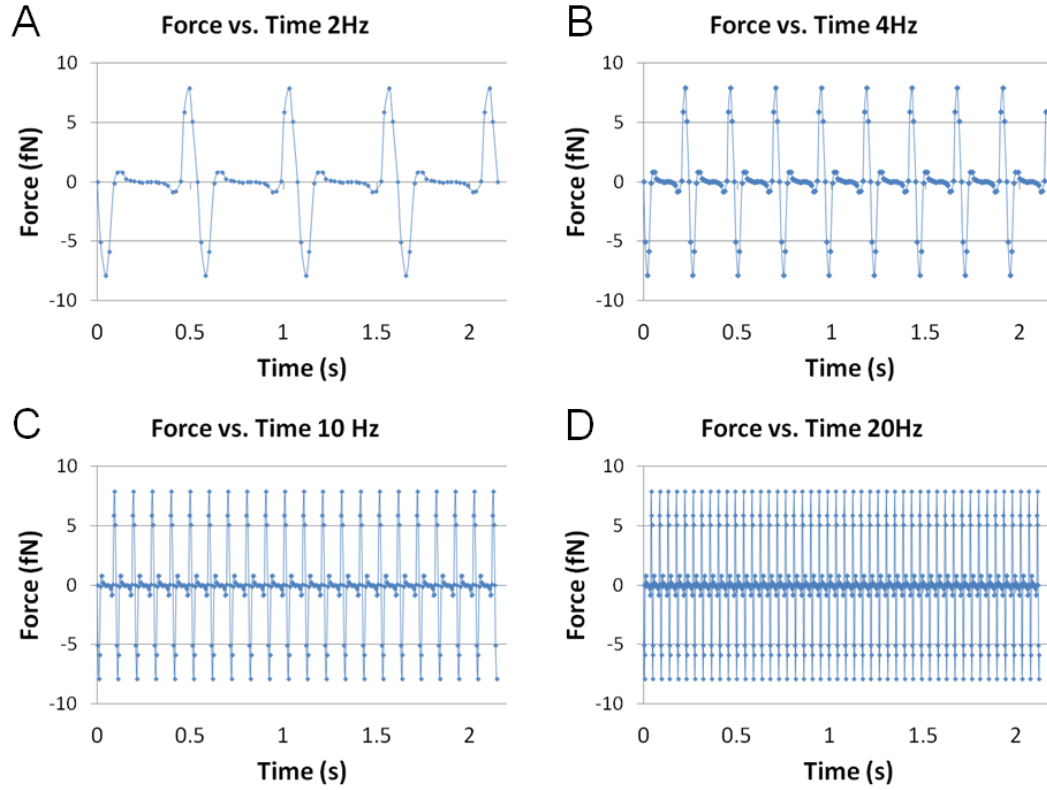


Figure 3.12 Calculated horizontal magnetic force vs. time. (A) 2Hz (B) 4Hz (C) 10Hz (D) 20Hz

The force in the XY plane reaches a maximum of 7.9 fN. The plots of force go into the negative values showing that the direction of the force reverses direction as the magnet passes over the sample. So in addition to the oscillation of force in the Z-direction, a significant component of the oscillation is also produced in the lateral direction.

To put this force regime in perspective, it can be contrasted with the force exerted on the particle due to gravity. The bead density is reported by the manufacturer as 3 g/cm³, (Teller and Grüttner 2012) which is equal to 3000000 g/m³. Treating the particle as an idealized sphere, the volume of the particle is 1.15x10⁻²¹ m³ as shown previously. The mass of the particle is the found using

$$m = \rho V \quad (3.12)$$

Where m is the mass, ρ is the density, and V is the volume. Therefore the mass is calculated to be 3.45×10^{-15} g (3.45×10^{-18} kg). The force on an object due to gravity is given by Newton's law of universal gravitation:

$$F = G \frac{m_1 \times m_2}{r^2} \quad (3.13)$$

Where G is the gravitational constant (6.674×10^{-18} N·m²·kg⁻²), m_1 is the mass of the first object (in this case the earth, 5.9742×10^{24} kg), m_2 is the mass of the second object (in this case the particle, 3.45×10^{-18} kg), and r is the distance between the centers of the 2 masses, (in this case the radius of the earth 6,378,100 m). Calculating the gravitational force yields 3.38×10^{-17} N, 3 orders of magnitude less than magnetic force.

Chapter 4

Transfection is Enhanced with Oscillating Magnetic Fields

4.1 Overview

To deliver non-viral gene vectors *in vitro* or *in vivo* there are two main aspects that must be considered once the vector is introduced into the cell culture, tissue, or organism. The first is the transport to the cells or tissue which the vectors are intended to affect. Magnetic force can be applied to paramagnetic particles to induce a velocity in the particle in the direction of the magnetic gradient. Secondly, the vector must gain entry into the cell after contacting the cell membrane. *in vivo* cell transfections suffer from low efficiencies, so in order for non-viral delivery to be a viable therapy, improvements must be made to both aspects of delivery. Oscillating magnetic fields have shown promise in their ability to enhance transfection efficiency with magnetic nanoparticle delivery to cells. The effects of oscillating forces on nanoparticle transfection are not fully understood, but must be to make non-viral delivery a viable option as a therapeutic treatment.

This chapter details the use of the oscillating magnetic field device described in chapter 3 to enhance transfection of HeLa cells. Using a range of oscillation frequencies EGFP expression levels are increased, and I show that the effect behaves like a band pass filter. How oscillating forces actually produce enhanced transfection efficiencies has been a previously unanswered question in the field. I detail a modification to published transfection protocols that allow me to better distinguish what phases of the transfection are affected by the oscillating forces, and therefore get closer to the reasons why the forces are actually beneficial.

4.2 Published Oscillating Field Transfections have not Revealed Mechanisms Responsible for Enhancing Effects

Several studies have been performed to test the effects of oscillating fields on transfection. Kamau et.al applied oscillating fields to multiple cell types to test the effects of oscillating fields on transfection. (Kamau, Hassa et al. 2006) In their study they applied a 50Hz pulse with a field and gradient and gradient of 27mT and 10 T/m. This paper showed that oscillating fields could increase the transfection efficiency for delivery of nanoparticles. Other papers have investigated the effects of oscillating fields on transfection. The same group published a paper applying pulsed magnetic fields to transfect primary cells of multiple types. (Chapman, Hassa et al. 2008) Another paper presented mixed results applying a horizontally oscillating array of permanent magnets with a frequency of 2Hz and amplitude of oscillation of only 200 μ m. (McBain, Griesenbach et al. 2008) Some data presented here showed an enhanced effect from the oscillating field, some of the data did not have an enhanced effect. Other papers have shown enhanced effects with horizontally oscillating arrays, testing frequencies between

1 and 5Hz, with a similarly low amplitude of 200 μ m. (Pickard and Chari 2010) There are other studies that have investigated this effect, but overall the number of published articles is quite low, with around 10 total papers at the time of this writing. All of these papers have shown that there exists an enhancement to transfection due to an oscillating magnetic field, but they also all contain one fundamental issue in understanding the nature of the effect. These experiments do not distinguish between the transport and post-transport phases of delivery, because there are nanoparticles still free-floating in culture during the application on the oscillating fields. While this may result in improved transfections, it does not lead to a clearer understanding of how oscillating fields improve transfection rates.

4.3 Protocol to Effectively Study Oscillating Force Effects

As mentioned before, there are in effect two components to the delivery of a gene to the cell. First the gene vector must be transported through the cell culture media to the cell membrane. The paramagnetic nanoparticles are distributed throughout the cell culture media, moving around via Brownian diffusion, eventually settling to the bottom of the well via gravitational sedimentation. This sedimentation would be considered the transport stage of transfection, which would be enhanced by a sufficient magnetic field and gradient. Secondly, there must be uptake of the vector by the cell in order to introduce the gene to the interior of the cell, where it will be available for to the intended intracellular target. In all of the papers that use oscillating magnetic fields the data reported do not distinguish between these two phenomena, making it impossible to know by what mechanism the oscillating fields are actually influencing the transfection. The typical process is depicted in Figure 4.1.

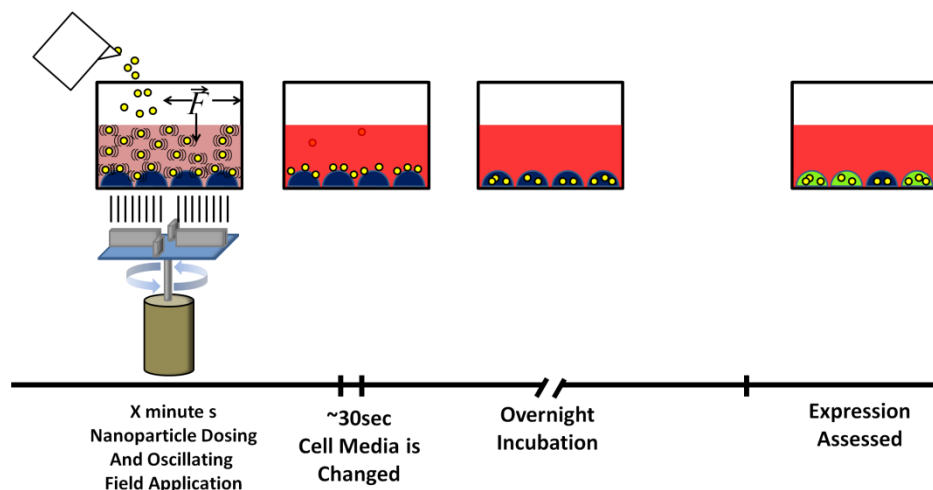


Figure 4.1 Schematic of a typical oscillating field Magnetofection experiment in literature. Oscillating fields are applied as nanoparticles are still freely floating in the cell culture, making it impossible to distinguish transport to the cell from post-transport effects.

Even in studies where both static and oscillating fields are applied, the effect is obscured because the nanoparticle containing cell culture media is not changed in between applications of the different field types. When media is not changed before application of the oscillating field, nanoparticles are still being transported to the cells from the culture media while at the same time particles are also experiencing uptake. To examine the effect of the oscillating field on the uptake cell media must be changed prior to the application of the field. My protocol is displayed graphically in Figure 4.2. All experiments are performed at 37.0°C.

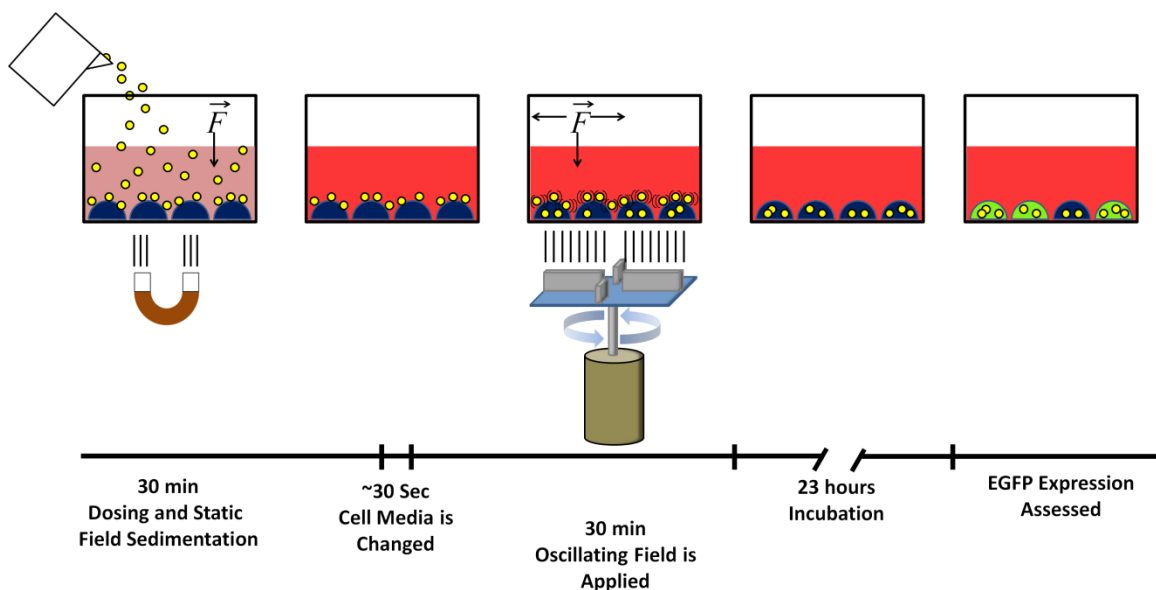


Figure 4.2a Schematic of the oscillating (AC) field transfection protocol (referred to as “Static+2Hz”, or 2Hz, 4Hz, 20Hz). 1. Oligo bearing nanoparticles are dosed into the sample and exposed to a permanent magnet for 30 minutes. 2. Cell culture media is changed to remove excess nanoparticles from solution. 3. An oscillating field is applied to the sample for an additional 30 minutes. 4. The cell culture is incubated for 23 hours. 5. Cells are imaged for EGFP expression.

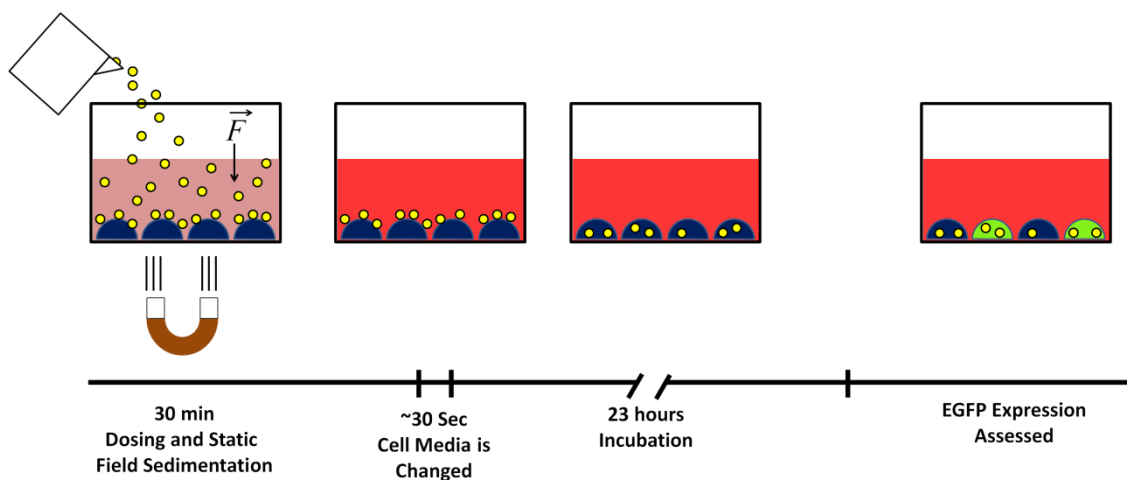


Figure 4.2b Schematic of the static field (“Static Only”) transfection protocol. 1. Oligo bearing nanoparticles are dosed into the sample and exposed to a permanent magnet for 30 minutes. 2. Cell culture media is changed to remove excess nanoparticles from solution. 3. The cell culture is incubated for 23 hours. 4. Cells are imaged for EGFP expression.

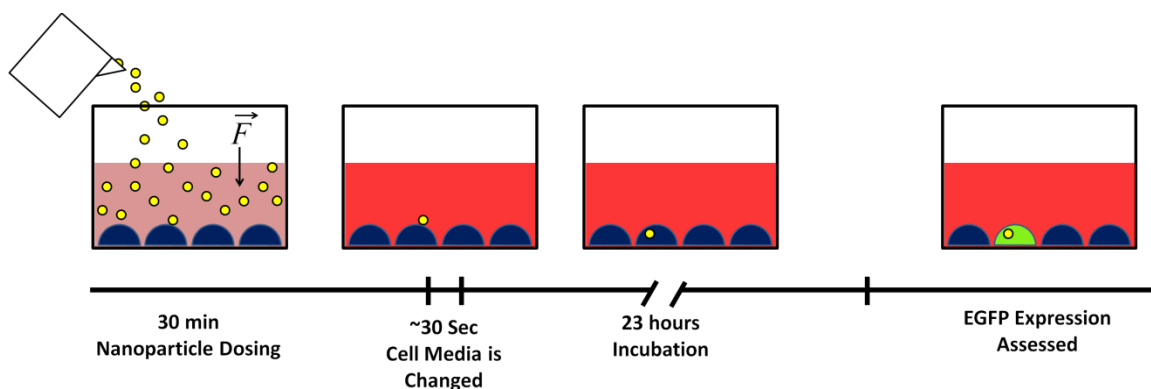


Figure 4.2c Schematic of the “No Field” transfection protocol. 1. Oligo bearing nanoparticles are dosed into the sample and incubate for 30 minutes. 2. Cell culture media is changed to remove excess nanoparticles from solution. 3. The cell culture is incubated for 23 hours. 4. Cells are imaged for EGFP expression

This simple step is not done in any of the current literature of the field and the resulting data are presented here for the first time in these experiments. These data will show definitively that the oscillating field has a distinct effect on the post-transport phase of the transfection, an effect separate from the transport, with implications for future work and *in vivo* therapeutic applications.

4.4 Frequency Response Experiments

Since an oscillating magnetic field has the effect of enhancing transfection results, then it must be the case that there is a dependence on the frequency of the oscillation. Several papers have performed frequency response studies using oscillating fields. In the Chari group papers from Keele University (Pickard and Chari 2010; Jenkins, Pickard et al. 2011) they tested the frequency effects on transfection of astrocytes and oligodendrocytes. The frequencies tested were 1, 3, and 5Hz, and 1 and 4Hz for the respective papers. These frequencies were undoubtedly chosen due to limitations of the magnetic device they were using. The nanoTherics Ltd. Website, makers of the

Magnefect nano transfection system, report that the maximum operating frequency for the system is 5 Hz. It also reports that the amplitude is 0.2mm. The problems with these limitations are two-fold. First an optimal approach for probing frequency dependence would test frequencies along a wider range, beyond 1-5Hz. The peak in efficiency may exist outside of this limited range. Secondly, the amplitude of oscillation is 0.2mm. While the 0.2mm is much larger than the average length of the cell, across the face of a cylindrical disk magnet there is not much change in the magnetic field gradient over 200 microns. This is shown by the calibration of a typical neodymium disk magnet in Figure 4.3.

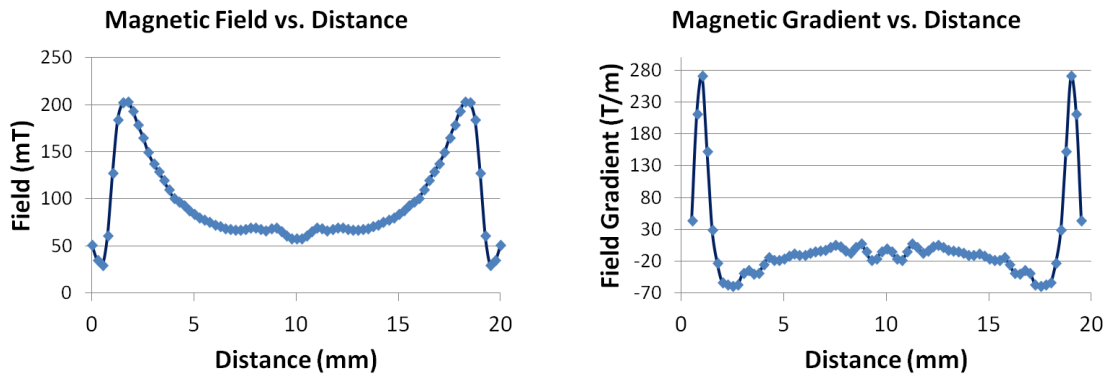


Figure 4.3 (Left) Calibration along the surface of a 1” neodymium magnet. (Right) Calculation of the magnetic gradient. The biggest changes in field and gradient occur at the edges of the magnet, so an oscillation of only 200 μ m only affects a small portion of the cell culture.

Each data point is 250 μ m apart which is smaller than the reported magnet displacement of 200 μ m. While the change in gradient is relatively high at the edges of the magnet, for roughly 75% of the diameter of the magnet the change in gradient, on average, is only 5 T/m. Therefore oscillating a magnet with an amplitude of 200 μ m would only produce a minimal change in force application for the majority of the cells which are not at the

periphery of the magnet edge. This does not optimize the field effects. Alternately, sweeping a magnet underneath the entire cell culture will allow all of the cells to experience the full range of magnetic gradients from the maximum to zero. The oscillating effect, that is, changing the force application upon the magnetic vectors, is only optimized by applying the full range forces including the zero force range. Otherwise, the change in gradient will be orders of magnitude smaller for the majority of the cells.

4.5 Oscillating Field Transfections

The oscillating field transfection experiments will be described in this section.

4.5.1 Magnetic Field Application

For the nanoparticle dosed wells, some wells receive an initial magnetic field application to sediment particles to the cell layer and some do not. After the sedimentation time, the media is changed to remove excess particles in solution. This is a key step in the study of this phenomenon that is not performed in current papers focusing on the effects of AC fields on transfection. Current published studies do not change the media in between applications of DC and AC fields. As mentioned previously, transfection is composed of two components, the transport of the vector to the cell membrane as well as the transport of the vector through the membrane. When the media is unchanged during the experiment, the line is blurred as to the effect the oscillating field is actually having in the process of transfection. If particles remain in the solution when the AC fields are applied, the fields will have an effect on continued transport of particles to the cell, as well as an effect on particles that are on the membrane and already along the endocytosis pathway. So while it is true that papers can report increased transfection

using oscillating fields, their data do not elucidate the reasons the AC field produce this effect. The reasons for these results are often only qualitatively addressed in discussion. By changing the media we focus our experiment to examine the effects of the AC fields on transport of particles through the cell membrane.

After the media is changed, some samples receive an additional DC field, AC field, or no field application. The additional fields are applied for 20 minutes. A chart depicting the samples is shown below.

Name	Vector	Dosage (nM)	10 min DC	Media changed	Additional 20 min DC field	Additional 20 min AC field
Untreated	None	0	NO	NO	NO	NO
Beads only	130nm particles	50	NO	YES	NO	NO
DC only	130nm particles	50	YES	YES	NO	NO
DC + DC	130nm particles	50	YES	YES	YES	NO
DC + AC	130nm particles	50	YES	YES	NO	YES
Lipo+623	Lipofectamine 2000	50	NO	YES	NO	NO

The magnets are oscillated horizontally underneath the cell culture plate at a frequency of approximately 2 Hz. In addition to the z-component of force due to the magnetic gradient, this oscillation produces a lateral component to the motion of the particle. It is theorized that for particles in solution this additional component promotes increased particle sedimentation although no data to this effect has been published to confirm this hypothesis. (McBain, Griesenbach et al. 2008) It is also thought that this lateral component of force the application also serves to stimulate increased particle uptake.

4.5.2 2Hz Oscillation Produces an Increase in Relative Fluorescence Intensity of Transfected Cells

To analyze the data, images were captured of the cells via fluorescence microscopy, and were segmented in Metamorph to measure the mean intensity of EGFP expression cells. We auto-threshold for light objects and adjust the threshold as needed to capture the entirety of the cells in the image. An average and standard error is calculated from 30-50 images from each sample. The data are normalized with respect to Lipofectamine. The Lipofectamine expression level is normalized to a value of 1000, and the other averages are adjusted to the same scale. The results of the first experiment are shown below. Data are reported in Figure 4.4 as mean relative intensity \pm SE.

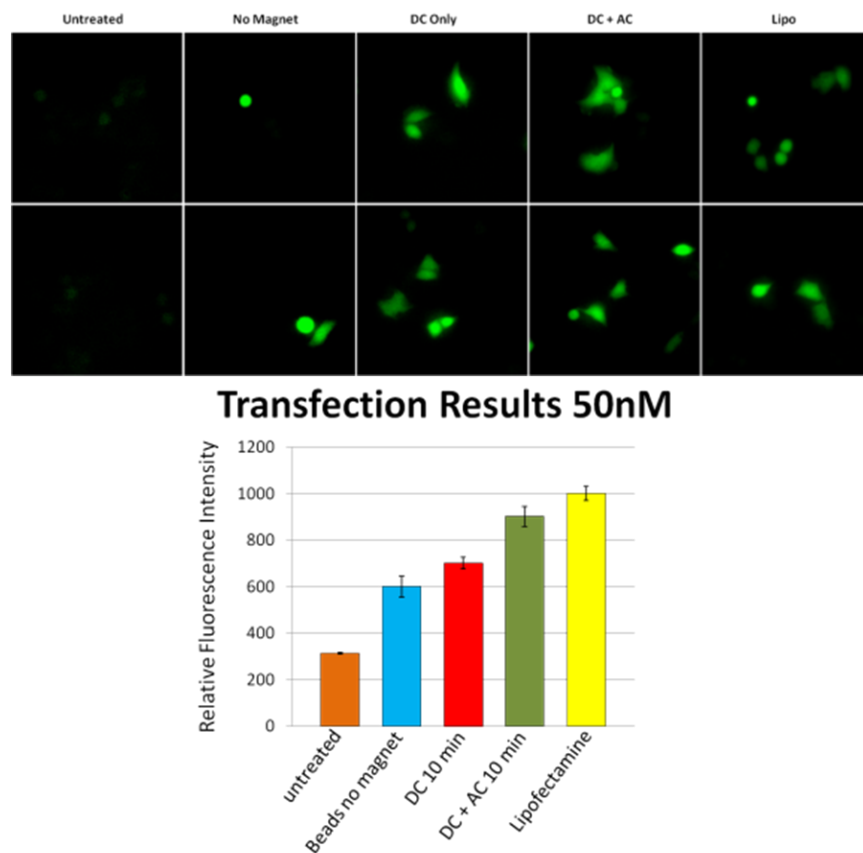


Figure 4.4 Images from the transfection experiment. (Top Left to Right) The images show untreated, nanoparticles with no magnet, nanoparticles with a static field

application, nanoparticles with static plus oscillating field, and a Lipofectamine control. (Bottom) Image segmentation results from transfection.

The relative fluorescence intensity of the 10 minute static field (DC) application was 701 ± 25 as compared to the non-magnetic particle dosage which measured 600 ± 46 . It should be noted that there was a clear difference in the number of expressing cells between the DC application and the no magnet sample. Transfection efficiency was not measured in these experiments, but qualitatively, finding fluorescent cells in the non-magnet sample required significantly more scanning of the well between fluorescent cells, meaning the transfection efficiency is lower in that sample. Additionally, from a qualitative sense, the DC+AC samples had a higher efficiency than the other nanoparticle dosed samples. Transfection efficiency will be examined in later studies. After changing cell media, an additional application of an oscillating (AC) field measured a relative fluorescent intensity score of 901 ± 44 . These cells were on average 28.5% brighter than the cells from the DC application. These data indicate that the oscillating field has a direct impact on the endosomal uptake of the particle once it is on the membrane. These data are distinct from previous reports, because the effect of the uptake specifically has been isolated by the methodology of the experiment.

4.5.3 Frequency Response Transfection

Prior to transfection, the cell media is replaced with Opti-MEM reduced serum media. Nanoparticle/oligo solution is added to the cell cultures to achieve $200\mu\text{M}$ concentrations. The samples are “No Field”, “Static Only”, and “Static+ 2, 4, 10, or 20Hz” as depicted in Figure 4.2. The cells are plated in a square of 4 adjacent cells, over the magnet array such that the length of the bar magnet sweeps over the bottom of all the wells, as shown in Figure 4.5.

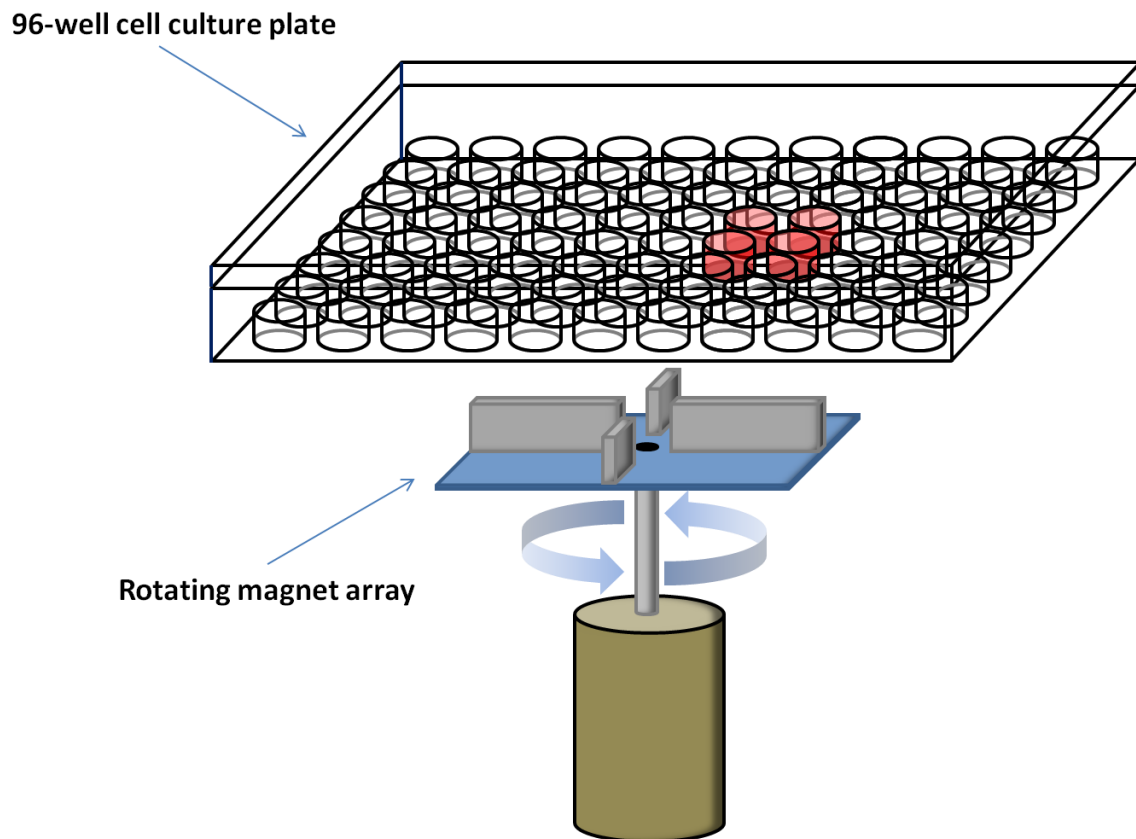


Figure 4.5 Cells are plated in 4 adjacent wells so that all cells receive the most uniform field application possible.

This allows each well to receive the most uniform field application possible. After the oscillating field application the cells are allowed to incubate for 24 hours. Prior to imaging, cells are stained with Syto 82 nucleic acid stain to enable counting of the entire cell population. Cells are then imaged to assay for EGFP expression. The entire assay is described in section 8.4.3.

4.5.4 Oscillating Field Enhancement is Frequency Dependent, and Peaks at 10Hz

Example images and a plot of the transfection efficiency are shown in Figure 4.6.

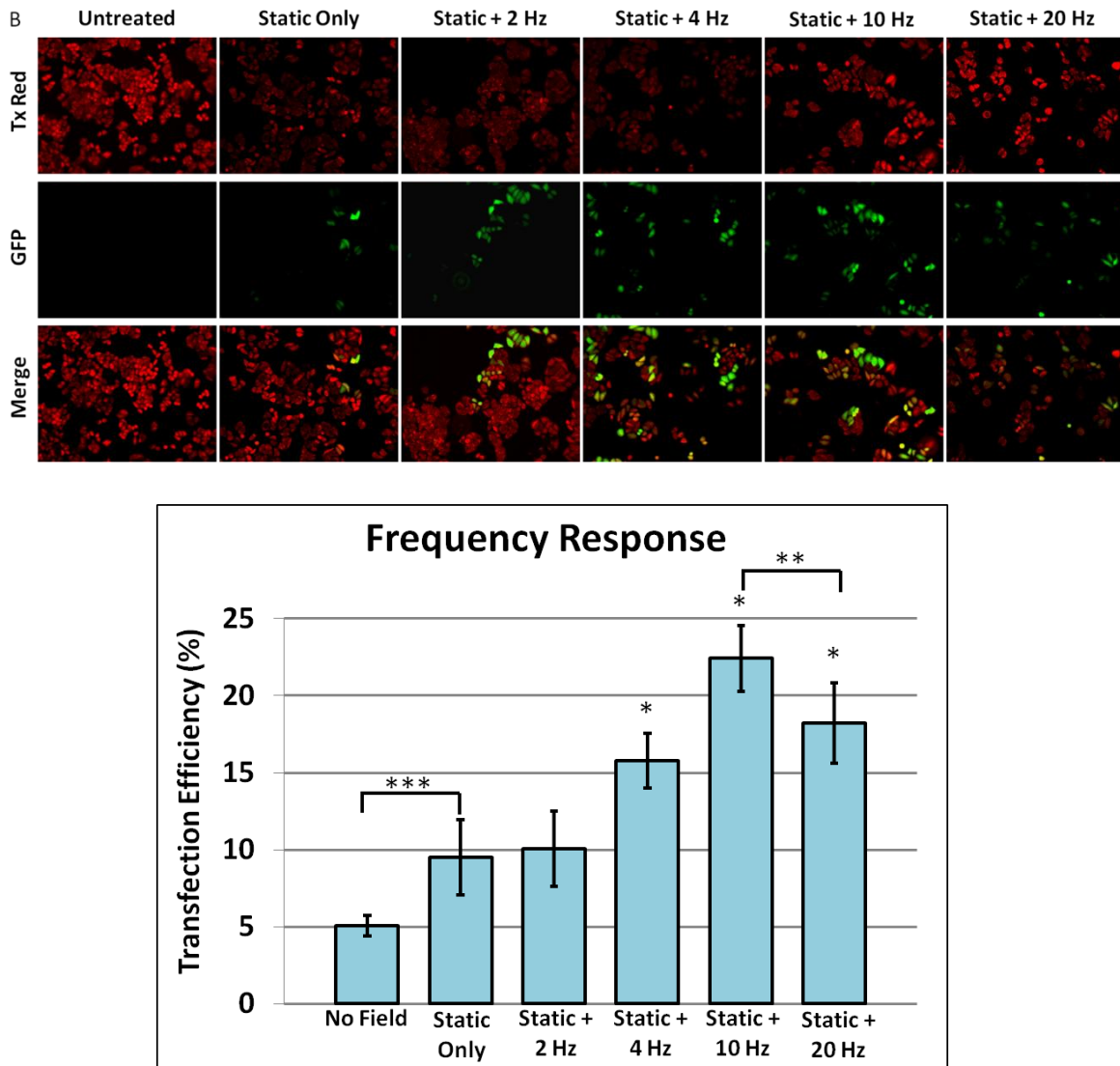


Figure 4.6 (Top) Images of HeLa EGFP-654 cells after transfection. Cells are imaged in the Texas Red (Syto 82) and GFP channels and merged together. (Bottom) Cells are counted and transfection efficiency calculated. Peak transfection efficiency is achieved at 10 Hz. (*) indicates significant difference between the static only sample, (**) indicates significant difference between the 10Hz and 20Hz samples, and (***) indicates significance between the static and non-magnetic samples.

A definite dependence of transfection rate on frequency can be seen in the analysis of the data. The sample which received the 2 Hz oscillating field showed

essentially no improvement over the sample which received only the static field sedimentation ($10.05\% \pm 1.77$ versus $9.49\% \pm 2.44$). This indicates that 2 Hz is below the threshold that can enhance the transfection. A significant increase can be seen at the 4 Hz frequency level. The transfection rate at 4 Hz is $15.76\% \pm 2.16$, which is a 66% improvement over the static field only sample. An even larger improvement is seen at the 10 Hz level. The 10 Hz produced a transfection rate of $22.41\% \pm 1.78$, a 136% improvement over the static field only sample. An interesting phenomenon is observed when the sample is exposed to the 20 Hz oscillating field. Up to 10 Hz the transfection efficiency steadily increased. However with the 20 Hz application the efficiency actually decreased below that of the 10 Hz sample. The 20 Hz sample produced a transfection efficiency of $18.22\% \pm 1.01$. While still an improvement over the DC only sample (92% increase in efficiency) it is not an improvement over the 10 Hz sample. This type of result is similar to one reported by Chari et.al where they achieved a maximum transfection efficiency at only the 1 Hz level, but saw steady decreases in expression for the 3 and 5 Hz samples. There are differences in magnet geometry between that system and the one used here, as well as differences in cell type and non-viral vector that may account for the variations with my data. External force stimulation at particular frequencies appears to be able to elicit increased activity by one or more endocytic pathways. The affects of oscillating forces on endocytic pathways are examined in Chapter 5.

Chapter 5

Oscillating Magnetic Field Transfection and Endocytosis Pathway Dependence

5.1 Overview

In order for cells to sustain themselves, they must intake nutrients from its environment. The cell membrane is studded with trans-membrane transport proteins that allow for passage of ions and other molecules such as glucose. Cells are also capable taking in other, larger particles from the extracellular environment that contact the membrane. When a particle comes into contact with the membrane, the membrane will begin to invaginate around the particle, and eventually the particle is drawn into the cell and entrapped in a vesicle formed from a pinched off portion of the membrane. This process of uptake of particles by the cell is referred to generally as endocytosis. Endocytosis can take place along one of several pathways, which are generally categorized into 5 main areas. These are clathrin-mediated endocytosis, caveolae-mediated endocytosis, macropinocytosis, phagocytosis, and non-caveolae/non-clathrin dependent pathways.

This chapter details for the first time an endocytic pathway dependence involved in oscillating magnetic field nanoparticle transfection. For the first time I identify the pathways that are highly sensitive to oscillating force application, that are able to increase transfection efficiency by as much as 2.3X. I present the first evidence to demonstrate that oscillating forces are a way to preferentially target certain pathways, without the need for specialized ligand-receptor modification to the nanoparticles. These results show the most detailed data of how forces influence transfection. I propose mechanisms that may be affected by forces to explain how they transfection is enhanced. The applications from these discoveries have an impact on future *in vivo* drug delivery and may be a means to overcome drug resistance in resistant cells.

5.2 Endocytosis Pathways

ENDOCYTOSIS PATHWAYS

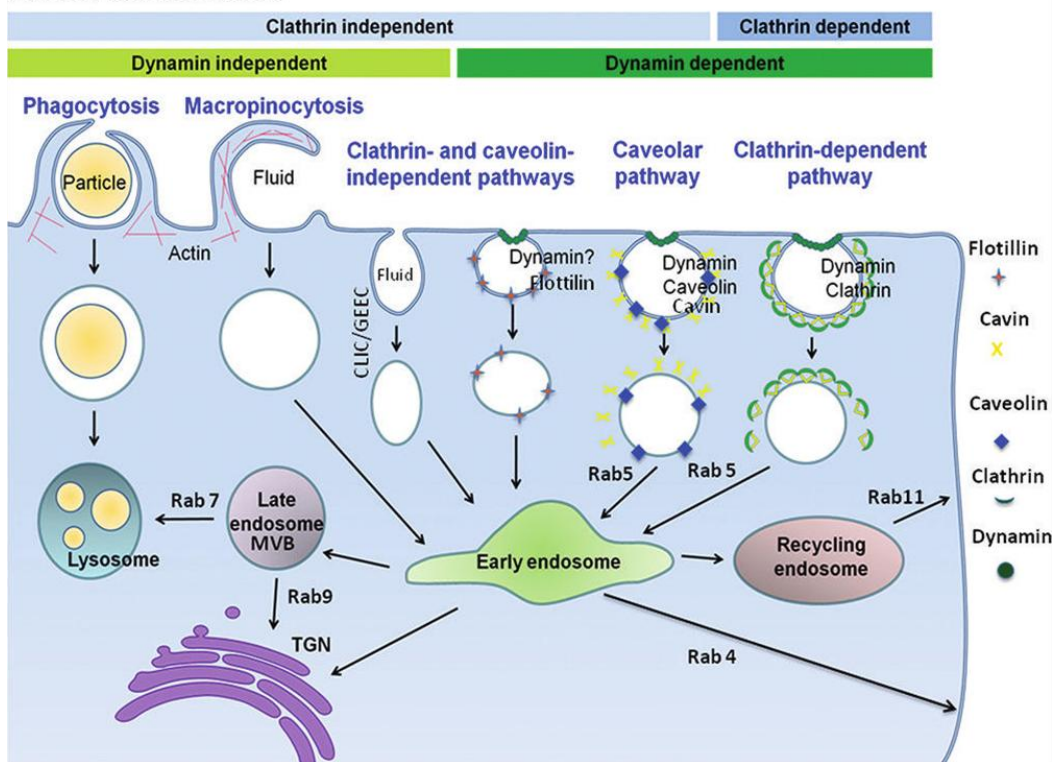


Figure 5.1 Illustration of endocytosis pathways

Figure 5.1 illustrates the various endocytosis pathways that are involved in transfection, used courtesy of Rudy Juliano of University of North Carolina at Chapel Hill. (Juliano, Ming et al. 2012) This section will discuss the pathways important in nanoparticle transfection.

5.2.1 Clathrin Mediated Endocytosis

Clathrin coated pits were first reported in 1964 in a paper by Roth and Porter. (Roth and Porter 1964) The existence of the clathrin coated lattice was first reported in 1976 by Pearse, in which coated vesicles were purified from several cell lines and imaged with electron microscopy. The clathrin protein is bound to the luminal side of the cell membrane in a complex with the adaptin protein. As a cargo molecule binds to a cargo receptor protein, the cell membrane begins to invaginate, beginning the process of transport into the cell. As this continues, the invagination begins to take on a more spherical conformation. As this enclosure is formed, dynamin and actin are recruited to this region and act to pinch it off from the cell membrane, creating a newly formed intracellular vesicle. This is referred to as a clathrin coated vesicle. The clathrin proteins form a lattice around the exterior of the vesicle and as such are generally restricted in size in the 85-110nm range for mean diameter. At some point after becoming fully engulfed into the cytosol, the clathrin coat releases from the vesicle, and the clathrin triskelions are recycled back to the luminal side of the cell membrane, where the process can continue.

5.2.2 Caveolae Mediated Endocytosis

Caveolae dependent endocytosis initiates at the caveolae of the cell membrane. This pathway was first described in the 1950s by Palade and Yamada. (Pelkmans and

Helenius 2002) These caveolae are formed from lipid rafts in the cell membrane, comprised of cholesterol, glycosphingolipids, and Glycosylphosphatidylinositol (GPI) anchored proteins. The primary protein constituent is the caveolin protein. Dynamin is shown to be part of the caveolae complex, a protein associated with the pinching off of vesicles at the end of the endocytic process. Lipids in the cell membrane, including the lipid rafts in caveolae, have lateral mobility across the membrane which is a function of the composition of the lipid raft. (Hancock 2006)

5.2.3 Macropinocytosis

Macropinocytosis is a third form of cellular uptake that cells use to bring nutrients from the extracellular milieu to the cytosol. First observed by Warren Lewis in 1931, the entry point for the vesicles (macropinosomes) in macropinocytosis occurs in the regions of ruffling that occurs at the periphery of spread attached cells. (Swanson and Watts 1995) This ruffling can be described as planar or circular extensions of the cell membrane which protrude out and then fold back into the membrane. This process results in the formation of the characteristic vesicles. These macropinosomes can be as large as 5µm, (Fawcett 1965) significantly larger than the vesicles involved in clathrin mediated endocytosis. The ruffles are the result of actin filaments protruding and causing the membrane to ruffle, or appear to ruffle when viewed at an increased frame rate.

5.2.4 Non-Caveolae/Clathrin Mediated Endocytosis

There is an additional pathway that is caveolae and clathrin independent. This is a more general category which includes several pathways that have the common feature of not relying on clathrin or caveolae for uptake. Like the other pathways, they can be

dynamin dependent or independent. Flotillin is a protein that has been shown to be key in one of these pathways and in some sense forms its own unique pathway. These pathways are also categorized based on the types of ligands or cargo that they are known for trafficking.

5.3 Experiment

To test the pathway dependence, cells are treated with one of several inhibitor drugs to block a specific uptake pathway prior to transfection. The purpose is to determine which pathways are most affected by the application of oscillating forces, to elucidate the reasons why the forces produce the observed effect.

5.4 Actin Inhibition of Transfection

Lipofectamine is a lipid based transfection reagent that allows DNA to fuse with the cell membrane, overcoming the electrostatic repulsion between the gene and membrane. I wanted to test whether the oscillating forces were in some way enabling a type of membrane fusion, where the oscillating force is physically perturbing the nanoparticle to move through the membrane. This would allow the nanoparticle to gain entry into the cell independent of the traditional endocytic pathways. Nanoparticles gain entry into the cell through multiple pathways but it was possible that the membrane fusion hypothesis explained the enhancement of transfection efficiency by oscillating fields.

Actin plays a vital role in many endocytic pathways, (Juliano, Ming et al. 2012) including macropinocytosis, clathrin, and caveolae-mediated pathways. The nanoparticles gain entry to the cell via one of the many endocytic pathways which depend

on actin for their activity. Therefore, if actin activity is knocked down temporarily in the cell, nanoparticle transfection should be severely decreased, if not eliminated all together. Applying an oscillating magnetic field for transfection increases the expression in the cells for reasons that are not well understood. However, if the oscillating field influences transfection in ways that are dependent from actin activity, i.e. membrane fusion, this would explain why oscillating the field increases transfection efficiency.

5.4.1 Latrunculin B Dose Determination

To this end, to test the impact of AC field transfection on non-actin dependent pathways, we must knock down actin activity in the cells. Latrunculin B is a cell-permeant macrolide marine toxin derived from sponges and nudibranches. (Pawlik 1993) This compound acts to disrupt actin polymerization by binding one-to-one with G-actin monomers. With actin knocked down, normal cell morphology is disrupted, and the cells take on a more rounded-up, less spread morphology. Cells were dosed with concentrations of Latrunculin B of 1, 5, 50, and 250 μM . The difference in morphology can be seen in Figure 5.2.

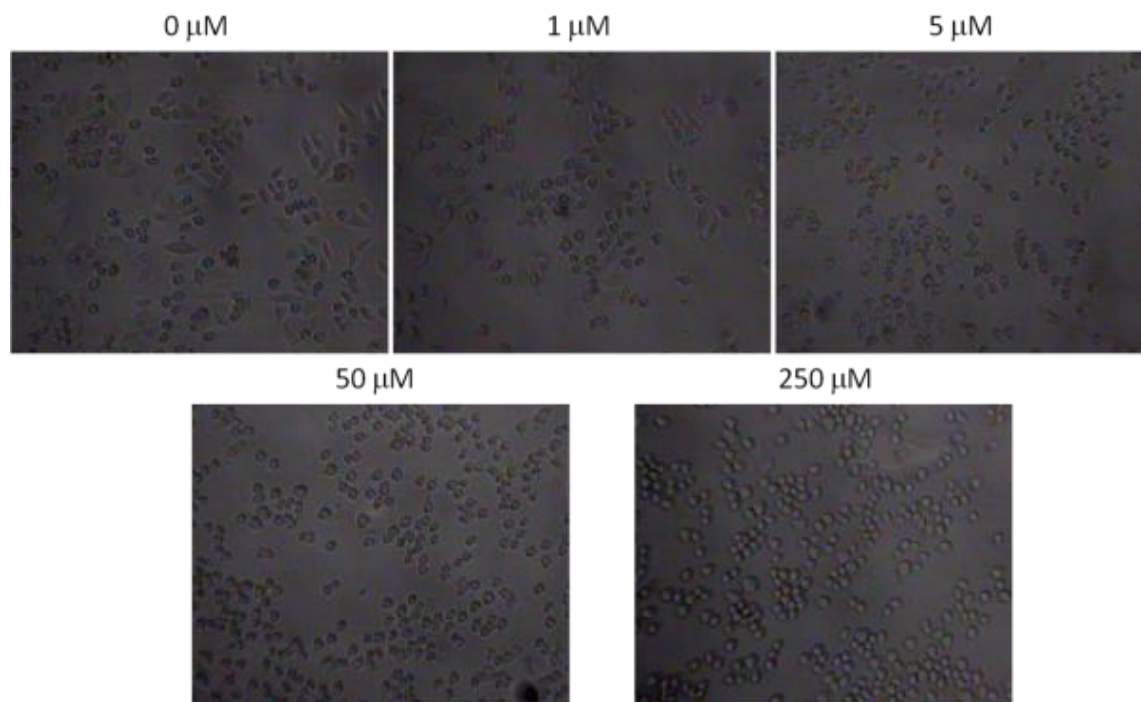


Figure 5.2 Bright field images of cells treated with Latrunculin B for 1 hour.

This change in morphology is evidence of the Latrunculin B treatment. After 1 hour of incubation with Latrunculin B, all samples exhibited cells showing a more rounded morphology, in contrast to the untreated cells. The 50 and 250 μM samples qualitatively exhibited the highest level of morphology change. After the hour incubation with Latrunculin B the media is replaced with DMEM/F12 with 10% FBS. After 24 hour incubation the cells were imaged to observe effects post Latrunculin B treatment. The 1 and 5 μM recovered normal morphology after treatment. The 50 μM cells retained viability but exhibited abnormalities in cell morphology. The 250 μM dosage was highly toxic for the cells and all were dead 24 hours later. For AC experiments the 5 μM dosage was selected for effectiveness of actin knockdown and recovery of morphology after 24 hours.

5.4.2 Determination of Lat B Incubation Time

In order to knock down the actin activity for the initial incubation period of the transfection, the transfection must not only be performed in the presence of Latrunculin B, but also the Latrunculin B must remain in the media for a period of time after the initial transfection time. Removal of Latrunculin B immediately following the initial sedimentation of the particles results in the recovery of particle uptake and expression of EGFP. This is proven by an experiment to understand an appropriate incubation time to achieve knockdown of nanoparticle transfection. The cells were dosed with Latrunculin B for 1 hour and then transfected for 30 minutes with the nanoparticles. At the end of the transfection the media was replaced with DMEM without Latrunculin B. Even with the 90 minute incubation with Latrunculin B, actin activity and nanoparticle uptake were recovered following replacement of the media. This recovery is shown by the fluorescence activity in the Latrunculin B experiment in Figure 5.3.

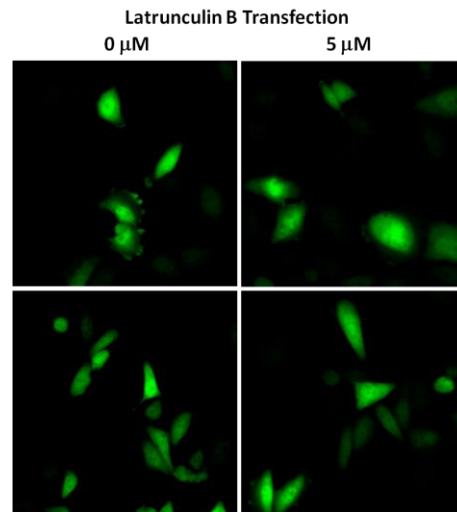


Figure 5.3: Fluorescent images of transfected HeLa EGFP 654 cells. The images on the left are not treated with Latrunculin B. Cell on the right show expression of EGFP, indicating recovery of nanoparticle uptake after dosing immediately after Lat B removal.

The goal of the Latrunculin B was to significantly reduce the expression levels by inhibiting endocytosis but it was clear from imaging that the Latrunculin B sample was expressing. It was evident that the Latrunculin B would have to remain in the cell culture in the time immediately following the transfection period.

5.4.3 Expression is Restored Unless Lat B Remains in Culture Several Hours after Transfection

To prepare the cells for transfection, Latrunculin B is diluted in Opti-MEM cell culture media to achieve a 5 μ M concentration. Prior to transfection, cell media is removed and replaced with the 5 μ M Latrunculin B Opti-MEM solution. This solution is allowed to remain in the cell culture for at least 1 hour in the incubator before transfection reagents are dosed to the cells. While the cells are incubating with the Latrunculin B, 130nm particles (1mg/ml) are mixed with the oligonucleotide (50 μ M) and phosphate buffered saline at a 25:5:70 volume ratio. Simultaneously, oligos are complexed with Lipofectamine 2000 and Opti-MEM at a 5:5:90 ratio by volume. After the 1 hour incubation with Latrunculin B, the cells are dosed with the nanoparticle and Lipofectamine solutions in their respective wells to achieve 50nM concentrations. Cells are dosed with the transfection reagents in the presence of 5 μ M Latrunculin B. Initially the effects of Latrunculin B are tested on the standard nanoparticle delivery. That is to say, I first test them on the standard DC magnetic field transfection, without application of oscillating fields. Cells are dosed with nanoparticles for 30 minutes with and without a static magnetic field. Cells are also dosed with the Lipofectamine 2000 solution for 30 minutes. These dosages are applied to cells that have been treated with Latrunculin B and without Latrunculin B as controls. After 30 minute incubation at 37.0°C, the static

field is removed and media is removed in all samples and replaced with DMEM/F12 with 10% fetal bovine serum. Cells are allowed to incubate for 24 hours before being imaged for EGFP expression. Cells are imaged at 36X on an Olympus IX81 motorized inverted microscope. Imaging is acquired with a QImaging Rolera EM-C² emccd 14-bit digital camera. The microscope, filters, shutters, and camera are all controlled via Metamorph from Molecular Devices.

Images of this transfection are shown in Figure 5.4.

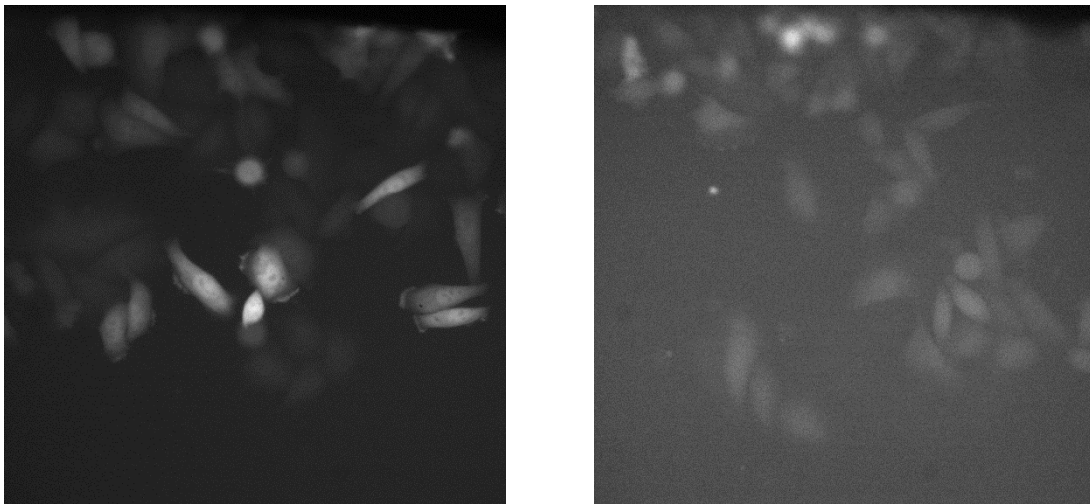


Figure 5.4 Representative images of Lat B Transfections. (Left) 0 μ M Latrunculin B sample (Right) 5 μ M Latrunculin B sample. The majority of transfection is knocked down in the 5 μ M sample when the Lat B is left in the culture several hours after initial dosage.

These data confirm that the Latrunculin B protocol did in fact inhibit transfection of the nanoparticles. Latrunculin B did not inhibit transfection of the Lipofectamine 2000 treated cells, as Lipofectamine transfection depends on membrane fusion and not an actin dependent endocytic pathway. Having confirmed the knockdown of the nanoparticle transfection the testing of the AC effects can be tested.

5.4.4 Oscillating Fields do not Enhance Transfection via Membrane Fusion

Lipofectamine is a lipid based transfection reagent that allows DNA to fuse with the cell membrane, overcoming the electrostatic repulsion between the gene and membrane. We wanted to test whether the oscillating forces were in some way enabling a type of membrane fusion, where the oscillating force is physically perturbing the nanoparticle to move through the membrane. This would allow the nanoparticle to gain entry into the cell independent of the traditional endocytic pathways. Nanoparticles gain entry into the cell through multiple pathways but it was possible that the membrane fusion hypothesis explained the enhancement of transfection efficiency by oscillating fields.

Actin plays a vital role in many endocytic pathways, (Juliano, Ming et al. 2012) including macropinocytosis, clathrin, and caveolae-mediated pathways. Without the ability to polymerize actin these processes cannot occur in the cell. To test whether the oscillating field affect can be explained via a membrane fusion process, the actin polymerization is arrested with Latrunculin B, a drug which binds to actin monomers. (Schmoller, Semmrich et al.) Cells were transfected in the presence of 5 μ M Latrunculin B. In addition to the nanoparticles, cells were also transfected with Lipofectamine 2000 as an additional control.

Cells are plated at a density of 17,000 cells per well in a 96 well cell culture plate 24 hours prior to transfection. One hour before transfection the cell media is replaced with Opti-MEM supplemented with 5 μ M Latrunculin B. After 1 hour of Latrunculin B incubation, the cells were dosed to achieve a 200 μ M dosage of the antisense

oligonucleotides. The plates were placed over a permanent magnet to sediment the particles. The cells were washed once with phosphate buffered saline and replaced with Opti-Mem supplemented with 5 μ M Latrunculin B. Some samples received no further magnetic field application, others received an additional static field, and other samples received a 4 Hz oscillating magnetic field application. After this application the samples are removed from the magnets and allowed to incubate for an additional 2 hours in the presence of Latrunculin B. Identical samples are similarly treated without Latrunculin B treatment. Figure 5.5 shows the Lat B treatment schematically.

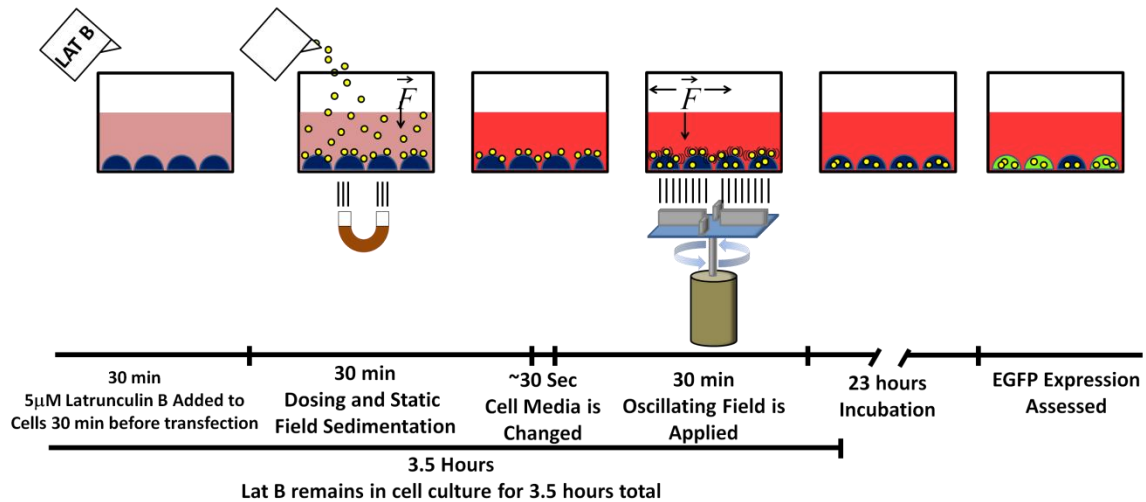


Figure 5.5 5 μ M Latrunculin B is added to the cell culture 30 minutes before transfection, and remains for a total of 3.5 hours. The Latrunculin B treatment is performed for the “No Field”, “Static Only”, and “Static+4Hz” conditions. Lipofectamine is also included as a control.

After a total of 3.5 hours of incubation with Latrunculin B the cell culture is replaced with DMEM/F12 with 10% FBS and supplemented with antibiotic/antimycotic without Latrunculin B.

5.4.5 Actin Inhibition Results

The results of the Latrunculin B transfection are shown in Figure 5.6.

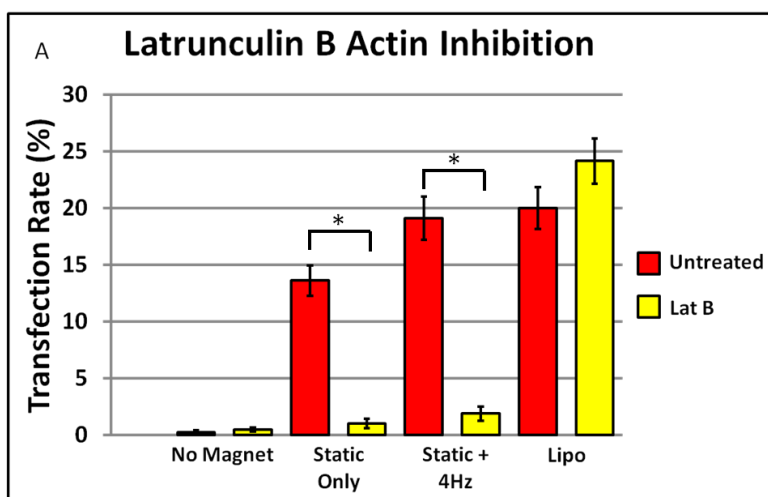
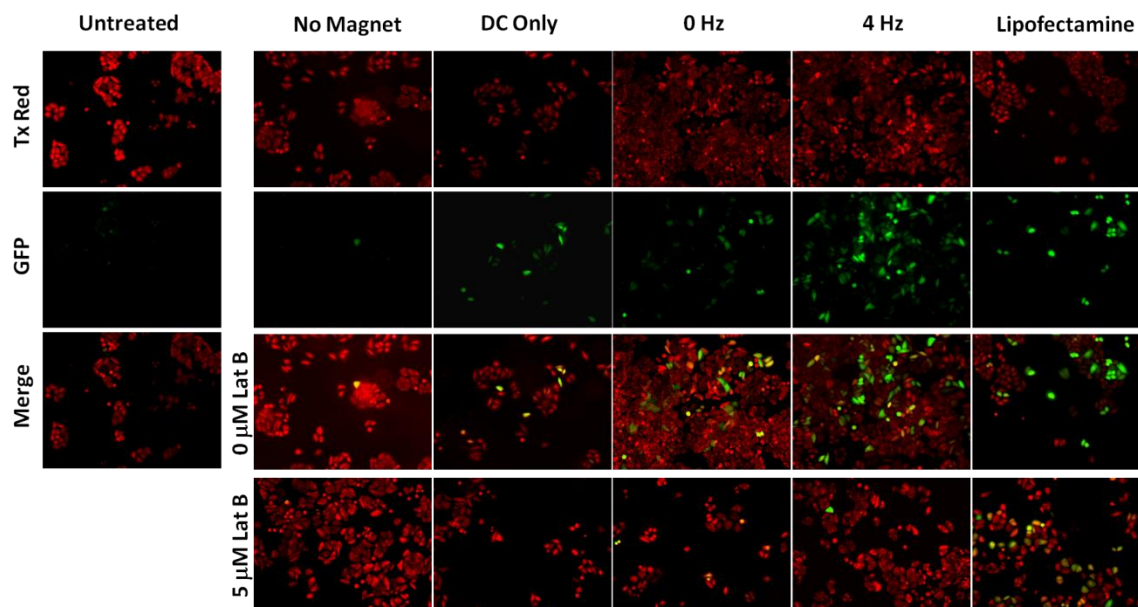


Figure 5.6 (Top) Images of HeLa EGFP-654 cells after transfection. Cells are imaged in the Texas Red and GFP channels and merged together. (Bottom) Transfection results of actin inhibition study. Cells are counted and transfection efficiency is calculated. Latrunculin B treatment effectively inhibited the nanoparticle transfection, resulting in low levels of EGFP expression. Latrunculin B did not show an inhibitory effect on the Lipofectamine 2000 treatment. Significance testing is performed at $p < 0.05$ significance level.

In imaging the results, no toxicity was observed in any of the wells. The oscillating 4 Hz sample produced a transfection rate of 19.11% on par with the Lipofectamine result, 20.02%. The 4 Hz sample exceeded the DC only and 0 Hz results, 13.6% and 12.8% respectively. Latrunculin B knocked down transfection of the nanoparticles in all of the respective wells. The 4 Hz oscillating field did not produce any significant expression as shown by the 1.15% transfection rate, not dissimilar from the Lat B DC only and 0 Hz samples (0.43% and 3.2% respectively). These data indicate that the oscillating magnetic field does not initiate a non-actin dependent pathway for uptake of the nanoparticles. If it did, one would expect a significant level of expressing cells over the other samples in the presence of the Latrunculin B. These data show no increase with application of the oscillating field. The non-magnetic application showed essentially no transfection for Latrunculin B and non-Latrunculin samples (0.45% and 0.25% respectively).

There is no designed specificity for the uptake of the nanoparticles. That is to say, no functionalization has been performed to the cells to cause them to enter the cells through a specific endocytosis pathway. In general, cells can ingest particles such as the paramagnetic nanoparticles through any of the understood pathways of endocytosis; clathrin-mediated, caveolae-mediated, macropinocytosis, non-clathrin or caveolae dependent, and phagocytosis (for specialized cell types). It could be postulated that the AC field could be affecting an aspect of cell endocytosis that is independent from these pathways. That is, it could be moving the particle through the cell membrane merely via the application of sufficient force. It seems reasonable that a sufficiently high force would be able to penetrate the cell bilayer, forcing the particle from the extracellular

space into the lumen of the cell. If this were the case it would be expected that transfection could be achieved regardless of any inhibition of endocytosis. However the Latrunculin B knockdown of actin activity showed that essentially no expression of EGFP was detected above that of the background. The maximum force that the particles experience in the z-direction is 43 fN as determined by the force calculation of section 3.2.6. It stands to reason that this force is below the theoretical force that would be required to penetrate the cell interior absent of any cellular uptake mechanism. Therefore the enhancement in transfection efficiency that the oscillating field produces is still dependent on actin dependent uptake mechanisms. Significantly higher gradients will have to be produced if endocytosis independent entry of the nanoparticles is to be achieved, although the effect of forcing multiple particles through a membrane in this fashion is not known. This has implications for potential *in vivo* gene delivery using paramagnetic nanoparticles. A tissue is composed of multiple layers of cells in a matrix of extracellular matrix. In order to deliver genes to a tissue using non-viral vectors, the particles would have to penetrate multiple layers of these cells, if that would be required to attain the therapeutic effect. In an *in vivo* system, a permanent field could be used to attract gene bearing nanoparticles to the site of interest, causing particles to sediment onto the epithelial layer. After sufficient application with the permanent field, an oscillating field would be applied to enhance uptake of the particles to the cells. The data presented here have shown improvements in transfection rate as high as 136% which would contribute significantly for improving *in vivo* efficiencies. This physical control over the localization and uptake would reduce the exposure time for the vectors to the hazards of the *in vivo* environment, minimizing the systemic responses by the body. The application

of the oscillating field would have the effect of increasing the effective dosage of the drug or gene, increasing the therapeutic effect.

5.5 Endocytic Pathway Inhibition

For inhibition studies, drugs were diluted in Opti-MEM prior to experimentation. Chlorpromazine hydrochloride (MW 355.33) was acquired from Sigma Aldrich and diluted to 14 μ M concentration. Amiloride hydrochloride hydrate (MW 266.09) was acquired from Sigma Aldrich and diluted to 100 μ M concentration. Dynasore hydrate (322.31) was acquired from Sigma Aldrich and diluted to 80 μ M concentration. Nystatin suspension (10,000IU/ml) was acquired from Invitrogen and diluted to 200IU/ml. For transfection experiments, cell culture media is replaced with the respective drug 30 minutes prior to transfection. The inhibitors remain in culture during the 30 minute transfection, and 2.5 hours post-transfection, as shown in Figure 5.7.

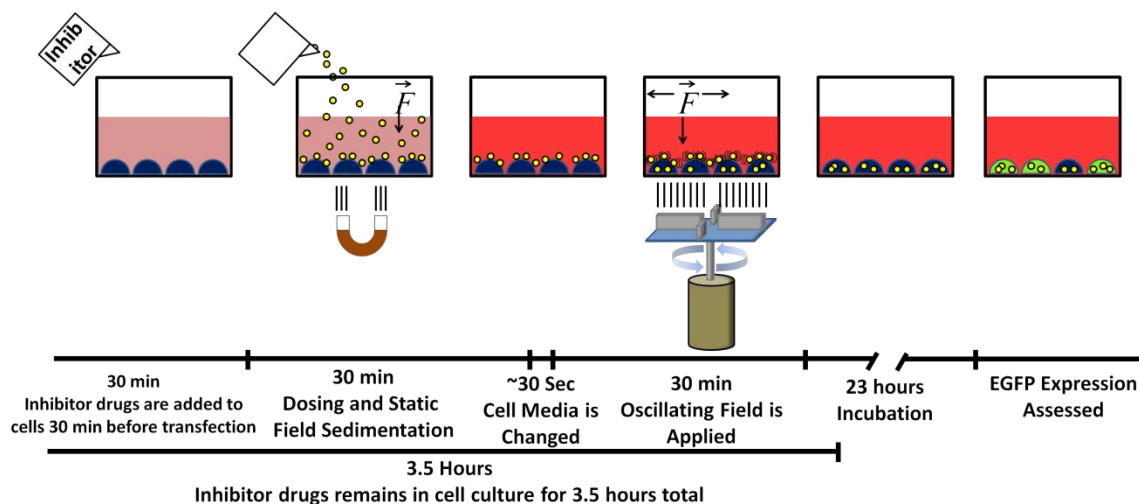


Figure 5.7 Schematic for pathway inhibition studies. Inhibitors remained in the cell culture before, during, and after transfection.

Cell cultures are incubated with inhibitor drugs for a total of 3.5 hours at which time the media is replaced with fresh DMEM/F12. Incubation with these drugs for extended

periods of time results in cell death and no toxicity was observed via light microscope inspection. Nystatin was well tolerated by the cells and remained in the cell cultures overnight. No toxicity was observed in these cell cultures.

5.5.1 No Inhibitors were Toxic in any Samples

Endocytic inhibitor drugs are effective at blocking pathways at appropriate dosages, but as with all drugs, they can become toxic beyond acceptable dosages and incubation times. To determine toxicity of the drug dosages, cells were stained with a calcein live/dead stain obtained from Invitrogen. Cells were transfected with nanoparticles as described in section 5.6.3 and treated with the selected inhibitory drugs at the respective concentrations. The experiments were the same as the static only transfections, with the exception that oligonucleotides were not used. Controls were performed in the presence of drugs and without nanoparticle dosing. The calcein stain was prepared according to the manufacturers specifications and added to the cell cultures 24 hours after transfection. Calcein stains live cells green and ethidium homodimer-1 stains dead cells red. Cells were imaged for fluorescence and counted in ImageJ. A minimum of 400 cells were counted for each sample and the percentage cell viability and standard error are calculated. The results are tabulated in Figure 5.8.

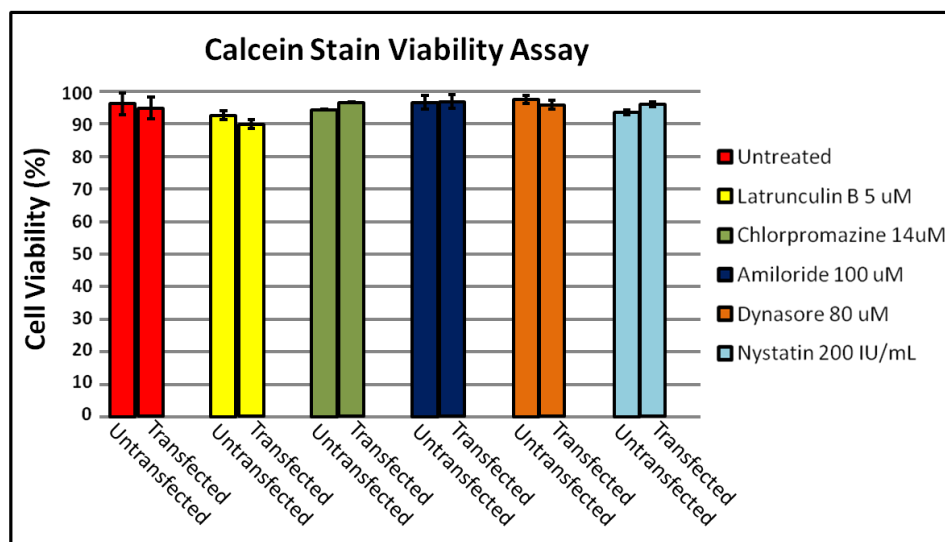


Figure 5.8 Cell viability as determined with calcein live/dead stain. “Untransfected” samples were not dosed with nanoparticles and “Transfected” samples are the results of a “static only” transfection. Toxicity was not observed in any of the samples. From left to right **Untreated** (no inhibitor drug) U = 96.2% \pm 0.05 T = 94.6% \pm 3.3. **Lat B** U = 92.6% \pm 2.7 T = 89.6% \pm 1.3. **Chlorpromazine** U = 94.4% \pm 3.7 T = 96.4% \pm 0.03. **Amiloride** U = 96.6% \pm 0.3 T = 96.6% \pm 2.2. **Dynasore** U = 97.5% \pm 0.9 T = 95.6% \pm 1.3. **Nystatin** U = 93.5% \pm 1.9 T = 95.7% \pm 0.3.

No significant toxicity was observed in any of the samples, indicating that the dosages of nanoparticles and drugs were not harmful to the cells.

5.5.2 Endocytic Inhibition Results

As with prior experiments, the application of the oscillating field yielded a distinct improvement over applying only a static field ($19.2 \pm 2.0\%$ for static + 10Hz versus $9.9 \pm 0.85\%$ for static only). The 10Hz field improved transfection efficiency by a factor of 1.94X, almost a doubling of efficiency. The no-field sample and the Lipofectamine treated samples yielded expression levels of $6.8 \pm 3.0\%$ and $8.6 \pm 1.9\%$ respectively. Data are shown in Figure 5.9 and 5.10.

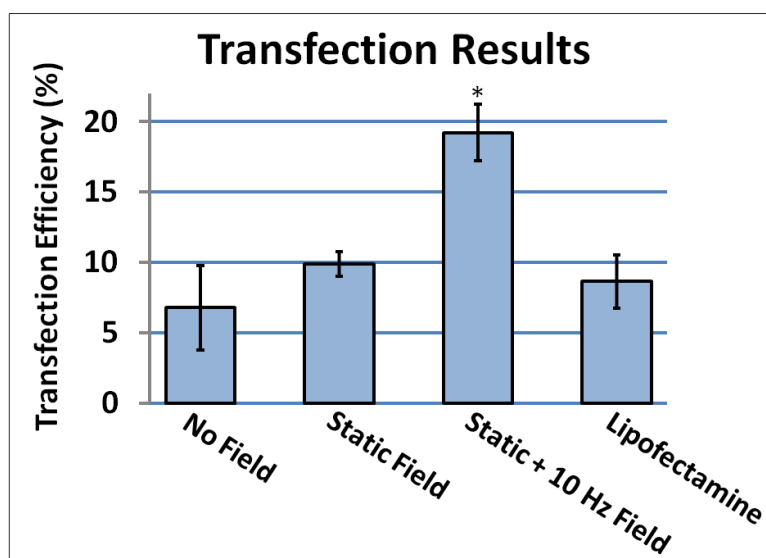
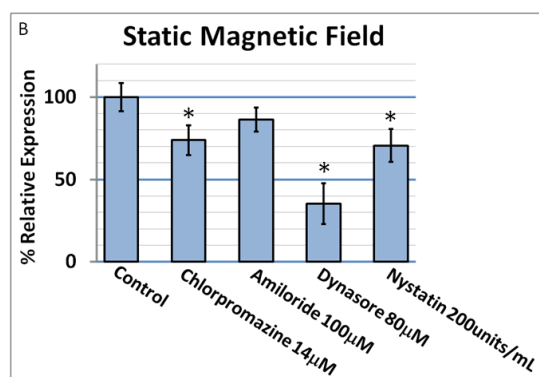
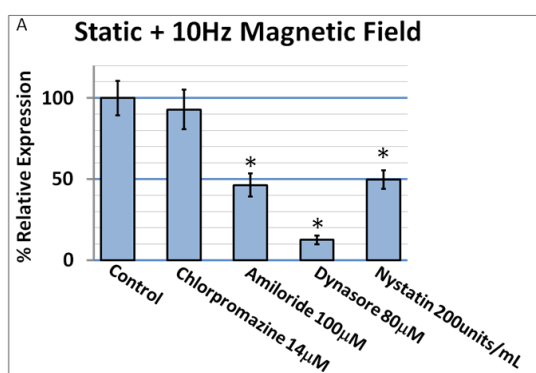


Figure 5.9 Transfection efficiency from of untreated cell samples. No field 6.8% \pm 3.0, Static field 9.9% \pm 0.85, Static + 10Hz field 19.2% \pm 2.0, and Lipofectamine 2000 8.7% \pm 1.9. The additional application of the 10Hz field yielded a significant improvement (94.2%) in transfection efficiency over the static only sample. These data serve as a baseline for endocytosis pathway inhibition results shown in Figure 5.10.

These controls are used as the baselines to measure the relative effect of the drug treatments. The results of each are shown in Figure 5.10 and 5.11.



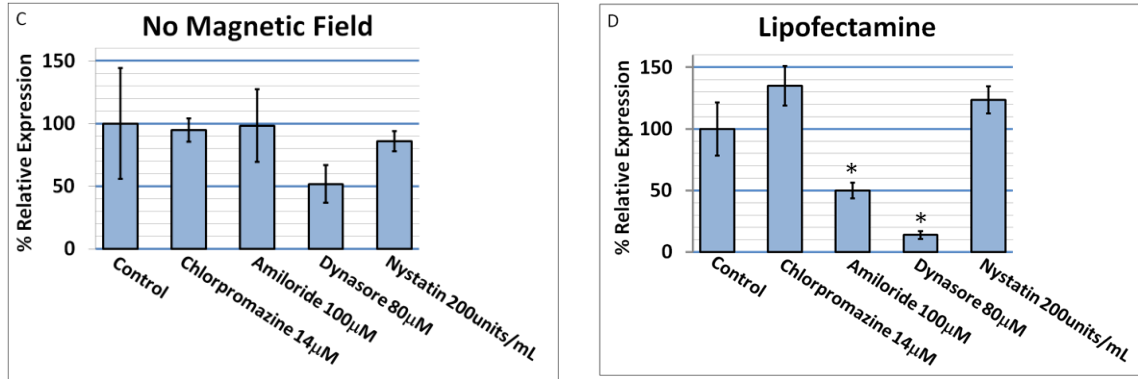


Figure 5.10 Relative transfection efficiencies after inhibition of endocytosis pathways. The untreated control samples are normalized to 100%. (A) Static + 10Hz field Untreated: 100% ± 10.6, Chlorpromazine: 92.8% ± 12.2, Amiloride 46.4% ± 7.2, Dynasore 12.4 ± 2.6, Nystatin: 49.7 ± 5.6. (B) Static field Untreated: 100% ± 8.6, Chlorpromazine: 73.8% ± 8.9, Amiloride 86.3% ± 9.7, Dynasore 35.4 ± 12.4, Nystatin: 70.5 ± 10.0. (C) No field Untreated: 100% ± 44.2, Chlorpromazine: 94.7% ± 9.3, Amiloride 98.4% ± 28.8, Dynasore 51.8 ± 12.4, Nystatin: 85.9 ± 8.1. (D) No field Untreated: 100% ± 21.6, Chlorpromazine: 135.0% ± 16.0, Amiloride 49.7% ± 6.4, Dynasore 13.8 ± 3.1, Nystatin: 123.5 ± 11.0.

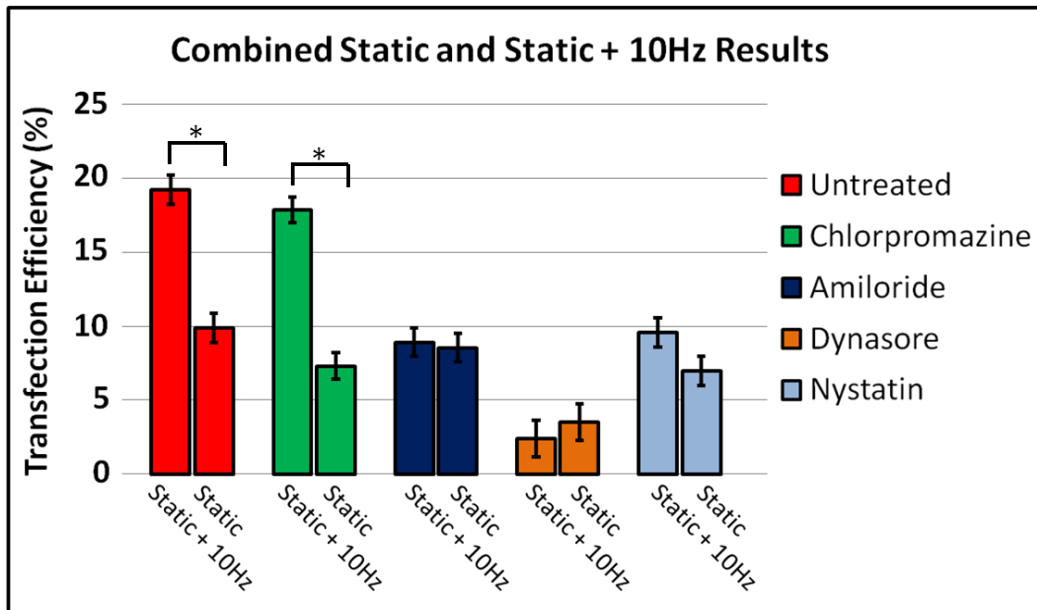


Figure 5.11. Absolute transfection efficiency data, showing impact of oscillating fields on endocytic pathway. From left (static + 10Hz) to right (static) Untreated 19.2 ± 2.0% and 9.9 ± 0.9%, Chlorpromazine: 17.9 ± 2.3% and 7.3 ± 0.9%, Amiloride 8.9 ± 1.4% and 8.5 ± 1.0%, Dynasore 2.4 ± 0.5% and 3.5 ± 1.2%, Nystatin: 9.6 ± 1.1% and 7.0 ± 1.0%. Neither of the amiloride samples are significantly different from one another, indicating that macropinocytosis is enhanced by the force oscillations caused by the 10Hz application. Lipid raft-mediated (Nystatin) pathways are also impacted by the application of oscillating forces. The clathrin-mediated pathway (Chlorpromazine) doesn't appear to

be influenced significantly by force application. Dynamin (Dynasore) inhibition shuts down the majority of all transfections, with the oscillating force having no effect. Significance testing is performed at $p < 0.05$ significance level.

5.5.3 Macropinocytosis is Up-Regulated by Oscillating Forces, and does not Contribute to Transfection Efficiency Without Them

The inhibition of macropinocytosis accounted for a 54% reduction in relative expression ($19.2 \pm 2.0\%$ decreased to $8.9 \pm 1.4\%$). This shows that macropinocytosis is particularly sensitive to an applied external oscillating force. Supporting this, the static only Amiloride sample is not statistically different from the untreated static only control, indicating that macropinocytosis is not an active contributor to the transfection during the 30 minute incubation time ($8.5 \pm 1.0\%$ for amiloride and $9.9 \pm 0.9\%$ for the untreated control). Were macropinocytosis a significant contributor in the absence of an external stimulus, these data points would be significantly different. The transfection efficiencies for the amiloride treated static only and static + 10Hz are not significantly different from one another ($8.5 \pm 1.0\%$ and $8.9 \pm 1.4\%$ respectively), further verifying that macropinocytosis stimulation is a major contributor to the improved efficiency. These data indicate that macropinocytosis is up-regulated or hyper-activated by the additional perturbation of oscillating forces.

5.5.4 Caveolae/Lipid raft Pathways Increase in Efficiency due Oscillating Forces

Treatment with Nystatin reduced EGFP expression by 50%, a significant decrease in transfection efficiency from the control ($19.2 \pm 2.0\%$ for 10Hz decreased to $9.6 \pm 1.1\%$). The nystatin treated oscillating field sample is not different from the untreated static control, indicating that no enhancement was produced in the presence of

the inhibitor. Similarly, there is no difference between the two Nystatin treated samples. Caveolae/lipid rafts are therefore also sensitive to or benefit from oscillating forces exerted on nanoparticles during transfection.

5.5.5 Clathrin-Mediated Endocytosis is not Affected by Oscillating Forces

Inhibition of clathrin in the static + 10Hz sample did not produce a statistically significant change in expression levels from the control, ($19.2 \pm 2.0\%$ compared with $17.9 \pm 2.3\%$). If the clathrin pathway was affected by the oscillating force effects, we would expect a significant decrease in the Chlorpromazine treated samples. The reduction in the static field sample was statistically significant ($9.9 \pm 0.85\%$ decreased to $7.3 \pm 0.88\%$) which indicates that clathrin is involved in the transfection of these cells. While it has been shown that the clathrin pathway is an available pathway for nanoparticle uptake, (Hsu, Ho et al. 2012) here it does not appear that it was affected by an oscillating magnetic force. Based on the previous conjecture of increasing the MSD of a particle on the cell membrane, it is not clear why this does not seem to affect the clathrin-mediated pathway.

5.5.6 Oscillating Force Enhancement is not seen without Dynamin

Inhibition of Dynamin resulted in the largest inhibition of transfection for all samples. Dynamin is motor protein involved in pinching off invaginations as they become internalized vesicles, as is shown in the clathrin and caveolae-mediated pathways. (Juliano, Ming et al. 2012) Of the non-caveolae non-clathrin dependent pathways, some are known to be dynamin dependent and others dynamin independent. Macropinocytosis and phagocytosis are not believed to depend upon dynamin for

internalization of vesicles. Undoubtedly due to the effects on multiple pathways, dynamin inhibition reduced transfection efficiency by 88% for the 10Hz magnetic field sample ($19.2 \pm 2.0\%$ decreased to $2.4 \pm 0.49\%$). The efficiency of the static field sample went from $9.9 \pm 0.85\%$ to $3.5 \pm 1.2\%$, a reduction of 65%. The Dynasore inhibition essentially negated any effect of from the oscillating field, with the transfection efficiencies of the static + 10Hz and static only samples within a standard error of the mean of each other. The severe reduction in expression does not account for the dynamin independent pathways which, based on the macropinocytosis inhibition, should account for more than 2.4% transfection efficiency. In spite of this it is clear that the enhancement due to oscillating fields is dependent upon dynamin activity to be effective.

5.5.7 “No Field” and Lipofectamine Controls

The relative transfection efficiency of the no field samples were not remarkably different from one another with the exception of the Dynasore treated one (Untreated: $100 \pm 44.2\%$, Chlorpromazine: $94.7 \pm 9.3\%$, Amiloride $98.4 \pm 28.8\%$, Dynasore $51.8 \pm 2.4\%$, Nystatin: $85.9 \pm 8.1\%$). Thirty minutes incubation time is not a sufficient time for the sedimentation of colloidal nanoparticles of this size and these data are intended as a control showing the effects of increased sedimentation in the static field samples. A longer time course would be needed for a comparison with non-magnetic delivery.

For treatment with Lipofectamine 2000, a 30-minute incubation time is short relative to a typical transfection (Ming, Sato et al. 2011) but delivery is still achieved. The clathrin and the lipid-raft mediated pathways showed no reduction in transfection efficiency with treatment of inhibitory drugs. A high level of reduction was shown with macropinocytosis inhibition (~50% decrease from the control), indicating that this is an

important pathway for lipid based delivery. Lipid based gene delivery is known to occur through a membrane fusion process (Chesnoy and Huang 2000), where the lipid-DNA complexes bind to the cell membrane, merging the two. This allows the DNA to pass through into the interior of the cell, making it available for expression. However, the dependence on macropinocytosis is consistent with other studies that have shown that this pathway is an important mechanism for lipid transfection. (Zhang, Allen et al. 2011; De Haes, Van Mol et al. 2012) Macropinocytosis showed little activity in the static only nanoparticle transfections, but since it is inhibiting a portion of the Lipofectamine delivery, we know that it is active during the 30 minute transfection period. This further supports the idea that the oscillating field is in some way hyper-activating this pathway to take up the nanoparticles. Dynamin inhibition effectively blocked the vast majority of transfection (~86% reduction). It is clear that active processes are involved in lipid-based transfection, but a more thorough study would be needed to fully examine this dependence. The activity of all of the pathways, including the membrane fusion process, does not occur at the same rates relative to each other. Over different time scales, certain pathways may predominate in the overall transfection. For this study, Lipofectamine transfection serves as a positive control for the efficacy of the oligonucleotides.

5.5.8 Possible Mechanisms of Force Sensitivity: Flexing of Membrane Ruffles

Applying oscillating forces to a ruffle associated nanoparticles may stimulate bending of the ruffles to induce closure into vesicles. The entry point for the vesicles (macropinosomes) in macropinocytosis occurs in the regions of ruffling that occur at the periphery of spread attached cells. (Mukherjee, Ghosh et al. 1997) The forces applied on the nanoparticles are within the range needed to buckle actin filaments of sufficient

length, (Footer, Kerssemakers et al. 2007) particularly given the likelihood of particles being aggregated.

The ruffling typical of macropinocytosis is dependent upon the polymerization and de-polymerization of actin in the form of F-actin filaments. (Lee and Knecht 2002) As a filament polymerizes next to a load it exerts a pushing force against it as monomers are added. This event can be modeled as an elastic slender rod that is clamped at one end and free at the other. The slender rod also has a characteristic flexural rigidity. The flexural rigidity of is a property which describes the ability of the rod to bend given an applied moment. The flexural rigidity of a single actin filament has been determined to be $0.06 \text{ pN}\cdot\mu\text{m}^2$. (Yasuda, Miyata et al. 1996) For a rod of circular cross section clamped at one end, the force needed to buckle the rod is characterized by the equation:

$$F_b = \left(\frac{\pi^2}{4} k \right) / L^2 \quad (5.1)$$

where k is the flexural rigidity and L is the length of the rod. (Howard 2001; Footer, Kerssemakers et al. 2007) Taking the flexural rigidity reported in literature we can produce a plot of buckling force versus length of the actin filament.

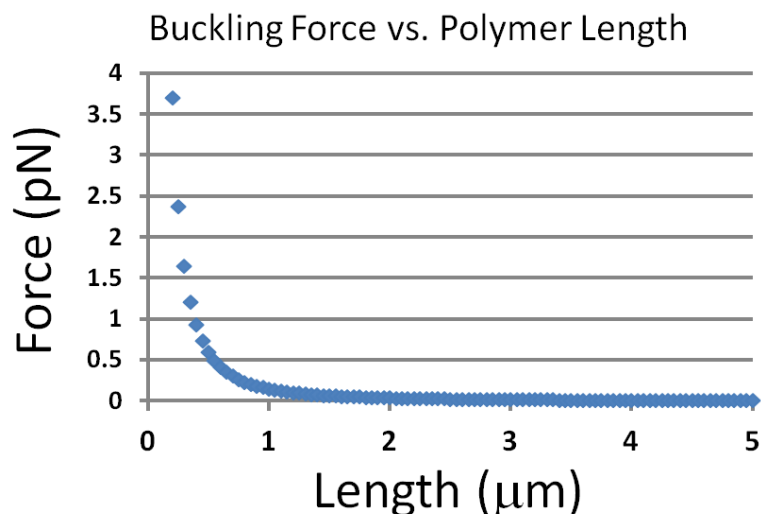
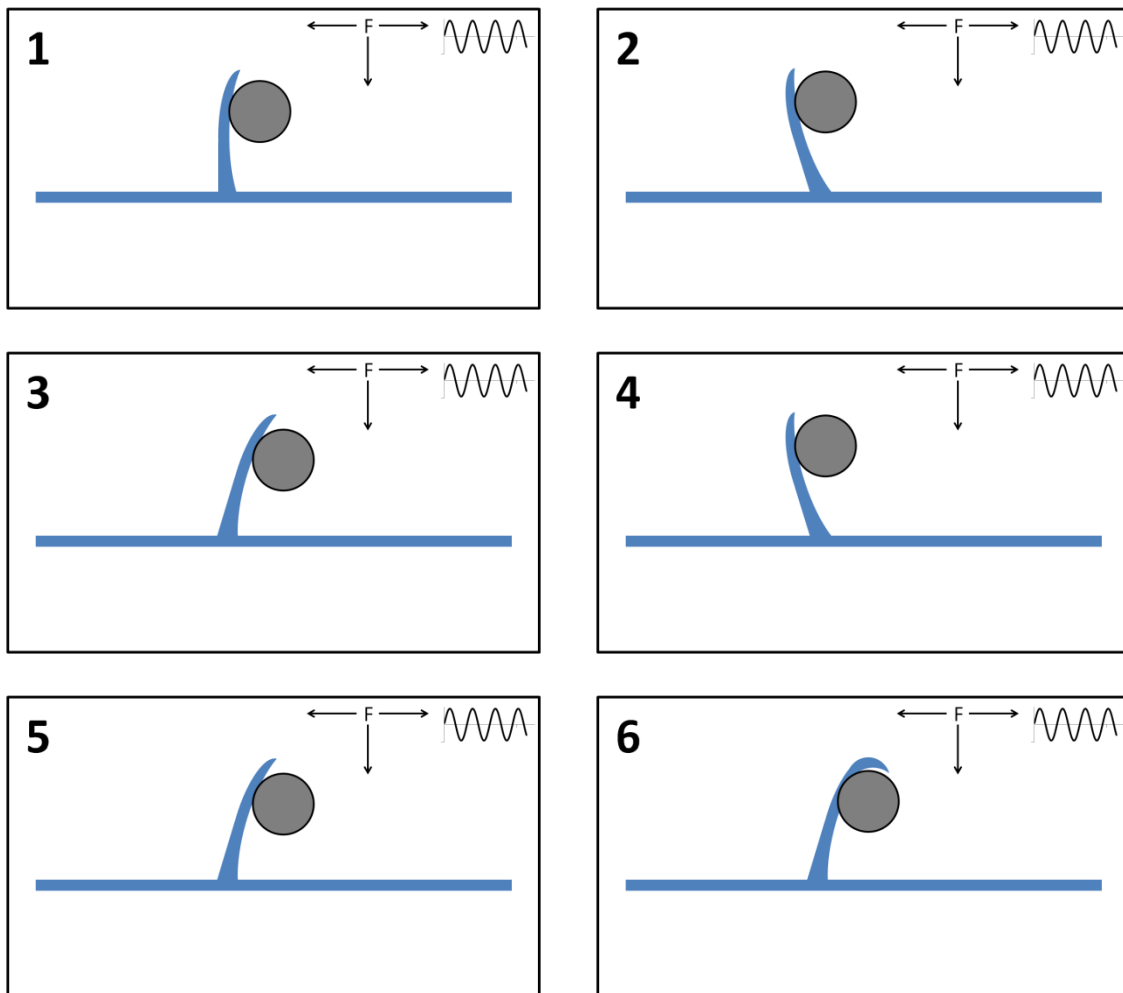


Figure 5.12 Theoretical buckling force an actin polymer versus length of the polymer. Force applied to an aggregate of 10 nanoparticles is sufficient to buckle filaments greater than 550nm.

The force applied on a theoretical aggregate of 10 nanoparticles ($\sim 0.5\text{pN}$) is sufficient to buckle actin filaments greater than 550nm. Actin filaments aligned in parallel would cause the force to be divided among all of the filaments. Therefore a force that would buckle a single 550nm filament would buckle 10 filaments 1.75 μm in length. Experimentally, forces of 0.2-0.8pN were shown to buckle actin bundles in the range of 400-900nm in length, which were comprised of, on average, 4-10 filaments. For sufficiently long actin filaments, it is possible for these force regimes to apply sufficient buckling forces on multiple filaments in parallel arrangement, which form the membrane ruffle. Additionally, the ruffling that occurs at the membrane periphery does not necessarily result in the formation of a macropinosome. That is, the ruffle can recede back into the membrane without forming an enclosure or vesicle. (Swanson and Watts 1995) Applying forces laterally and normally (relative to the plane of the cell) to a ruffle-associated nanoparticle could induce the necessary folding and enclosing process,

perhaps increasing the number of vesicles that form due to macropinocytosis. The cell membrane/cortex is resistant to deformation and it known that the conformational shape changes characteristic of endocytosis occur with a significant energy cost (Liu, Sun et al. 2009) which may be overcome with the externally applied force.

It is possible that these force regimes are sufficient to stimulate increased activity of the cell surface ruffles by bending or flexing the membrane ruffles. This could assist in the closure of the ruffles to form the early vesicle as illustrated in Figure 5.13.



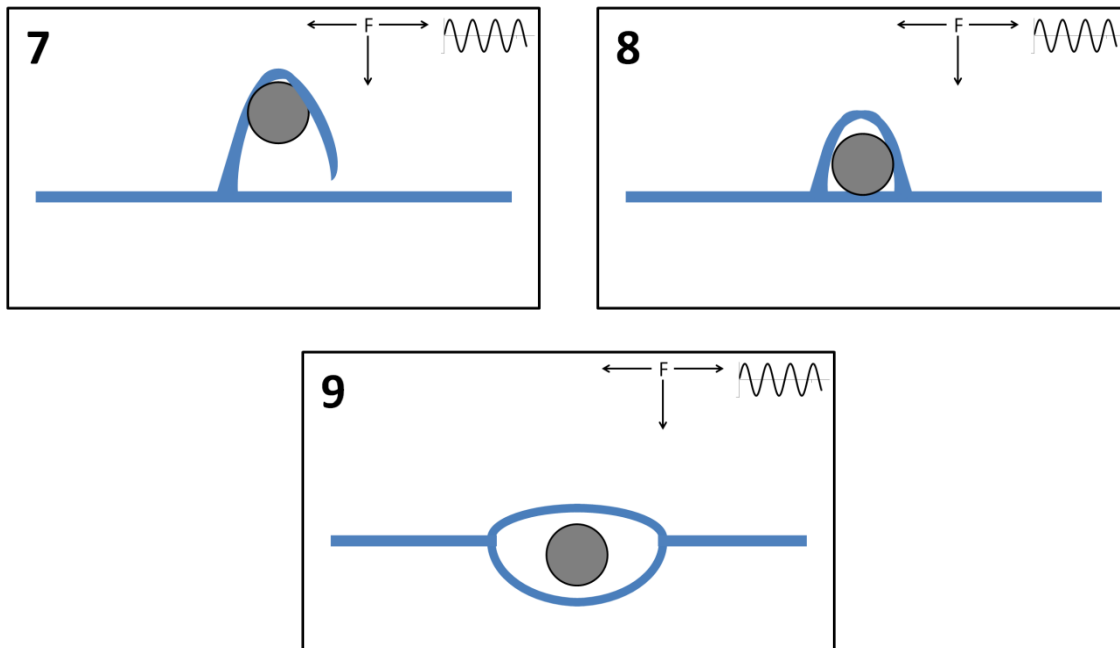
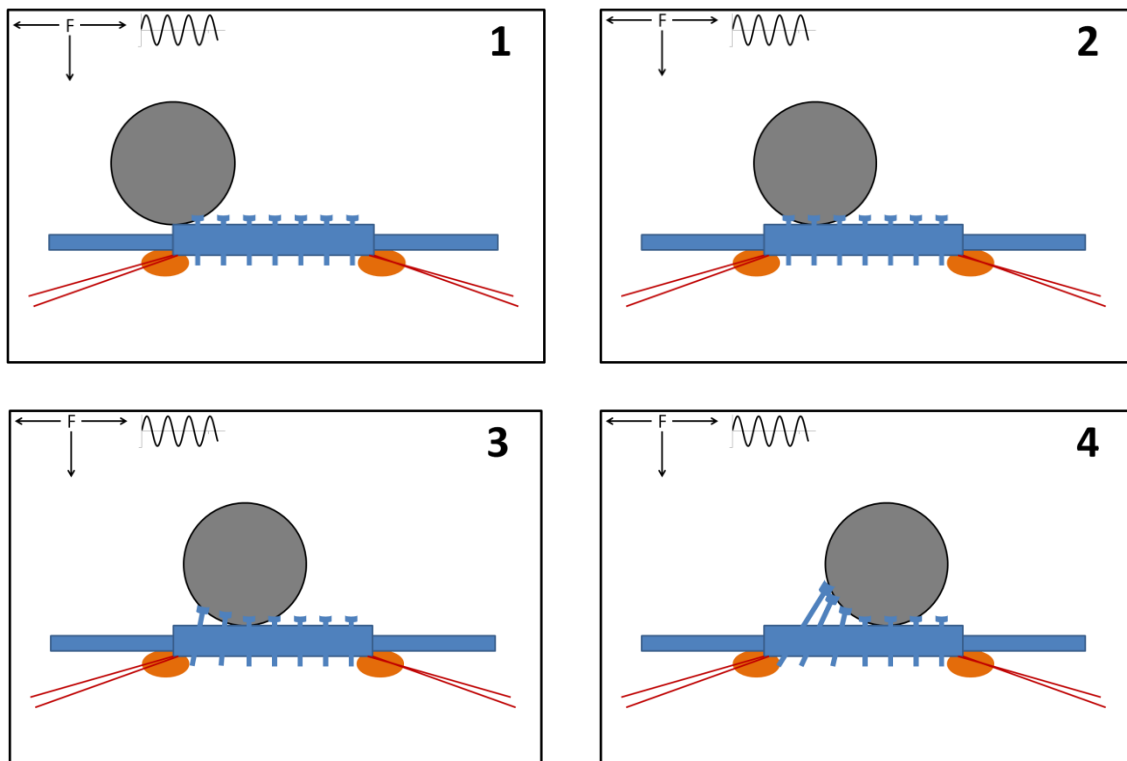


Figure 5.13 Proposed mechanism for enhancement of macropinocytosis with oscillating forces. 1. Nanoparticle is attached to a membrane ruffle. 2-5. Oscillating forces cause flexing of the ruffle. 6-8. Forces cause the folding over and closure of the ruffle, forming the early vesicle. 9. Macropinosome moves into the cell.

Work has begun (not presented here) to test this hypothesis. I am currently attempting to co-localize membrane ruffles/macropinosomes and nanoparticles on individual cells. Fluorescent dextran is being used to locate macropinosomes or membrane ruffles since it is known that dextran enters the cell preferentially through this pathway. (Zenni, Giardina et al. 2000) By visualizing particles and dextran, I hope to quantify the degree of association nanoparticles with macropinosomes, with and without a magnetic application. I also plan to apply oscillating forces with the 3-dimensional force microscope to observe the degree of movement that is associated with the nanoparticle/ruffle/vesicle complexes. This would verify whether the oscillating forces were sufficient to manipulate this process.

5.5.9 Possible Mechanisms of Force Sensitivity: Increased and Faster Binding with Trans-membrane Proteins

There are several possible explanations as to why caveolae/lipid rafts are affected by oscillating fields. Caveolae have been shown to be associated with a variety of receptors and trans-membrane proteins (Yamamoto, Toya et al. 1998; Simons and Toomre 2000; Chini and Parenti 2004) which are implicated in cell signaling. Perturbing a nanoparticle in a caveolae may cause it to increase the number of contacts with receptor proteins, initiating trans-membrane signaling which leads to internalization, which is illustrated in Figure 5.14.



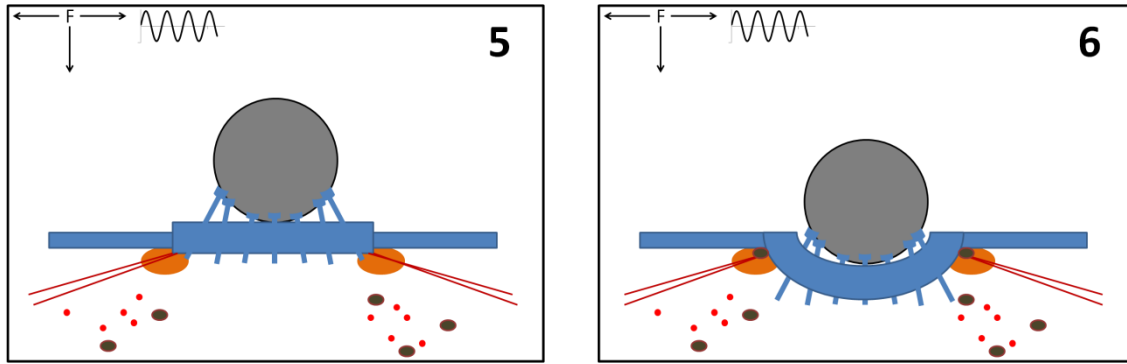


Figure 5.14 Proposed mechanism for oscillating force enhancement in caveolae/lipid rafts. 1. Bead contacts caveolae. 2. Oscillating forces begin to roll the nanoparticle across the caveolae. 3-4. The oscillations cause the particle to make contacts with trans-membrane proteins responsible for initiating endocytosis. 5-6. With trans-membrane contacts made, dynamin, actin, and other protein recruitment begins, and the particle is enveloped. The oscillating forces may cause this process to occur more quickly and at a greater percentage over the surface of the cell.

Additionally, it may increase the rate at which the contacts are made, causing the internalization process to commence at an earlier time. Without the perturbation the binding of any particular nanoparticle may not occur at all or may occur at a slower rate so as to delay the onset of expression. Simian virus 40 (SV40) has been shown to utilize caveolae-mediated endocytosis to gain entry into the cell. (Pelkmans, Puntener et al. 2002) It was shown that the SV40 viruses concentrated at caveolae and are internalized whereas empty caveolae did not become internalized. (Pelkmans, Kartenbeck et al. 2001) Some manner of perturbation is needed in accessing this pathway, which we may be assisting with the oscillating magnetic force.

To verify this, fluorescent caveolae/lipid rafts would be dosed with fluorescent nanoparticles. Imaging would be performed to measure the degree of co-localization between nanoparticles and caveolae with and without magnetic application. If the

oscillating forces cause a greater incidence of nanoparticle binding to caveolae, this should be evident in changes to percent co-localization.

5.5.10 Possible Mechanisms of Force Sensitivity: Improved Transport Through the Glycocalyx

Applying external force to a nanoparticle can also increase the mean square displacement of a nanoparticle on the membrane, possibly giving it a greater probability of reaching the lipid rafts or membrane ruffles. HeLa cells have a glycocalyx layer above the cell membrane which acts as a barrier for macromolecule transfer. (Zhou, Xiong et al. 2011) Many epithelial cell types produce this layer of proteoglycans, glycoproteins and glycolipids that sheaths the outer layer of the cell membrane. (Reitsma, Slaaf et al. 2007) This layer is a gel-like matrix that has been shown to be as much as several microns in thickness. (Weinbaum, Tarbell et al. 2007) This layer can act as a selective barrier for macromolecules from blood to the cells. (Henry and Duling 1999) This also presents a barrier to non-viral vectors for entry into the cell. A nanoparticle must traverse this region and in order to achieve successful delivery which presents a possible reason for how an oscillating magnetic field can impact the transfection.

Several studies have investigated the rheology of the glycocalyx by introducing nanoparticles and observing and tracking the displacements. (Nijenhuis, Mizuno et al. ; Zhou, Xiong et al. 2011) Calculating the mean square displacement is used to determine a diffusion constant, which describes how quickly a particle will move through the material. The diffusion constant of glycocalyx in HeLa cells was experimentally determined to be $0.15 \pm 0.014 \mu\text{m}^2/\text{s}$. (Zhou, Xiong et al. 2011) The Stokes-Einstein equation defines the diffusion coefficient (D) as:

$$D = \frac{kT}{6\pi\eta r} \quad (5.2)$$

where k is Boltzmann's constant, T is temperature, η is viscosity, and r is the radius of the particle. Taking the experimental diffusion constant, we can solve for viscosity and show it is equal to 0.0221 Pa·s. The force applied to the particles can be used to determine the velocity based on Stokes' equation of drag force on a particle:

$$F_d = 6\pi r \eta v \quad (5.3)$$

where F_d is the drag force, r is the radius of the bead, η is the viscosity of the Newtonian fluid, and v is the velocity of the bead. The plots of velocity vs. force are shown in Figure 5.15.

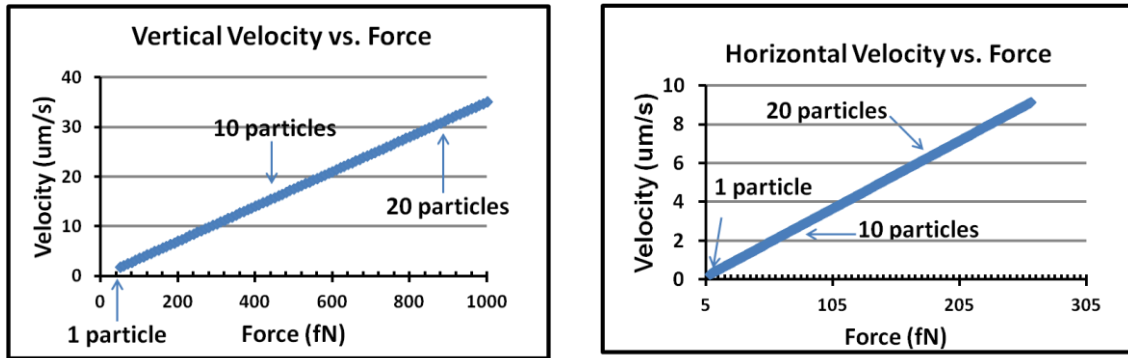


Figure 5.15 Theoretical velocity vs. force plots for 130nm nanoparticles in HeLa cell glycocalyx. (Left) The vertical component of velocity. (Right) The horizontal component of velocity. The applied magnetic force can propel the nanoparticles through the glycocalyx at velocities comparable to organelles being transported inside of cells.

A particle must traverse the glycocalyx in order to reach the cell membrane and be accessible to the endocytic pathways. A particle undergoes a random walk due to diffusion in a gel. As it takes the random walk, it encounters regions of the gel mesh. The gel mesh can vary in porosity, so the nanoparticle will encounter open areas through

which it can easily travel. It can also encounter regions of more densely packed mesh. In regions such as this, the particle can become entrained in the meshwork and sequester the nanoparticle away from the endocytic mechanisms. Applying an oscillating force to a nanoparticle could free the particles from regions where it has become entrapped by increasing the mean square displacement of the particle. The horizontal component of velocity on a single nanoparticle is minimally 280nm/s and the vertical component is 1.75 μ m/s. This velocity will increase for aggregates of nanoparticles, but these velocities are well within the range of organelles transported within the cell. (Hill, Plaza et al. 2004; Kural, Kim et al. 2005) Organelles move through the viscoelastic environment of the cytoplasm at rates similar, so it is a reasonable conjecture that this magnitude of oscillating force is sufficient to move a particle through the glycocalyx. Applying these forces to the nanoparticles increases the random walk that a particle undergoes, allowing it to take larger excursions than it would by diffusion alone. A particle would be able to traverse into and out of dense regions, escaping entrapment, and continuing on a path towards the cell membrane. Otherwise, without the additional force, the particle would remain caught.

This hypothesis could be tested through studies of nanoparticle transport through the glycocalyx, for which a methodology already exists. (Zhou, Xiong et al. 2011) Using the 130nm particles as a tracer the diffusion coefficient would be measured with and without magnetic force application.

5.5.11 Advantages to stimulating macropinocytosis and caveolae/lipid raft pathways

Stimulating macropinocytosis can be particularly beneficial for cell types that have been shown to achieve transfection via this pathway. (Goncalves, Mennesson et al.

2004; Zhang, Allen et al. 2011) This presents a way to target this pathway without the need for chemical modification to the vector. Macropinosomes also present a potentially larger vehicle for carrying non-viral vectors. Macropinosomes have been shown to range in diameter from 200nm to 10 μ m. (Hewlett, Prescott et al. 1994; Swanson 2008) Vesicles resulting from the clathrin and caveolae-mediated pathways are typically smaller than 200nm. (Nanbo, Imai et al. ; Rejman, Oberle et al. 2004) A macropinosome can contain a volume many orders of magnitude greater than these other vesicles, enabling many more vectors to be carried into the cell. In a previous study of macropinocytosis inhibition it has been shown that macropinocytosis is a slower acting process. (Zhang, Allen et al. 2011) This could be observed from the static only samples, which showed no difference when treated with amiloride. Since macropinocytosis is accounting for a significant portion of the enhancing effect, the oscillating force seems to increase the rate at which this pathway operates. This is potentially beneficial for *in vivo* applications where nucleases in the blood would degrade the genes. The oscillating forces could be thought of as adding free energy into this endocytic pathway, enabling it to occur at a greater rate than the energy output of the cell alone would allow.

It is advantageous to stimulate caveolae-mediated endocytosis because of the potential for achieving non-degradative delivery of the vectors. Common fates for endocytic vesicles are lysosomal degradation or recycling of the vesicle back to the cell membrane. (Mukherjee, Ghosh et al. 1997) Caveolae-mediated endocytosis has been found to produce some internalized vesicles that do not result in acidification and fusion with lysosomes. (Medina-Kauwe 2007; Kiss and Botos 2009) Nanoparticles and viruses have been found in non-degradative compartments after uptake via caveolae (Medina-

Kauwe 2007; Kiss and Botos 2009; Kim, Boylan et al. 2012) escaping lysosomal degradation. This makes possible an increased bioavailability of the non-viral vectors and gene constructs, and thus a more efficient delivery. Stimulating this pathway via oscillating force provides a method to target this pathway without the need for chemical modification to the vectors.

5.6 Conclusion

In conclusion, these data reveal that oscillating magnetic fields enhance nanoparticle transfection by stimulating macropinocytosis and caveolae/lipid raft pathways. Applying oscillating forces on nanoparticles is a way to target these pathways without specific ligand functionalization to the nanoparticle. Optimal enhancement occurs at 10Hz, although this may vary depending on the cell type. Oscillating a nanoparticle may be helping a nanoparticle reach lipid rafts and membrane ruffles by helping it to traverse the matrix of the glycocalyx. Oscillating a nanoparticle may allow it to make increased trans-membrane receptor protein attachments, signaling the uptake cascade to occur at a faster rate or with greater frequency across the cell. Macropinocytosis is not a contributor to expression levels during a 30 minute transfection, but, upon application of an oscillating magnetic field this pathway becomes highly active, doubling expression levels. Up-regulating a pathway that is largely ineffective over a short time scale could be the means to making transfection possible in cells that are resistant to vector uptake. Caveolae-mediated delivery is improved with applied oscillating force stimulation also, potentially leading more vectors down a non-degradative pathway. This is potentially important for *in vivo* applications due to the low efficiencies involved with delivery in complex physiological environments. Cells or

tissues previously resistant to vector or drug uptake could have pathways “activated” by the stimulation of oscillating forces, enhancing the effectiveness of the treatment. Drug resistance is an issue in cancer treatment (Gao, Zhang et al.) and opening alternative pathways for delivery could offer improved efficacy in treatment. There are many steps involved in each of the endocytic pathways so further study will be needed to pinpoint where the oscillating force is most critical. Continued studies will further elucidate the cellular mechanisms involved in magnetic nanoparticle delivery to realize its promise as a means of gene delivery for the treatment and possible curing of diseases.

Chapter 6

in vivo Molecular Motor Transport and Force Response

6.1 Introduction

Once a nanoparticle enters the lumen of the cell, it is subject to the mechanics of the intracellular environment. To characterize this environment, I have probed it with paramagnetic microbeads and manipulated them with a 3-dimensional force microscope. I developed a protocol to allow the microbeads to be internalized by the cells, when they would otherwise be size excluded. I verify the position of the bead within the cell via 3-D isosurfaces and tracking of intracellular active transport. I describe how external forces change the molecular motor transport of the beads and for the first time characterize the different observed phenomena. I have measured, for the first time, an approximate stall force on a 1 μ m bead *in vivo*, and estimate the maximum number of dynein molecules attached to it. My data demonstrate that the molecular motor transport behaves like a ratchet and gear, in that under maximal loads it can move only a set distance, but when it does so moves at the same velocity as an unloaded motor.

The intracellular environment was once believed to be akin to the water inside of a balloon. As techniques developed that enabled insight into the biochemistry of the cell, it was discovered that the cell was in fact an extremely dense and diverse environment. The cytoplasm of the cell consists of the cytoskeletal network, organelles, proteins, and cytosol. The intracellular transport must occur in this milieu in order to effectively distribute necessary components to different parts of the cell, and to control the distribution of organelles and cytoskeleton at different times of the cell cycle. Molecular motors are the machines that work to manage the different transportation needs of the cell.

The movement of organelles began being characterized back in the late sixties as researchers observed saltatory displacements in a variety of cell types. (Freed and Lebowitz 1970) The movement of organelles was shown to consist of long excursions that would frequently and rapidly change in direction and magnitude. It was established that microtubules were the primary cytoskeletal constituent involved in this organelle transport, as the transport ceased with treatment of microtubule de-polymerization drugs. Dynein and kinesin are the primary motor proteins associated with microtubule based transport. Later studies would show that myosin via actin filaments was involved in organelle transport, though to a much lesser extent (Kulic, Brown et al. 2008) compared to microtubules. The introduction of *in vitro* motility assays provided a novel and useful platform from which motor transport could be studied. (Sheetz and Spudich 1983) In these systems, cytoskeletal filaments are purified and deposited onto a glass coverslip. Motor coated microbeads can be introduced to this coverslip and in the presence of ATP will undergo transport along these filaments. These studies showed that both kinesin and

dynein were both processive motors (Reck-Peterson, Yildiz et al. 2006) along with some members of the myosin family of proteins. (Rosenfeld and Lee Sweeney 2004) The processivity of a motor refers to the ability of a single motor to walk along a filament with multiple steps without detaching. This system also allows forces to be applied to the motor coated beads to observe the change in behavior of the motor with respect to applied loads. (Svoboda and Block 1994)

Kinesin and dynein motors are proteins that drive intracellular transport along microtubules. Each motor has 2 binding domains that have the ability to bind to tubule monomers in the microtubule. To describe the functioning of the motor, I will start with both domains of the motor attached to the microtubule. A domain of the motors, above the binding arms, binds ATP and is responsible for ATP hydrolysis. This hydrolysis reaction causes the motor to undergo a conformational change (working stroke) which results in the rear binding domain detaching from the microtubule. After this detachment the free binding domain progresses to the next binding site along the microtubule (recovery stroke). This free domain then binds again to the microtubule, completing the cycle. Repeating these steps allows a transported cargo along a microtubule, provided there is sufficient ATP, as governed by equations 6.1 and 6.2.



$$K_{eq} = \frac{[ADP]_{eq}[P_i]_{eq}}{[ATP]_{eq}} = 4.9 \times 10^5 M \quad (6.2)$$

The term K_{eq} is the equilibrium constant of the comprised of the concentrations of adenosine diphosphate (ADP) and inorganic phosphate groups (P_i).

Kinesin and dynein will work in concert to transport organelles throughout the intracellular environment. Kinesin transport is characterized as anterograde, as its

movement is in the direction of the plus-end of the microtubule, away from the nucleus. Dynein transport is characterized as retrograde, as it transports movements towards the negative end of the microtubule, towards the nucleus. The *in vitro* speeds for kinesin and dynein have been shown to be 840 and 1250nm/s respectively. (Howard 2001) The *in vivo* speeds for kinesin and dynein have been shown to be 1800 and 1100nm/s respectively. These values represent the speeds of the motors in the absence of an external load.

To achieve this transport the motors must generate a force. *In vitro* assays allow step sizes and forces to be measured through a number of modalities, including atomic force microscopes (AFM) and optical tweezers. As stated before, the average step size of both motors is shown to be 8nm but it has been shown that step sizes can vary by factors of this step size. Gelfand et al. showed that motors could take steps of 16, 24, 32, and more, which corresponds with the lengths of multiple 8nm tubulin monomers. (Kural, Serpinskaya et al. 2007) The force exerted by an individual kinesin protein has been determined to be approximately 6 pN (Howard 2001) with other studies reporting forces between 4 and 8 pN. The force exerted by an individual dynein motor has been shown to be in somewhat similar range, with report values as low as 1.1pN (Mallik, Carter et al. 2004) and up to 7 pN. (Gennerich, Carter et al. 2007) One common hypothesis as to how these motors manage to transport cargoes through the cytoplasm is the shared load model. In this model the load is distributed among several different motors, enabling greater forces to be generated as a collective unit. As stated previously both motors act on the load to move the cargo in a bi-directional manner. The mechanism for the “decision” of directionality is not clear in the current understanding of the field. Several theories have

been proposed to explain the cooperative nature of the motors. (Jolly and Gelfand 2011)

The theories are different but not necessarily mutually exclusive. One theory suggests that recruitment, the binding of molecules, is the deciding factor as to which direction the load will travel. The motor protein with the greater number of recruits will transport the load preferentially in the characteristic direction of that motor. Another mechanism suggests that there is some manner of crosstalk between the motors that communicates when transport needs to occur in a particular direction. One theory proposes that there is some type of motor coordinating complex that governs the switching of motors. A fourth model suggests that there is a regulating stochastic mechanism that controls the motor activation or inactivation based on binding of different constituents or modifications to the motors. These questions are still an area of great research interest and the answer is still sought.

While *in vitro* motor stalling has been successfully achieved, *in vivo* stalling has proven a more challenging proposition. Optical tweezers have been widely used in *in vitro* studies and employed in some *in vivo* studies, but there have been challenges. Optical tweezers have been shown to be damaging to cells even with low power levels. (Banerjee, Chowdhury et al.) Determining the force on an object depends on the size of the object trapped and vesicles/organelles inside of a cell can vary greatly in size. Attempting to track vesicles *in vivo* requires quick identification and focusing of the vesicle on the center of the target. Some of these issues can be dealt with but the fact remains that lasers are damaging to cells, making optical tweezers a less than optimal modality. In this chapter I present a study of intracellular microbead manipulation by way of 3-dimensional force microscopy. I demonstrate the protocol for introducing 1 μ m

paramagnetic polystyrene beads into the intracellular environment. I will show that the microbeads undergo bi-directional active transport and describe the different phenomena that are observed when forces are applied *in vivo*. I will show attempts to stall the microbead transport and the forces that are measured to achieve this.

6.2 Intracellular Constituents

This section will give a brief overview of some of the specific components of the cytoskeleton which contribute to the structure of the cell and provide for intracellular transport. It will describe several of the major organelles to give a general view for the many constituents of the environment.

6.2.1 Actin

The actin network provides the cell with an underlying structure that provides the framework for the cell as well as a means for the cell to stretch and move around in its environment. Actin monomers polymerize into long filaments which can wrap around each other in a helical fashion in a process called treadmilling. These polymers are generally 5-9nm in diameter. In the cytoskeleton the filaments combine into protofilaments that are connected end to end and lateral associations. Larger filaments combine into stress fibers which can span larger lengths of the cell providing structural integrity.

Although actin filaments are dispersed throughout the cytoplasm, a substantial layer of actin exists underneath the cell membrane called cortical actin. (Alberts, Johnson et al. 2002) This actin rich cortex allows the cell to adhere to a substrate and stretch out across it. This actin forms protrusions called filopodia and lamellipodia which allow it to

sense around its immediate environment and migrate to different parts of the environment. Actin is also involved in various phases of multiple endocytosis pathways.

6.2.2 Microtubules

Microtubules are hollow tube-like structures of the cytoplasm. (Alberts, Johnson et al. 2002) A single microtubule is composed of a total of 13 protofilaments, each comprised of individual α and β tubulin monomers, alternately arranged. These protofilaments connect laterally to one another and wrap around in a cylindrical conformation of about 25nm diameter. The microtubule network stretches throughout the cell, organizing around foci called microtubule organizing centers (MTOCs). These MTOCs are situated in perinuclear locations in the cell and the network extends from the center to the periphery of the cell.

The microtubule network provides the pathways along which organelles are able to move through the different regions of the cell. Organelles such as mitochondria and lysosomes are able to be transported along the microtubules through the action of molecular motors attached through them. The cell is able to transport necessary constituents to various part of the cell as well as reorganize the distribution of organelles via this transport system. The microtubules are shown to polymerize and de-polymerize at opposite ends causing microtubule to grow or shrink as befitting the needs of the cell. This phenomenon is known as dynamic instability.

6.2.3 Intermediate Filaments

A third type of cytoskeletal polymer is the intermediate filament. (Alberts, Johnson et al. 2002) This structure is less prevalent than the previous two but still found

in many metazoan cell types. Intermediate filaments are ropelike fibers of 10nm diameter. The subunits of intermediate filaments are comprised of two coiled-coil dimers of a 48nm polypeptide. These subunits attach linearly and laterally and twist into a ropelike filament.

These filaments are involved in providing structural reinforcement to the cell. They have been shown to span the length of the cytoplasm, forming bonds with adjacent cells, giving increased structural integrity to a layer of cells. Other filaments have been shown to provide structure to the cell nucleus.

Organelles in the cell each contribute a unique function to the cell. In order for a cell to exist, numerous tasks must be performed to sustain the cell. As with complex organisms such as mammals, a single cell must consume nutrients and eliminate waste.

6.2.4 Organelles

The intracellular environment is divided into a wide variety of membrane bound compartments called organelles. Each organelle type possesses its own unique characteristics which allow them to perform their respective functions. The nucleus is the largest organelle which is responsible for containing the genome of the cell, protecting it from damage or degradation. It provides an environment for transcription to occur. The endoplasmic reticulum is an organelle that forms a network surrounding the nucleus. The ER is involved in protein synthesis and membrane production. Mitochondria are involved in the production of ATP, a source of energy for the cells. Lysosomes and peroxisomes are responsible for the breakdown of foreign materials and wastes in the cell. Ribosomes read mRNA transcripts to produce peptides and proteins. The Golgi

body is responsible for the packaging of proteins for subsequent transport within the cell as well as outside of the cell. These are several of the major organelles in the cell and are by no means an exhaustive list. There are many others in the intracellular environment that account for all of the various functions that are needed for a cell to survive. When probing the rheology and transport phenomenon of this environment all of these constituents have an effect on the observed phenomenon. Molecular motors transport organelles through an environment packed with organelles, proteins, cytoskeleton, sugars, and many other components which affect the observed phenomenon.

6.3 Process of Microbead Internalization and Intracellular Fate

I have not determined the specific endocytic pathway that the 1 μ m microbead takes to gain entry into the cell but subsequent sections will describe the verification of the internalization of the bead. The process of internalization can be thought of in 3 general steps illustrated in Figure 6.1.

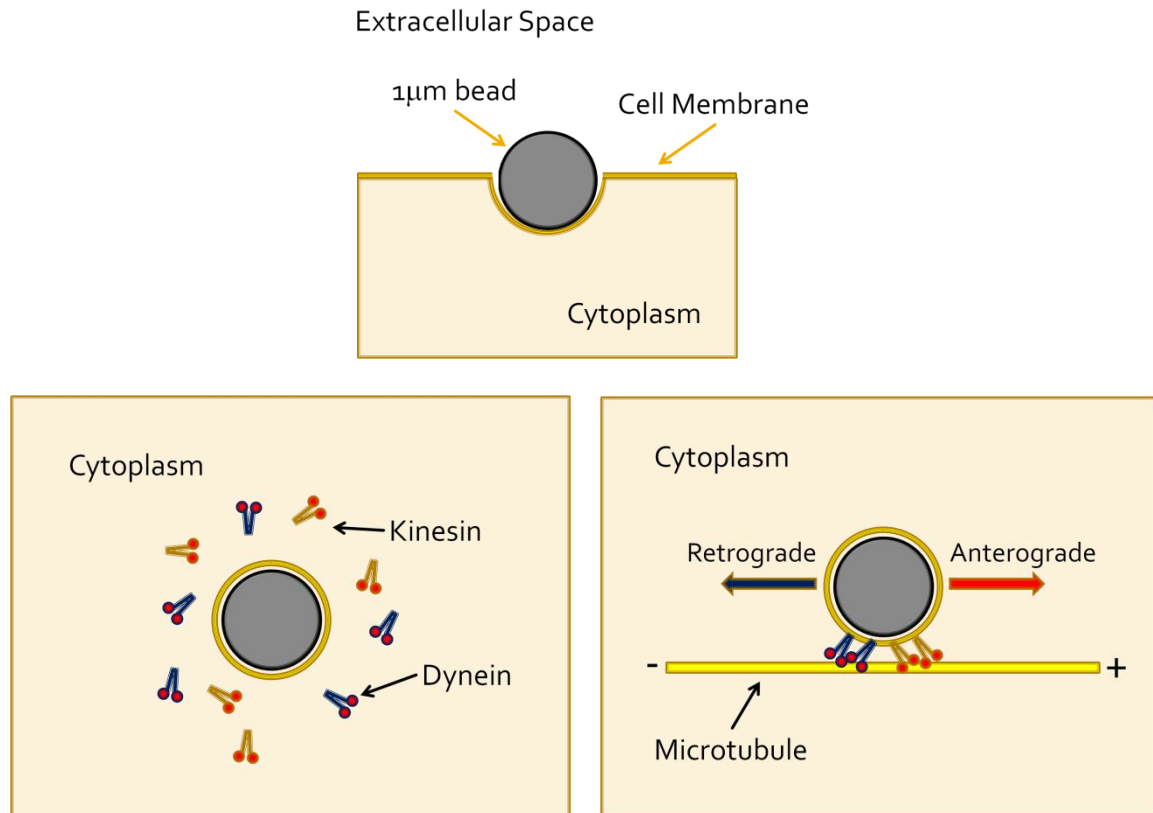


Figure 6.1 Generalized process of 1 μ m microbead uptake. Top Right: A bead contacts the cell membrane and begins the process of invagination until it is fully engulfed. Bottom Left: Bead is inside of pinched off portion of vesicle forming an endosome. Molecular motors in the cytoplasm attach to the outside of the vesicle. Bottom Right: The bead is then able to undergo transport along microtubules.

First, the bead comes into contact with the cell membrane, thus initiating the process of internalization. The uptake of the bead begins when the cell membrane begins to invaginate until the point that the bead is fully encapsulated by the cell. At a certain point the encapsulating membrane is pinched off, often by a combination of motor proteins and actin working in concert, to become a vesicle in the cell called an endosome. Motor proteins dynein and kinesin are floating around the cytoplasm and attach to the outer membrane. This endosome can eventually come into contact with one of the many microtubules contained within the cell for organelle transport and intracellular re-organization. Once the motors on the endosome come into contact with the microtubules

the microbead will undergo active transport along the microtubule network just like the other organelles in the cell.

6.4 Molecular Motor Transport Experiments

To characterize the rheology of the interior of the cell, I developed a protocol to introduce a probe into the cytoplasm of the cell. One micron paramagnetic beads are specially functionalized to promote uptake into the cells. Once inside, they can be visually tracked and manipulated with the 3-dimensional force microscope.

6.4.1 1 μ m Microsphere Functionalization to Achieve Internalization

Dynabeads Tosyl-activated MyOne beads (Invitrogen, Carlsbad, CA) were used in experiments for intracellular cell studies. These beads are 1 μ m diameter uniform microspheres. They are comprised of highly cross-linked polystyrene with interspersed magnetic material. The surface of the microspheres are available functionalizations of carboxylic acid, amino groups, streptavidin, and tosyl groups, making it ideal for a variety of secondary functionalizations. Scanning electron microscope images were taken to verify the uniformity of size of the MyOne beads, as shown in Figure 6.2.

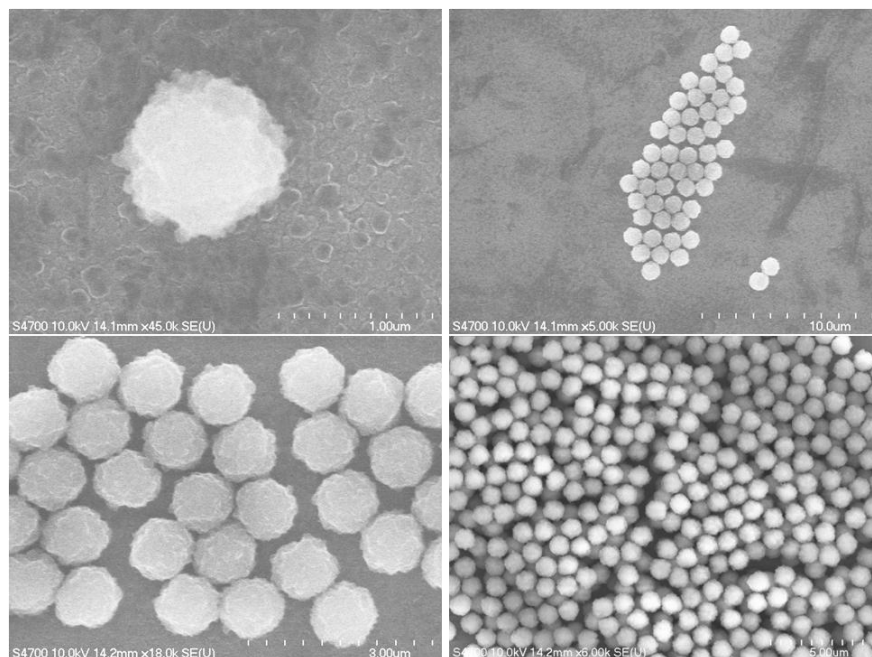


Figure 6.2 SEM micrographs demonstrate the highly uniform, spherical shape of the entire population.

The tosyl-activated MyOne beads were used in experiments for intracellular cell studies. The surface of the beads is functionalized with p-Toluene-sulfonyl groups making it extremely useful for binding with a variety of molecules. These beads were used for labeling with the Alexa Fluor® hydrazide fluorescent stains. The MyOne tosyl-activated super-paramagnetic beads were functionalized with Alexa Fluor® 568 hydrazide to make them visible through fluorescence microscopy. A volume of 100µl of Alexa Fluor® 568 hydrazide (100 µM) solution is added to 20 µl of 100 mg/ml MyOne tosyl-activated beads. This mixture is vortexed and placed on a rotator for 4 hours. The beads are spun down in a centrifuge at 4000 rpm, supernatant is removed, and the beads are re-suspended in 1 ml of PBS. This washing step is performed twice. Fluorescent

microscopy was used to verify the labeling of the beads with the Alexafluor, as shown in Figure 6.3.

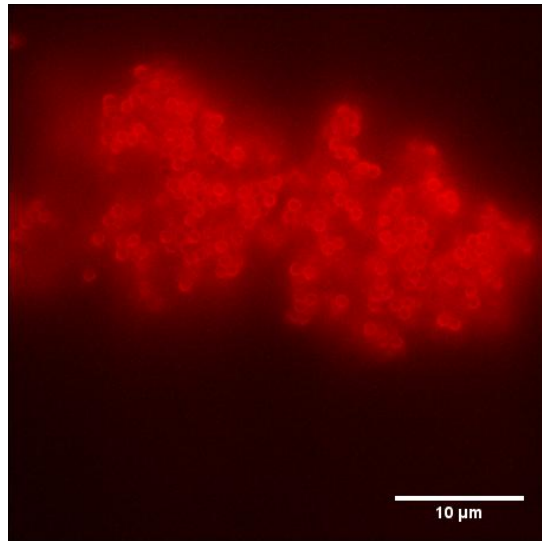


Figure 6.3 1 μ m MyOne Tosyl-activated beads fluorescently labeled with Alexafluor 568

To stimulate uptake of the beads into the cells, Lipofectamine 2000 transfection reagent is added to the beads. Twenty microliters of Lipofectamine 2000 is added to the fluorescently labeled samples. The sample is vortexed and placed on a rotator overnight. Section 6.4.2 and 6.4.3 will describe the verification of transport and internalization of the beads. This protocol was shown to introduce the MyOne beads into cytoplasm of HeLa cells. The tosyl-activated beads, unmodified, do not experience uptake into the cells. The treatment of the microbeads is a necessary step to achieve internalization. This treatment has the added benefit of minimizing the amount of excess beads attached to the glass providing for a cleaner sample. When the media is changed prior to imaging it is observed that there are almost no beads attached to the glass and all of the beads are associated with the cells. Conversely, without functionalization, there are a high number of beads associated with the glass, and essentially none associated with the cells.

6.4.2 Microbeads are Tracked and Mean-Squared Displacement Can Show Driven vs. Passive Transport

Video is tracked with Video Spot Tracker (<http://cismm.cs.unc.edu/downloads/>) and edited in MATLAB. A script called evt_GUI allows the data to be analyzed and plots of the tracks to be produced. Among other analysis tools the program allows us to produce plots of mean-squared displacement (MSD). Mean-squared displacement is a measure of the spatial extent of random motion. It is a measure of the displacement squared versus the change in time ($\tau = \Delta t$). The MSD is determined mathematically by Equation 6.3.

$$MSD(\Delta t) = \{[x(t + \Delta t) - x(t)]^2\} \quad (6.3)$$

where x is the position of the bead and t is time. The plot of MSD can be used to characterize the type of observed movement in the experiment (Kulic, Brown et al. 2008). The slope of an MSD curve reveals information about the displacement of the bead. The slope in log-log space of an MSD plot is indicative of purely diffusive motions. A slope between 0 and 1 is indicative of sub-diffusive behavior whereas a slope between 1 and 2 is indicative of driven, sub-ballistic behavior. A slope very close to 2 would be considered ballistic motion. Applying this analysis to the tracks we can judge the type of motions that are observed in the internalized $1\mu\text{m}$ beads. An example a radial displacement of a transported bead is shown in the left column of Figure 6.4. On the right column is the track of a bead in the same field of view that is stuck to the glass. Below each is the respective plot of mean squared displacement.

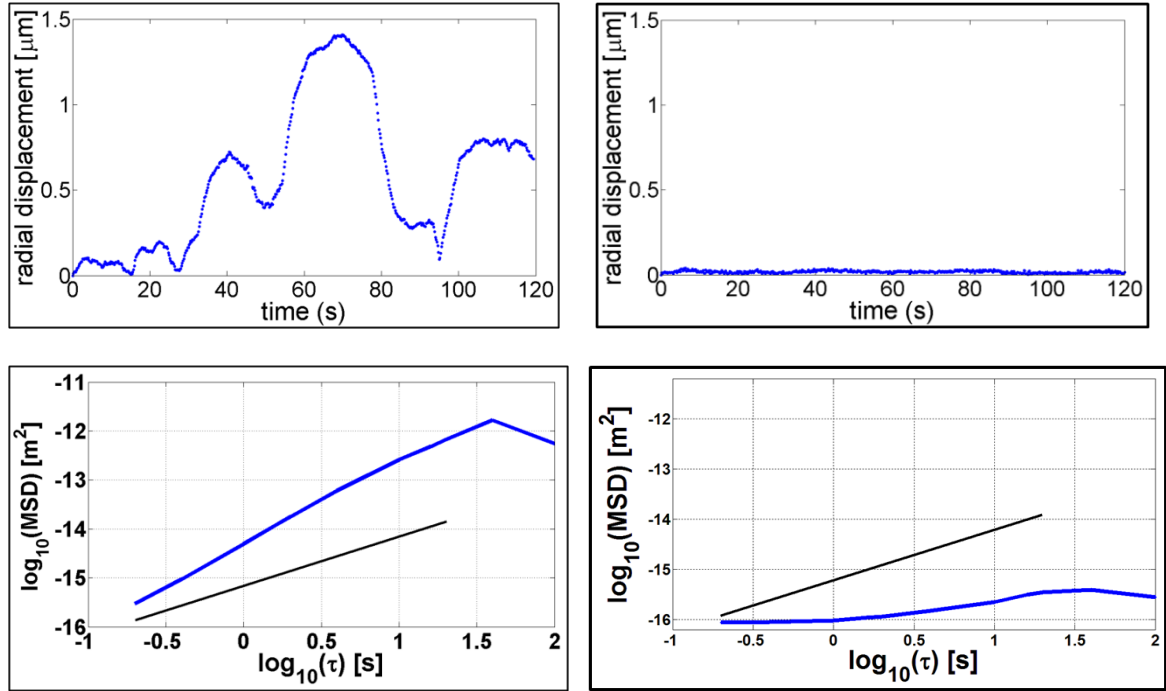
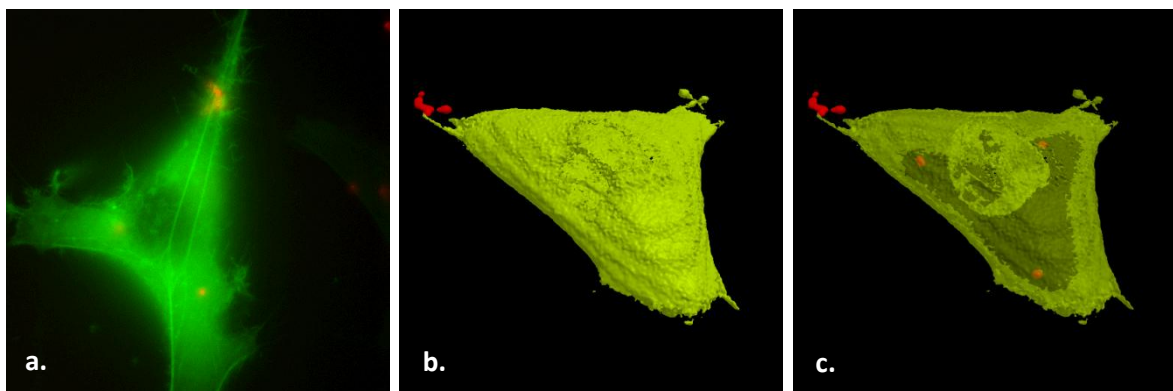


Figure 6.4 Left column shows the radial displacement plot of an internalized $1\mu\text{m}$ bead along with plot of MSD. The right column shows the same type of data for a $1\mu\text{m}$ bead that is stuck to the glass. Data are shown in blue. In both MSD plots, a line of slope = 1 is shown in black. The internalized bead has a slope greater than one ($m = 1.63$), confirming the active transport. The bead stuck to the glass substrate shows a slope less than 1 ($m = 0.6$), showing that it is not diffusing or transporting in any way.

The transported bead shows a clear distinction from the stuck bead. The bi-directional transport can be seen in the radial displacement plot. The slope of the MSD plot is shown to be 1.63, in the sub-ballistic, driven transport regime. The stuck bead shows no long-scale displacement which is also shown in its MSD plot, where the slope of the curve is 0.6, well within the sub-diffusive range. It is clearly possible then to distinguish which beads are undergoing active transport from ones that are not using this methodology.

6.4.3 3-D Isosurfaces Can Show the Position of the Microbead and Verify Internalization

To visualize the internalization of the beads by the cells, HeLa wild types cells were transfected with Fluorescent Protein Cellular Labels: Cellular Lights™ Reagents. These reagents use baculoviruses to introduce DNA into the host cell that codes for the cytoskeletal monomer subunits with an attached fluorescent protein. Cells were transfected with a GFP-Actin actin according to the manufacturer's guidelines, and results were verified with fluorescence microscopy. Stacks were taken on the Nikon epifluorescence microscope described previously. The images in the stacks were taken in green and red and red channels consecutively at each z-height. The stacks were then modeled into a 3D isosurface using Image Surfer software from CISMM (<http://cismm.cs.unc.edu/downloads/>). The models depict the positioning of the beads relative to the membrane of the cell. We are able to identify beads that are being transported by the cell and the 3D models can confirm that the beads are inside of the cell.



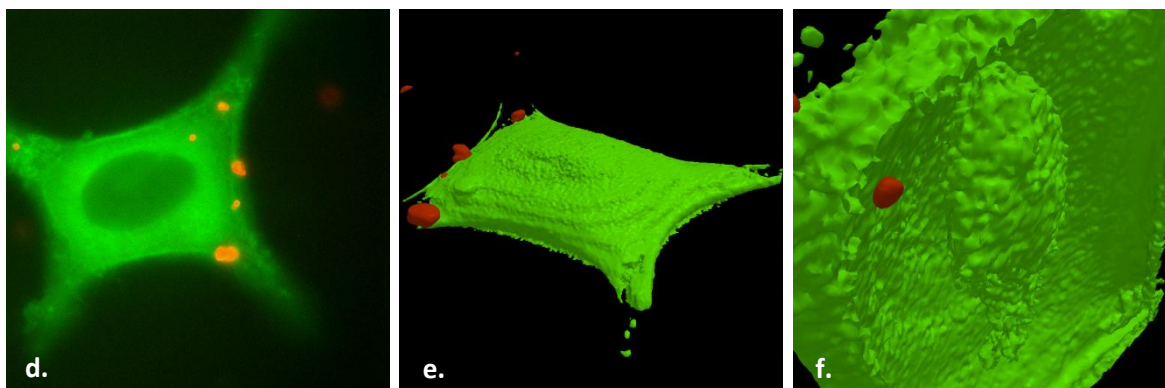


Figure 6.5 (a) Slice from a red-green stack of HeLa GFP-Actin cell and Alexa Fluor Hydrazide 568 beads. (b) Isosurface of combined red-green stack from ImageSurfer. (c) Same isosurface as b. with the opacity of the green channel reduced. Red 1 μ m beads can be seen inside of the isosurface. (d) Slice taken from another stack of a different cell. (e) Isosurface of d. (f) View of isosurface from underneath the cell. The 1 μ m bead can be seen beneath the outer membrane in proximity to the nucleus.

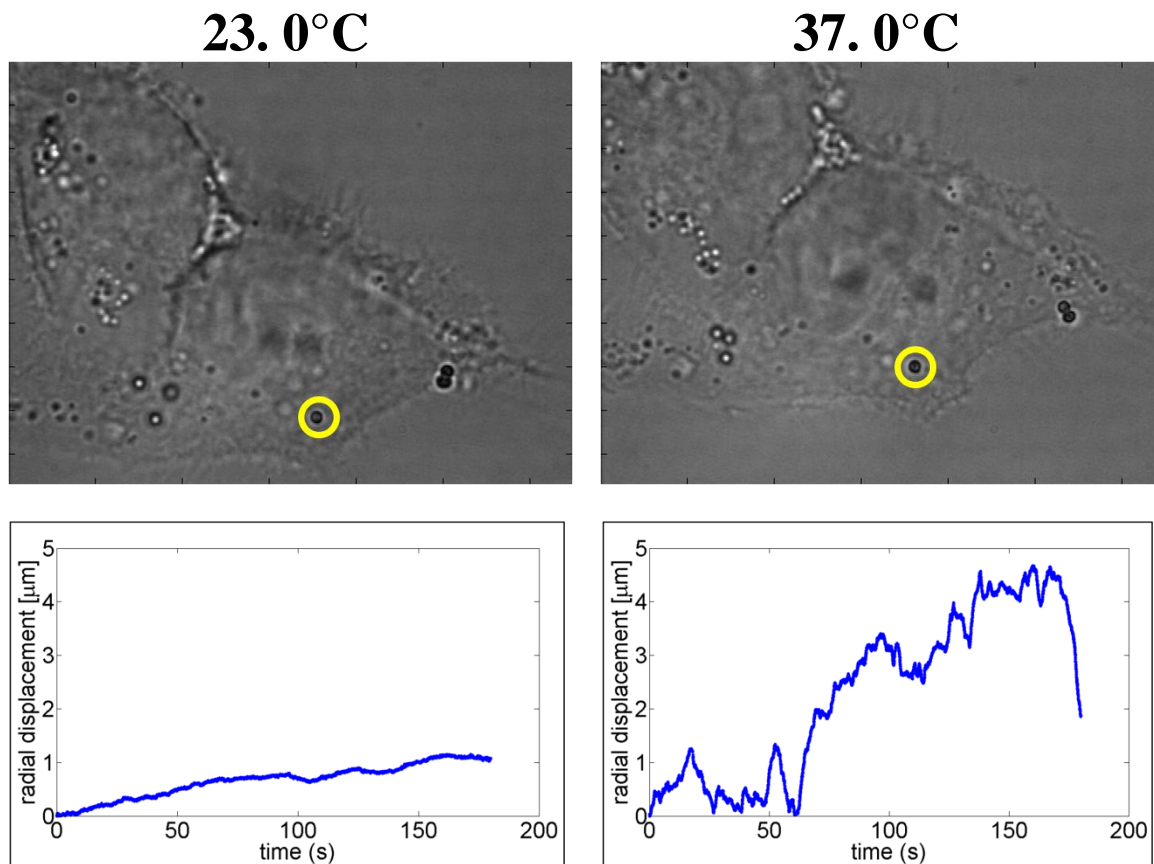
The isosurfaces depicted in Figure 6.5 show two examples of a bead internalized in a cell. The images in the left column are slices from the respective z-stacks. The middle column of the figure shows the two stacks merged and rendered into an isosurface. The top right image (c.) shows the isosurface of the top cell with the opacity of the green channel reduced so that the area beneath the membrane is visible. The nucleus is visible and the red fluorescent 1 micron bead is visible at the lower right. The bottom right image (e.) shows the isosurface rotated and so that the region underneath the membrane is visible. The 1 micron bead can be clearly seen in proximity to the nucleus. Images like this confirm that the beads we identify as undergoing active transport are indeed internalized within the cell, and are suitable candidates for probing the intracellular environment.

6.4.4 Active Microbead Transport is Temperature Dependent

The temperature dependence of organelle active transport was established in the seventies with the study of abdominal nerves of *rhodnius prolixus* (Heslop and Howes

1977). This temperature dependence is also evident in the transport of the 1 micron microbeads. Cells were plated as described above in section 6.3.2 and dosed with microbeads.

A single cell with an internalized bead being actively transported was identified. Video of this cell is captured at 60fps. Video is first captured at room temperature, 23.0°C. Later, the cell culture temperature is raised to 37.0°C to observe the difference in active transport. The results are shown in Figure 6.6.



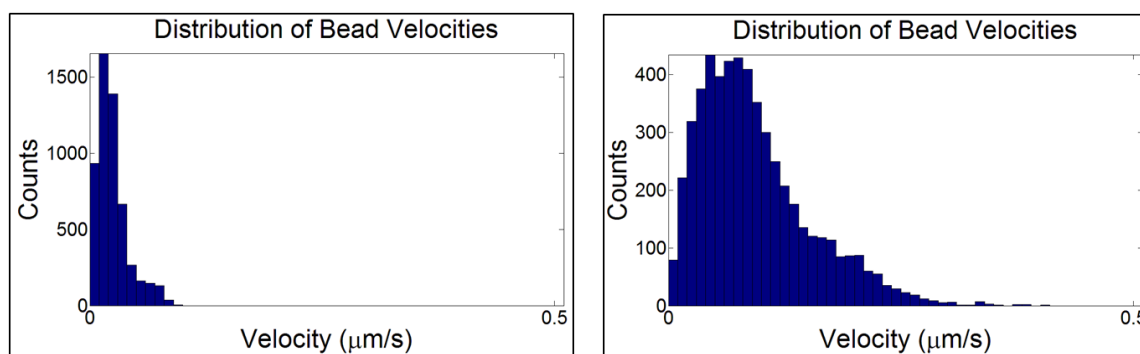


Figure 6.6 Results from the temperature dependence of transport on a single microbead in the same cell. The top two images are frames taken from the 60fps time-lapse. The yellow circles indicate the same bead undergoing transport at the two temperature regimes. Below the time-lapse images are the respective radial displacement plots. The difference in transport between the two is significant, with the 23.0°C track showing essentially none of the bi-directional transport indicative of motor transport. The 37.0°C sample shows a greatly increased level of activity.

The temperature dependence is clearly shown in the radial displacement plots. Tracking the microbead at 23.0°C showed very minimal displacement from the original displacement, especially when compared to the 37.0°C. The 23.0°C sample displaced essentially 1 micron from its original position, whereas the 37.0°C displaced as much as 5 microns from its original position and traveled a total distance of over 10 microns.

Data are taken and analysis is done on $n = 17$ and $n = 21$ beads for 23.0°C and 37.0°C respectively. The mean displacements, velocities, and excursion times are calculated to further characterize the temperature dependence on active transport. Displacements are characterized as anterograde or retrograde based on the direction the bead is moving relative to the nucleus. Anterograde transport involves movement away from the nucleus and retrograde displacement involves movement towards the nucleus. An “excursion” is characterized as a persistent displacement of the bead until the velocity of the bead equals zero. When the bead resumes transport, that movement is counted as a

new excursion. For each of excursion the displacement, velocity, and excursion time is measured. The results are shown in Figure 6.7 and Table 6.1.

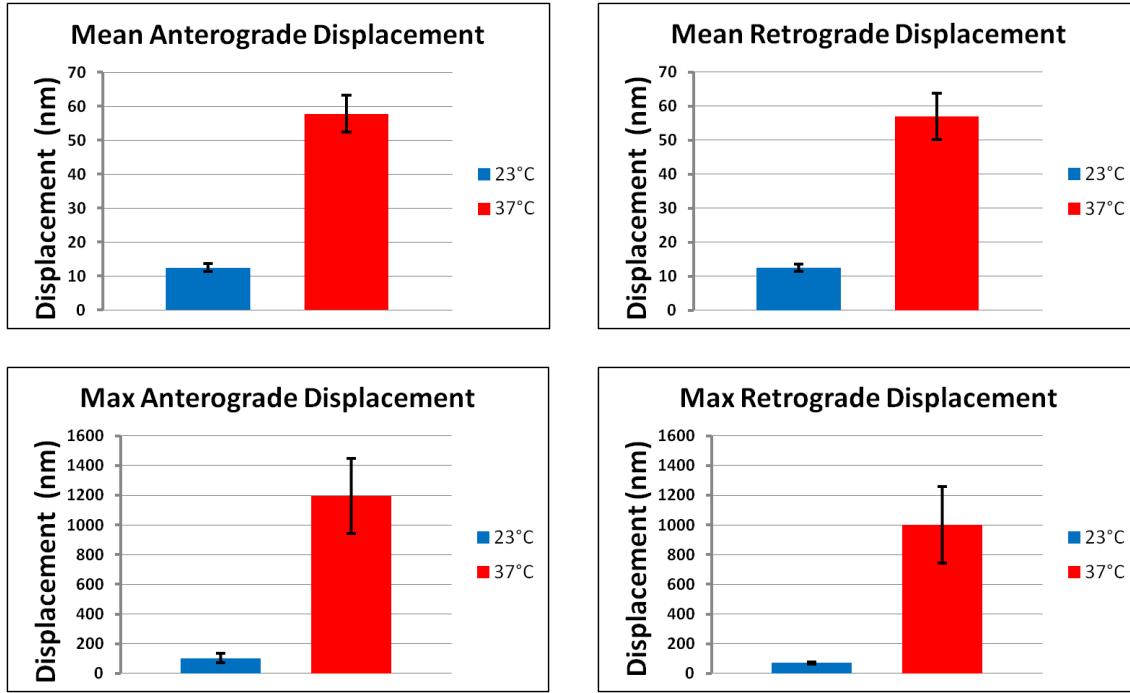
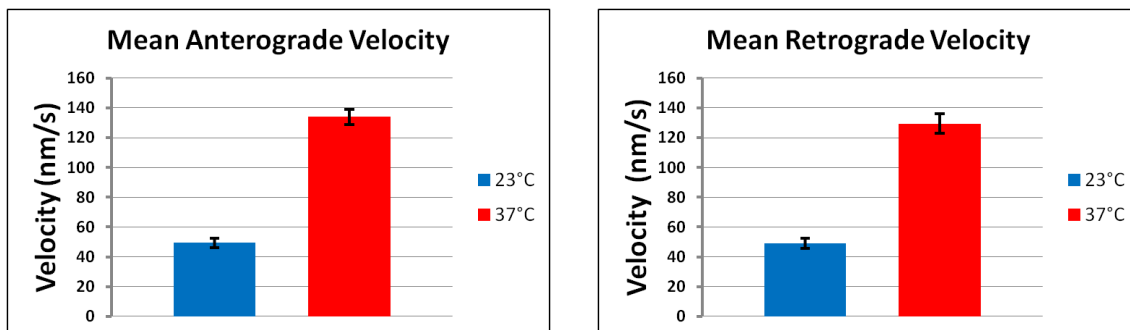


Figure 6.7a Intracellular 1 μ m microspheres undergo active transport at 23.0°C and 37.0°C. Shown are plots of mean and max anterograde/retrograde velocity.



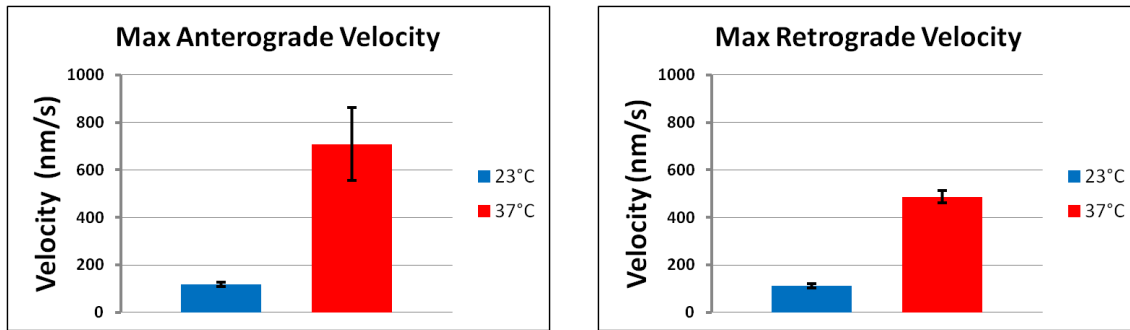


Figure 6.7b Intracellular 1 μ m microspheres undergo active transport at 23.0°C and 37.0°C. Shown are plots of mean and max anterograde/retrograde velocity.

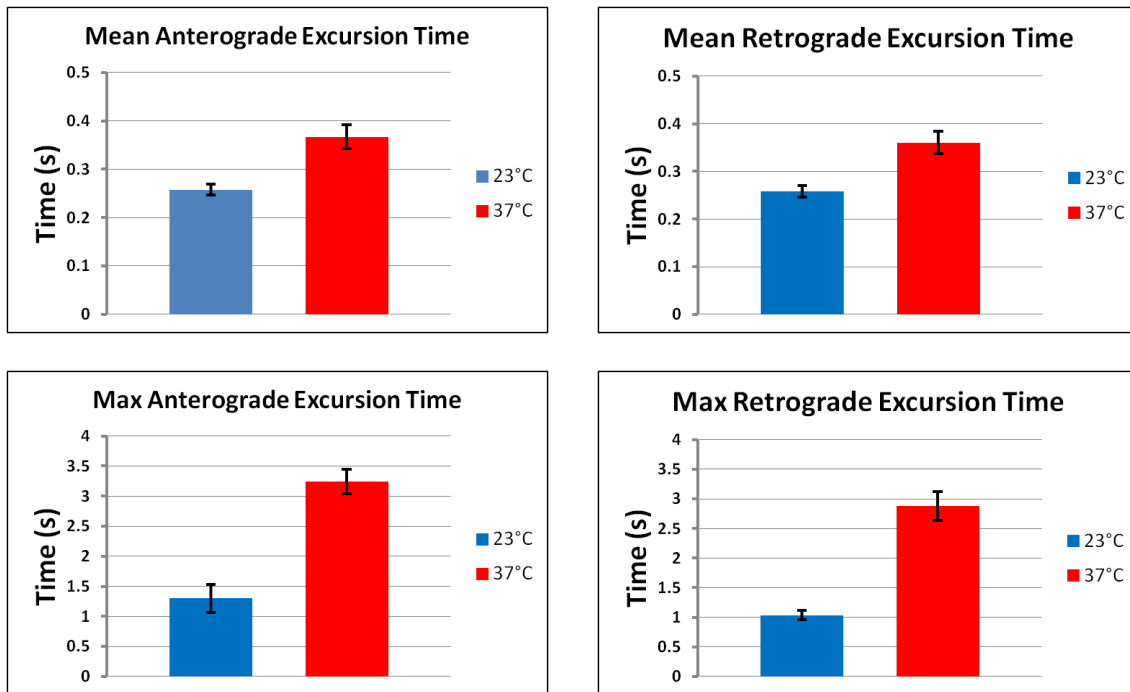


Figure 6.7c Intracellular 1 μ m microspheres undergo active transport at 23.0°C and 37.0°C. Shown are plots of mean and max anterograde/retrograde excursion time.

Table 6.1: Displacements/velocities/excursion times for intracellular transport of 1µm microbeads at 23.0°C and 37.0°C			
	23.0°C	37.0°C	% Increase
Mean Anterograde Displacement	12.5 ± 1.1	57.7 ± 5.4	363%
Max Anterograde Displacement	103.1 ± 30.4	1194 ± 253	253%
Mean Anterograde Velocity	49.5 ± 3.17	133.9 ± 5.1	170.7%
Max Anterograde Velocity	118.4 ± 8.4	708 ± 153.5	497.7%
Mean Anterograde Excursion Time	0.26 ± 0.01	0.37 ± 0.02	42.4%
Max Anterograde Excursion Time	1.3 ± 0.23	3.24 ± 0.2	149.6%
Mean Retrograde Displacement	12.5 ± 1.1	56.9 ± 6.78	354.1%
Max Retrograde Displacement	70.5 ± 6.45	1000 ± 6.78	1320%
Mean Retrograde Velocity	49.1 ± 3.4	129.4 ± 6.45	163.8%
Max Retrograde Velocity	113.4 ± 9.2	687.5 ± 1.4	507.0%
Mean Retrograde Excursion Time	0.26 ± 0.1	0.36 ± 0.02	39.4%
Max Retrograde Excursion Time	1.04 ± 0.1	2.87 ± 0.24	177.6%

The mean and max displacements, velocities, and excursion times all experience significant increases at 37.0°C over 23.0°C. Mean displacements increased by greater than 350% along with excursion times seeing an improvement of 150% and greater. The temperature dependence is clear and significant and must be taken into account in the planning of intracellular rheology experiments.

6.4.5 The Probability Distribution of a Diffusing Bead Shows that the Microbead Transport is Active

A microbead in a sample can be observed undergoing movements due to thermal fluctuations which will cause it to displace due to the motions of the surrounding fluid. This phenomenon is referred to as diffusion. All things being equal, a particle will move in any direction from its equilibrium position with an equal probability to diffuse in any direction. The amount diffusivity of a particle in a fluid is quantified by a constant of proportionality called the diffusion coefficient. It is defined mathematically by Equation 6.1

$$D = \frac{kT}{\gamma} \quad (6.1)$$

where k is the Boltzmann constant, T is temperature in K , and γ is the drag coefficient. The drag coefficient is a value that is proportional to the velocity (v) a particle will experience given an applied force (F), as shown in equation 6.2.

$$F = \gamma v \quad (6.2)$$

For a spherical particle the drag coefficient is defined as:

$$\gamma = 6\pi\eta r \quad (6.3)$$

where η is the viscosity ($\text{Pa}\cdot\text{s}$) of the fluid and r is the radius (m) of the spherical particle. Substituting this into equation yields an alternative equation for the diffusion coefficient in Equation 6.4

$$D = \frac{kT}{6\pi\eta r} \quad (6.4)$$

The intracellular environment is a very heterogeneous environment. Unlike a Newtonian fluid, no single value of viscosity would be accurate to describe the fluid nature of the

cell. The intracellular environment is constantly remodeling, moving, and changing such that assigning a single viscosity value to a cell is insufficient for characterizing the fluid nature.

For the purposes of determining active transport we can determine the diffusion coefficient based on experimentally determined values of viscosity. With methods that will be demonstrated in Chapter 7, we can determine a value of intracellular viscosity to be 0.69 Pa·s. This value is determined from a single HeLa EGFP-654 cell and it should be stated again that this value can vary from cell to cell and within the same cell. But this value is within the range of viscosity for this cell type that will be shown later. Inserting this value into equation 6.4 yields a diffusion constant of:

$$D = 6.58 \times 10^{-3} \mu m^2/s \quad (6.5)$$

This value correlates the size of the particle and the frequency of the diffusive step sizes that are indicative of the random motions. The higher the diffusion constant, the greater the amount of diffusion will be observed in a system. This is evident when observing increased diffusion in solutions of high temperature and low viscosity. Also the smaller the particle, the more it will diffuse in the same system.

A microbead that is undergoing active transport in a cell is transported along filaments of the cytoskeleton, primarily microtubules. Given the size of the microbead and the vertical height of the cell, it is largely restricted to a 2-dimensional plane to move in, which relatively limited movement in the z-direction. When considering individual movements along a cytoskeletal filament, we can consider the movements to be 1-dimensional, with movement being either anterograde or retrograde. So for simplification we can look at this as a one-dimensional problem, and compare the

microbead movements with diffusion in 1 dimension. If a particle is diffusing in 1 dimension it has only two directions for displacement to occur. Because the diffusion is random, there is a probability associated with finding the particle at some position x from its starting point after a given time t . This probability is defined by the distribution function in Equation 6.6:

$$p(x, t) = \frac{1}{\sqrt{4\pi Dt}} e^{-\frac{x^2}{4Dt}} \quad t > 0 \quad (6.6)$$

where D is the previously defined diffusion coefficient, t is time, and x is the particle displacement. If a particle is observed moving in a system, if it is undergoing diffusion, it should not, on average, undergo average displacements beyond what is typical of the above distribution. Of course the longer a particle is diffusing, the further more chance it has to move farther distances. Using the diffusion coefficient in Eq. 6.5, we can see that change when considering time scales of 0.1, 1.0, and 10 seconds. The probability distributions are shown in Figure 6.8.

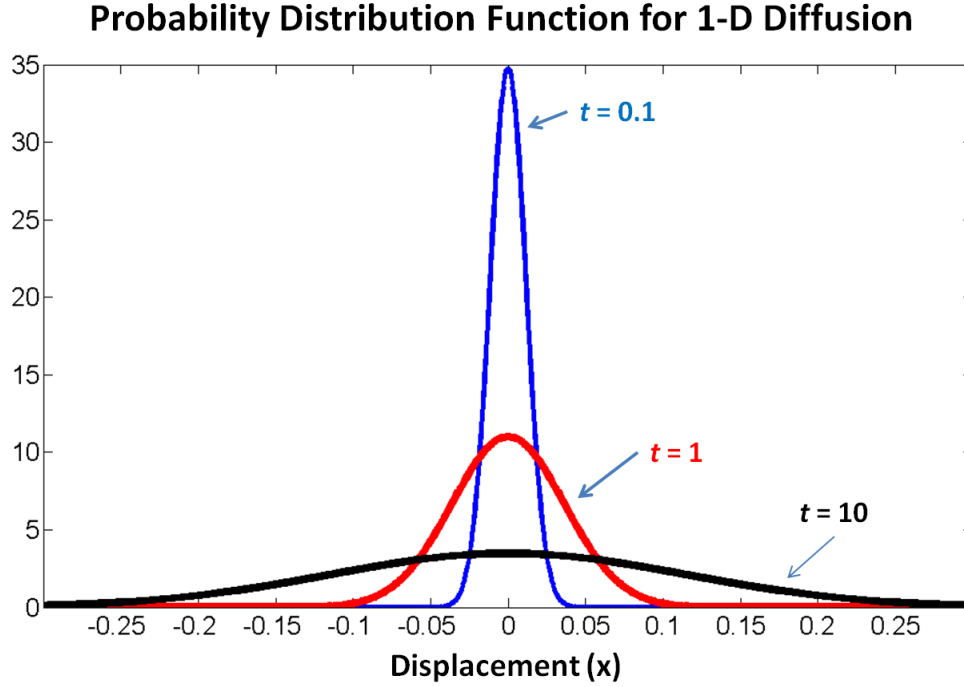


Figure 6.8 Probability distribution functions for 1-D diffusion of a bead for a 1 μm bead with diffusion coefficient of 6.58×10^{-3} . The times indicated are 0.1, 1, and 10 seconds. As a particle has more time to diffuse, it is likelier to traverse a greater distance.

As the microbead has more time to diffuse, of course there is greater probability of it displacing farther distances, as indicated by the above plots. It was shown that the mean anterograde displacement is 57.7nm with a mean excursion time of 0.37s. Plugging this time into the distribution, we can calculate the probability that the bead would diffuse this distance over this time scale. Setting the limits of integration appropriately, we integrate as shown in equation 6.7.

$$2 \int_{0.0577}^{\infty} \frac{1}{\sqrt{4\pi \times 6.58 \times 10^{-3} \times 0.37}} e^{-\frac{x^2}{4 \times 6.58 \times 10^{-3} \times 0.37}} dx \quad (6.7)$$

The integration is multiplied by 2 to calculate the 2-tailed probability, shown in Figure 6.9.

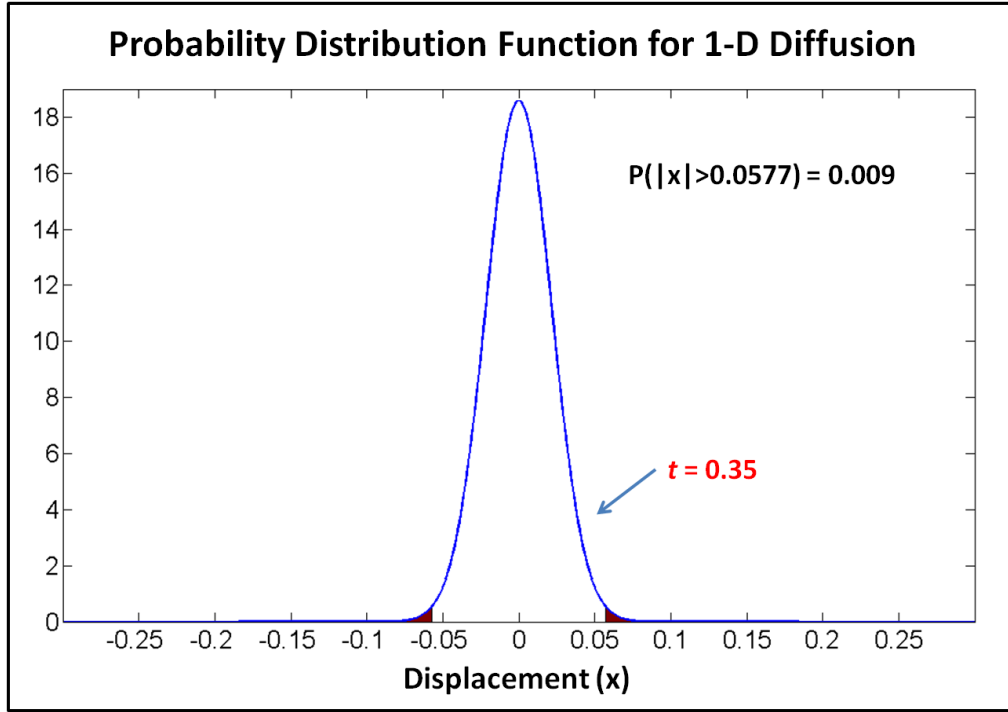


Figure 6.9 Probability distribution for the 1-dimensional diffusion of a 1 μ m microbead. The red indicates the calculated area under the curve, the result of Equation 6.7. The probability of the bead diffusing a distance greater than 57.7nm is 0.9%, which indicates that the transport that is being observed is not diffusive, but active transport.

The integration yields $P(|x| > 0.0577) = 0.009$ which shows that the bead movements are not diffusive but must be due to active transport. This confirms the internalized state of the microbeads and further confirms the selection of a selected bead as a probe for intracellular rheology.

6.5 *in vivo* Motor Stalling Results in Different Microbead Displacement Phenomena

To test forces being exerted by the molecular motors, forces are exerted on the microbeads with the 3-dimensional force microscope. The HeLa EGFP-654 cells are plated as described previously and dosed with the 1 μ m paramagnetic microbeads. The samples are placed in the environmental chamber previously set to 37.0°C. The sample

is visually scanned to find a suitable cell on which to collect data. As mentioned before, the cell will need to have at least 1 microbead in it that can be confirmed as undergoing active transport. Once this cell is identified, the motorized stage controls are used to lower the 3DFM pole tip down into position. The pole tip is generally lowered to a height of 10-50 μm above the cell culture. The typical sample would appear similarly to what is depicted Figure 6.10.

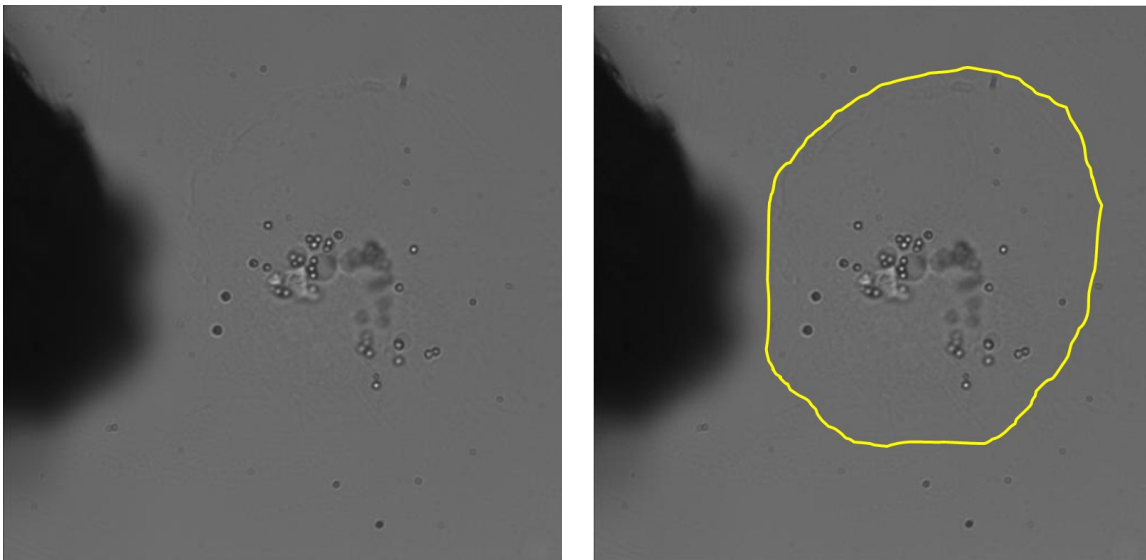


Figure 6.10 The image on the left shows a typical 3DFM experiment. On the left side of the image, the end of the magnetic pole tip is visible. The cell is shown roughly off center in the field of view. The outline of the cell is traced in yellow. Several microbeads can be observed in this cell undergoing active transport, making it suitable for experimentation.

With the pole tip in position forces are exerted on the microbeads. The force calibration of the pole tip is done prior to the experiment and is described in Chapter 8.

When attempting to stall motors *in vivo* with the 3DFM I attempted to apply forces in a pulsed periodic manner. There is no real way with which to predict the directionality of a bead that is undergoing active transport. The bead moves in a bi-

directional manner under the power of the respective molecular motors. Isolation of anterograde or retrograde transport can be achieved by selective knock down of kinesin or dynein activity during the experiment. (Loschi, Leishman et al. 2009) ATP concentrations can be altered to bias the transport of organelles in the anterograde or retrograde directions. (Nilsson, Steffen et al. 2001) Barring these treatments the transport occurs in a stochastic manner.

First attempts to stall the microbeads *in vivo* involved the application of pulsed forces in an attempt to halt the procession of the bead. The magnetic forces were pulsed at frequencies in the range of 0.2-0.5Hz. The intent was to apply a force at the exact right time when a bead is undergoing an excursion away from the pole tip. While it is possible to manually actuate the force, the speed at which a bead can change direction, combined with the duration of the excursion in one direction, make it virtually impossible to time the force application with the transport of the bead. Ideally, the tracking of the bead would occur in real time, and when the bead began travelling away from the pole tip, the computer would activate force at the appropriate time and level to stall the bead. Otherwise force must be applied with the hope of coinciding with one of these events.

Classically stalling the beads *in vivo* proved to be a challenging proposition. Ideally the bead would undergo an excursion with some velocity, a force is applied bringing the velocity to zero, and once the force is removed the bead continues along at its previous trajectory. Achieving this in reality turned out to be an extremely rare. There were actually a variety of different phenomena that I observed from attempts to stall a motor *in vivo* which I will describe.

6.5.1 Case 1: The Motor Stall

I have one instance of a classical stall. This is out of thousands of pulls on microbeads over the years. In this case the 3DFM was pulsed at a frequency of 0.2Hz. The level of the force application was in the 4-5 pN range, a force comparable to the stall force of a single dynein motor. The force was applied for a total of 12 times over 2 minutes. Data are shown in Figure 6.11.

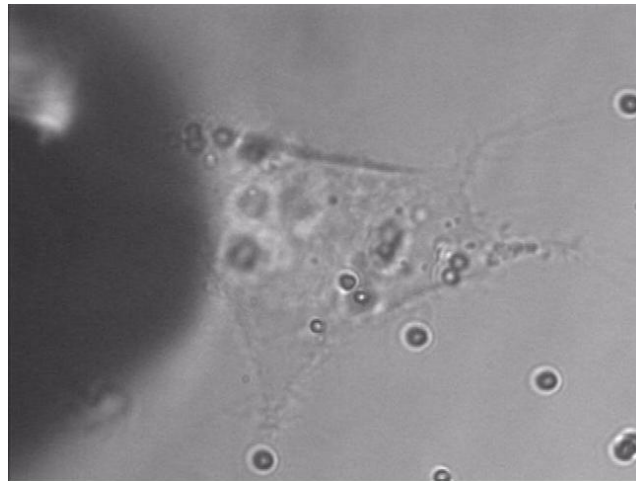
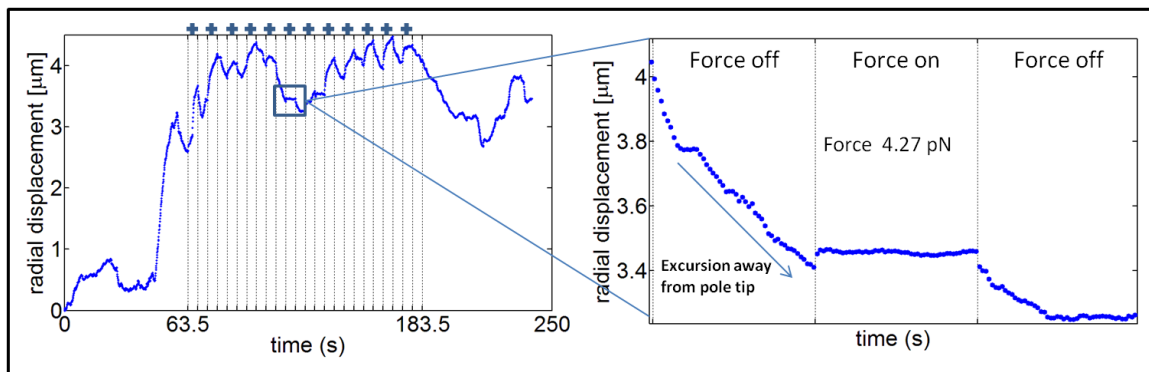


Figure 6.11 The above plot shows a displacement plot of a motor stalling experiment. The 3DFM was pulsed for 5 seconds on/off over 2 minutes. The force regime was in the 4-5pN range. The plus symbols indicate where the force is turned on. The top right shows a zoom-in of the plot showing where motor stalling is occurring. At the time that the force is turned on (4.27pN) the bead is taking an excursion away from the pole tip and its progress is halted. After the cessation of force the bead continues on its previous trajectory.

The plot in Figure 6.11 shows that prior to the sixth application of force the bead is undergoing an excursion away from the pole tip. When the force is turned on the progress is halted and the bead is stalled. The force applied is 4.27pN. The zoomed in portion of Figure 6.11 shows how the velocity becomes zero as the slope of the displacement becomes zero. After the force is turned off the bead continued along its previous trajectory. This represents the best example of in vivo stalling from the thousands of pulls that comprise this study. Roughly speaking it is less than $1/10^{\text{th}}$ of 1% of all of the pulls, indicating the difficulty of achieving this feat.

6.5.2 Case 2: The Viscoelastic Response

The majority of the cases of bead pulling result in the classical viscoelastic response. This is true for high force regimes (for these purposes we will call high force a force $> 50\text{pN}$) as well as low force regimes (1-30pN). The viscoelastic nature of the cytoplasm will be discussed more quantitatively in Chapter 7. Generally speaking a viscoelastic material is a material that possesses both viscous and elastic properties. When a bead is pulled through a viscoelastic material, after the force is removed, the bead regresses backward, as the material responds elastically. An example of a viscoelastic response is shown in Figure 6.12.

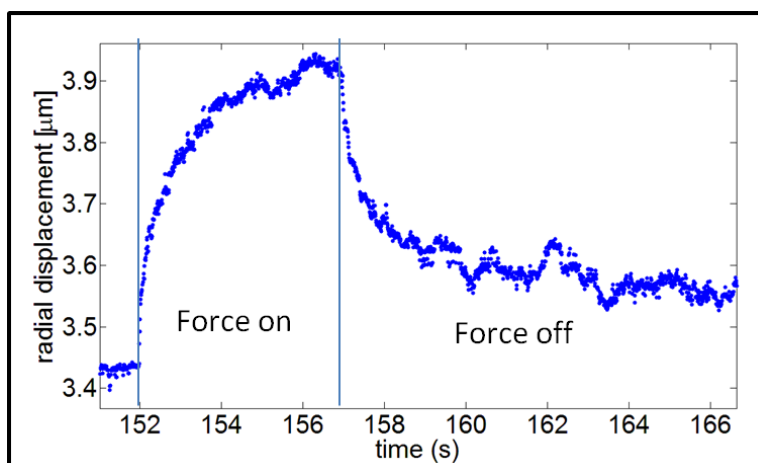


Figure 6.12 An example of a typical viscoelastic response. This effect is typical of the majority of the bead pulls, regardless of the force regime of the experiment. Viscoelastic properties of the cell will be discussed in more detail in Chapter 7.

In this example the force is on for 5 seconds and off for 10 seconds. Even when applying low forces to stall the motors a viscoelastic response is often the characteristic displacement. As with any experiment it is essential to match the timing of the video with the timing of the external force stimulus. At the current moment the 3DFM software does not in any way communicate or sync with the microscopy software. For these experiments I depend on timing the force start time with a stopwatch and then later determining the start time of the video with the tracked data. The appearance of at least one viscoelastic curve helps me to determine the exact frame at which the magnets turn on, so syncing the video data with the magnet data is not an issue. However, when probing low force regimes there may not be a well defined signal such as this to properly sync the two data sets. In this situation the data is unusable because even though I know the approximate time of the magnet start time, I can't determine it explicitly. The solution to this would be to get the programs to sync from a single clock and report the start times of both events in a metadata file. A second solution that I investigated was

connecting an LED that would turn on and add illumination to the field of view when the magnets are turned on or at least at the first magnet pulse. The LED would be connected to a port coming from the 3DFM amplifier so that illumination and magnetization would be simultaneous. In any event, probing low force regimes will require a magnet/microscopy synchronization to make data collection more efficient. Alternatively, at the end of any sequence of low force pulses, a single high force pulse could be applied to produce a large displacement to serve as a standard to isolate the start time for the low force pulses. This high force would risk detachment of the bead from the microtubule or disruption of the local environment surrounding the bead, which may or may not be desirable depending on the experiment.

6.5.3 Case 3: Direction Reversal

A third phenomenon that can be encountered with *in vivo* motor stalling will be the reversal of microbead direction during the period of applied force. When the force is turned on the bead begins to displace in a mostly viscoelastic manner. At some point in the force application, instead of continuing to displace in a viscoelastic manner, the bead begins to move in a direction opposite to which the force is applied. So if a bead is being pulled in an anterograde direction, the dynein motors “kick in” at some point and begin to walk the bead back in the retrograde direction. This phenomenon is depicted in Figure 6.13.

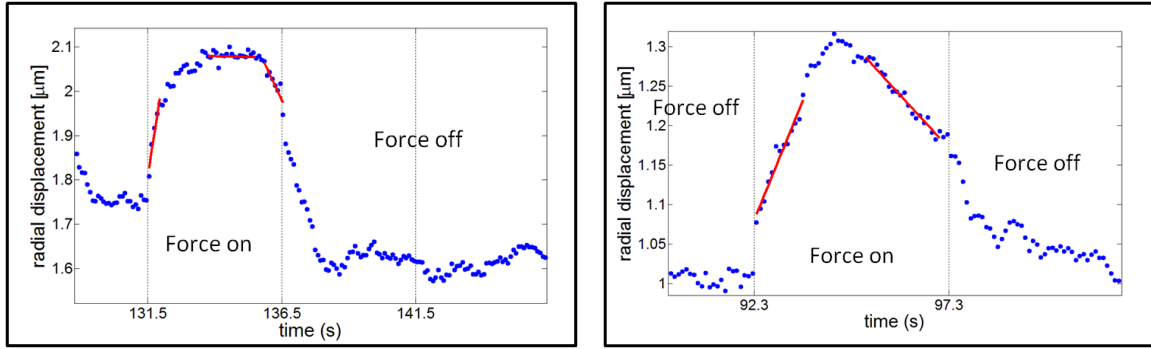


Figure 6.13 Two examples of the microbead reversing direction during the period of force application. The bead begins to displace in a mostly viscoelastic manner, but during the middle of the force application the dynein motors work to overcome the force of the magnet, and begin a retrograde excursion.

The applied force is overcome by the force of the dynein motors allowing it to move back towards the nucleus. In some sense this is a stall, in that the velocity of the bead becomes zero as it reverses direction. The force application in both cases is approximately 4.75 pN, again in the range of the stall force of a single dynein motor. This would point to more than one dynein motor being active at the time of the direction reversal. It is known that more than one motor can be acting on an organelle at any given time (Gagliano, Walb et al. 2009) and that the force applied acts in an additive, linear fashion. To stall motors in vivo forces will have to range from the force of a single motor to several, depending on the number of motors attached. The number of motors attached could be estimated based on the speed of the transport and the rheology of the cell. A computer program could take these features into account to modify applied forces in real time.

6.5.4 Case 4: Assisting Transport

When a force is applied during transport, in the direction of the transport, it may have the effect of assisting in the transport. When the force is removed, the bead will continue along the same trajectory, but at a reduced velocity. Normally when the force is

removed the bead's displacement will relax in a viscoelastic manner. But because the bead is still being transported after the force is removed, this relaxation is not seen. An example of this is seen in Figure 6.14.

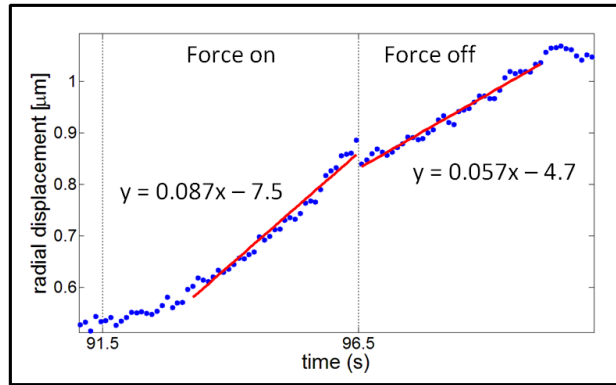


Figure 6.14 A case of the magnetic force assisting transport. During the interval of force application the bead begins to move towards the pole tip. Once the force is removed the bead continues along on its previous trajectory but at a slower speed. Least squares linear regression lines are fit to each portion, indicating a velocity of 87nm/s while the force is on, and a decrease to 57nm/s with the force on.

The force is turned on at $t = 91.5$ for 5 seconds. The applied force is quite low, only 1.65pN, on the order of the force of an individual kinesin motor. When the force is removed at time $t = 96.5$ there is a decrease in the velocity of the bead, although it travels along the same trajectory. Least squares regression lines are fit to each region separately to quantify the change. During the force application the bead moves at a rate of 87nm/s. Once the force is removed the velocity drops to 57nm/s, a 34% decrease. It seems that these low forces are able to impact the motor driven transport with low force application. Probing in these low force regimes could yield interesting transport data, but the synchronization of magnet and video issues will have to be overcome.

6.5.5 Case 5: Breaking Through

As previously stated, when applying an oscillating force to the bead, the predominate displacement will be viscoelastic in nature. Sometimes in the middle of the pull as the viscoelastic curve is flattening out, the bead will escape from its immediate surroundings and break through to continue its transport in the direction of the applied force. This case is shown in Figure 6.15.

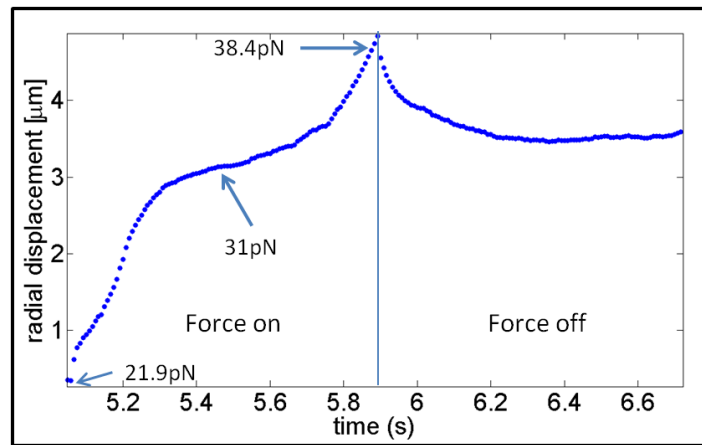


Figure 6.15 Example of a bead breaking through the local cytoskeletal entrapment to continue its movement in the direction of the force. At the point where 31pN is indicated, it would normally be expected that the bead displacement would flatten out. However because it breaks through there is an inflection point as the bead continues its path towards the pole tip.

The force at the beginning of the pull started out at 21.9pN and at the point where the bead breaks through the force has increased to 31pN. At the end of the force application the force has reached 38.4pN. In Figure 6.15, where 31pN is indicated, the expectation would be for the displacement curve to flatten out in a classical viscoelastic manner. Instead, the bead breaks free of its local environment to continue its trajectory towards the pole tip. The bead overcomes the elastic effects of the material, at least temporarily,

to achieve this. This phenomenon is not common, but can occur with sufficient force. It is a heterogeneous phenomenon, in the sense that it is dependent on where it is in the cell and can vary from cell to cell. It can happen also with greater or lesser degrees of force, and because it happens at one force does not mean it will happen again on a subsequent pull.

6.5.6 Case 6: Translation

The viscoelastic nature of the cytoplasm is well established. On occasion, microbeads can be translated through the cytoplasm with sufficient force. This is to say instead of the bead displacement flattening out viscoelastically, it travels in a somewhat linear trajectory, closer to what would be expected in a viscous medium. The bead may follow a trajectory that is dependent upon the obstructions from cytoskeleton and organelles, but is able to go around them as it moves towards the pole tip. An example is shown in Figure 6.16.

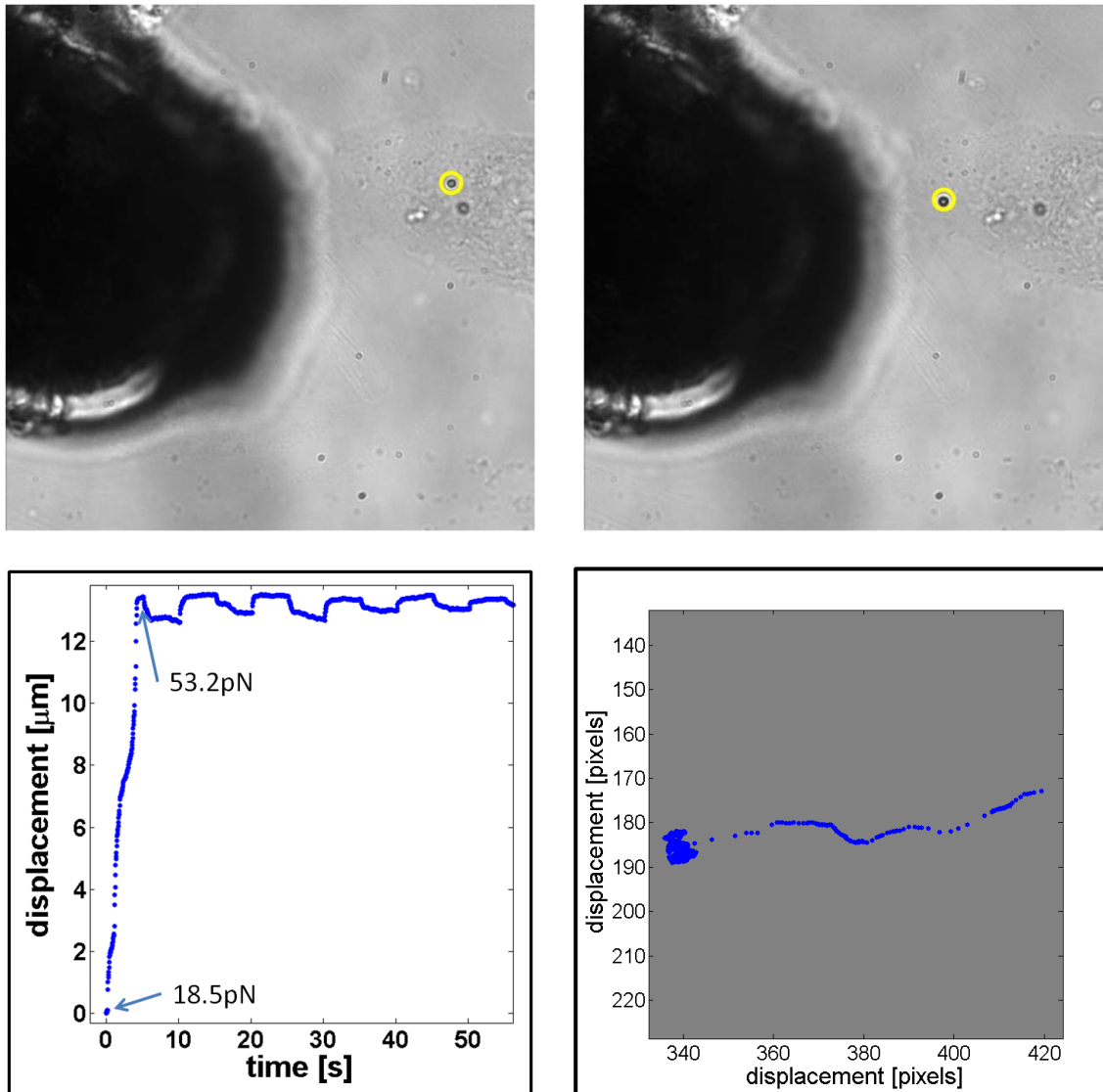


Figure 6.16 An example of a bead translating through the cytoplasm (bead is indicated by yellow circle). The trajectory is closer to what would be expected from a more viscous material. The bead moves around some of the intracellular features as it moves to the edge of the membrane/glass interface.

The bead is initially near the periphery of the nucleus before the force is applied. A force of 18.5 pN is applied and the bead translates towards the pole tip. The bead appears to circumnavigate some obstacles in the cell, as the trajectory bends on its path to the membrane/glass interface. As is shown in the bottom left displacement plot, the bead

translates nearly $13.5\mu\text{m}$ before stopping. The force of 18.5pN is not greater than a typical force used in these experiments. A force of this magnitude is not necessarily always going to provide sufficient impetus to translate a bead through any particular cell at any given time. Given the right positioning in the cell and a high enough force it is possible to translate a bead in a cell.

6.6 A Maximum of 6 Dynein Motors act on a Single Microbead

To effectively determine the stall force necessary to halt the progress of a microbead, it became clear that a pulsative application of force isn't the most efficient method of data collection. Instead I decided to apply a constant steady force to the bead and analyze the displacement of the bead with respect to force. These experiments were performed as previously described. The only difference is that the force was applied for a full 60 seconds. The force calibration is shown in Figure 6.17.

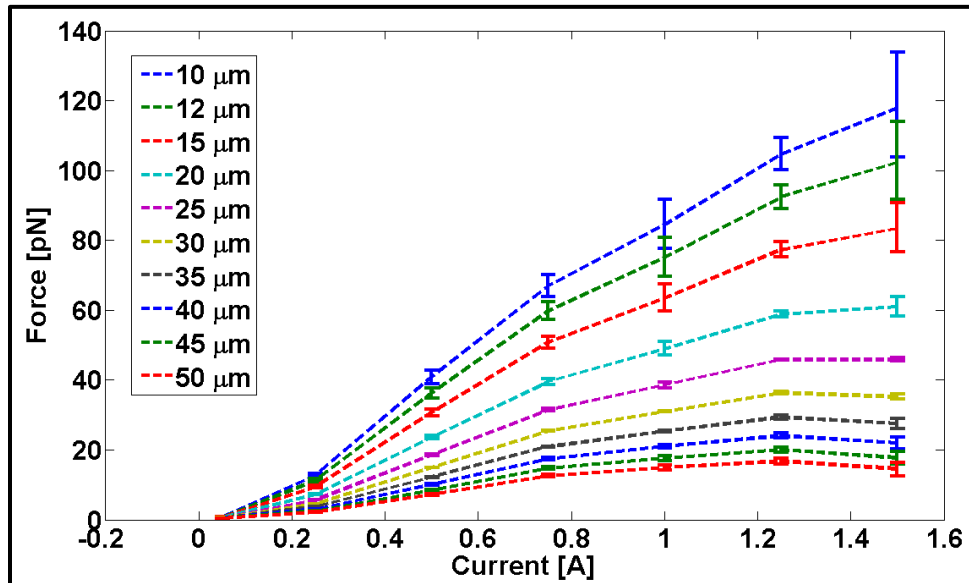


Figure 6.17 Force calibration for the long time scale force experiments. This was performed with a Netic pole tip $30\mu\text{m}$ above the sample.

The voltage signal for each experiment was ramped from 0.4V-3.0V. Data are collected on 21 microbeads. For each experiment video the positions of each microbead is recorded in an Excel spreadsheet. Based on the applied 3DFM current and distance of the bead from the pole tip, I determine a mean force on the bead. Using the same MATLAB program to analyze data from section 6.4, I determine the mean excursion sizes and velocities of the bead during the time of the applied force. The results are shown in Figure 6.18

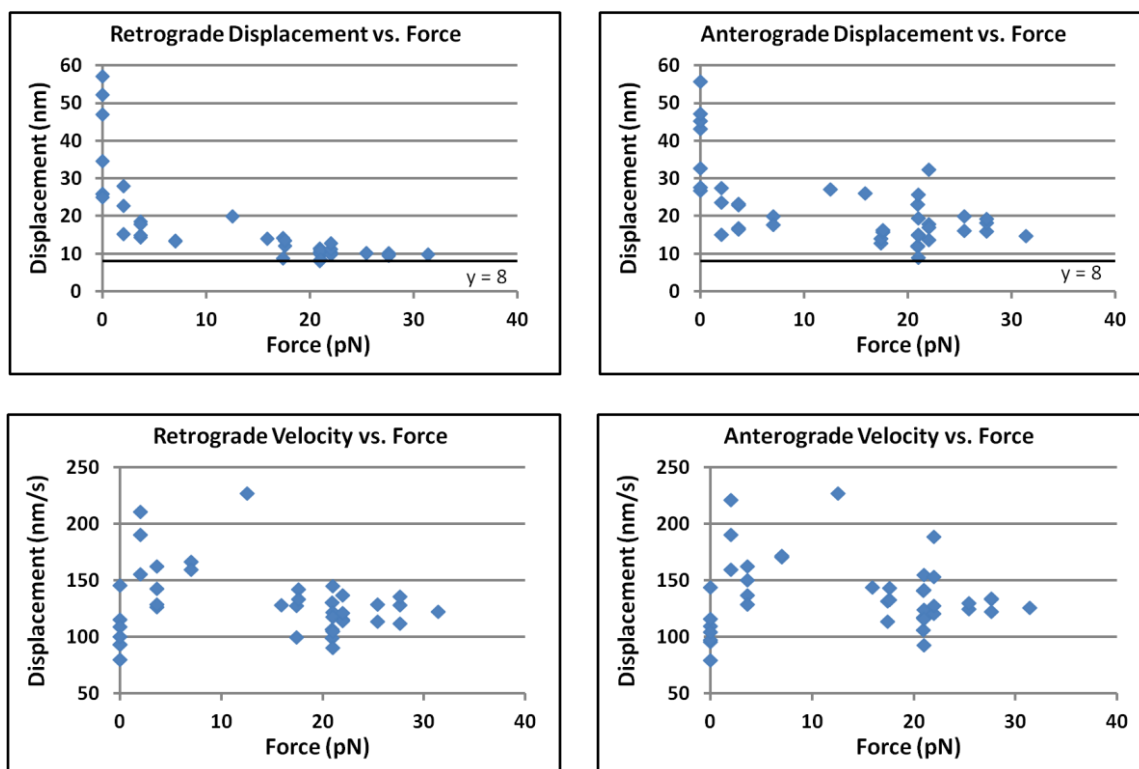


Figure 6.18 Plots of displacement vs. force and velocity vs. force for motor stalling experiments. Retrograde data is in the left column and anterograde data is in the right. The line $y = 8$ is plotted to show the location of the 8nm mean molecular motor step size.

Because of the geometry of the experiment, the anterograde direction is towards the pole tip and retrograde is away from the pole tip. Each data point on the Figure 6.18 represents a single microbead. The first result of note is that the retrograde displacement of the beads trends towards 8nm as force increases. Eight nanometers is the length of a single step-size, which means that these beads are able to overcome the force of the 3DFM enough to, on average, take a single step backwards. We fit an exponential curve to the retrograde displacement data to calculate an intercept with the $y = 8$ line. The exponential regression line is shown in Figure 6.19.

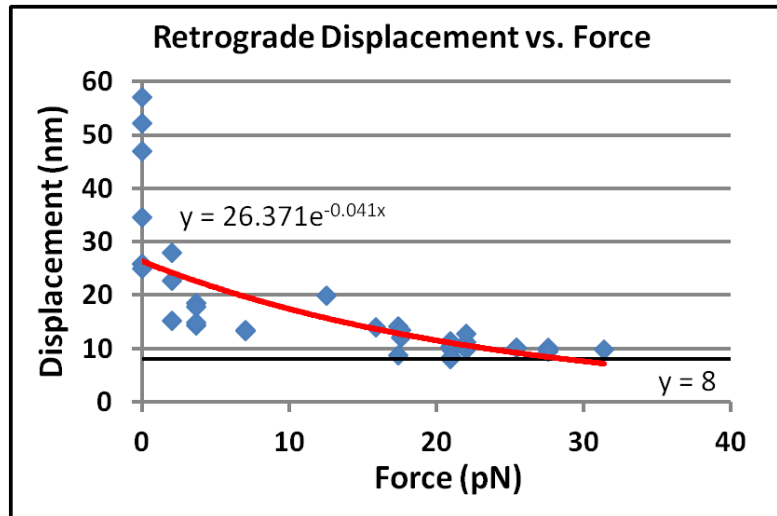


Figure 6.19 An exponential regression line is fit to the retrograde displacement vs. force data to determine stall force. Stall force is approximately 29pN.

Calculating the intercept of the regression curve with the line $y = 8$ yields a result of 29.09pN. The work of Holzwarth and others have introduced a shared load model of molecular motor transport. (Shtridelman, Holzwarth et al. 2009) Their data suggests that the stall force is linearly dependent upon the number of motors attached to a vesicle as shown in Equation 6.8:

$$F_s = N \cdot f_m \quad (6.6)$$

where F_s is the stall force of the vesicle, N is the number of motors, and f_m is the stall force of an individual molecular. The stall force of kinesin has been measured to be approximately 6pN with values reported within a few piconewtons of this value. (Howard 2001) Similarly, dynein stall forces have been reported between 2 and 8 pN. (Gennerich, Carter et al. 2007) The data in Figure 6.19 represents stalling force on dynein motors working against the 3DFM to transport the bead towards the nucleus. Taking a mean stall force for dynein to be 5pN this would result in approximately 6 dynein motors at most acting on a microbead when the highest forces are acting on it. I have not quantified the number of motors attached to the microbeads as a part of these studies. Fluorescence microscopy or SEM imaging of fixed cells could be used to determine the average number of motors attached, which would help to verify my conclusions. Electron micrographs of fixed cells have shown that 2-3 motors are attached to a vesicle. Given the relatively large size of the microbeads relative to the majority of vesicles, it is not unreasonable that there could be 6 motor proteins attached. It should be noted that a motor protein could be attached to a vesicle or microbead, but unless it is in contact with a microtubule, it will not be participating in the transport process.

The plot of retrograde velocity versus force shows that there is no impact to the microbeads velocity with respect to the applied force. The mean velocities at 0, 20, and 30pN are 129.4 ± 6.45 , 119.3 ± 3.9 , 124.8 ± 5.1 which are all within each other's standard error (velocities within ± 2.5 pN of 20 and 30pN are averaged together). So while the applied force has a definitive effect on retrograde displacement, it does not seem to have an effect on the velocity that the bead takes when it makes this excursion.

This should not be confused with the idea that a motor having a velocity of zero. These data say that when a bead does take an excursion under the influence of these forces, the velocity is not affected. This lends itself to a ratchet and gear type description of motor transport. If the microtubule is the ratchet and the motor is the gear, the gear is moving along the ratchet in 8nm steps. The stalling force holds the gear in place, until it is sufficiently motivated to take an excursion away from the applied force. In spite of the level of force applied to the gear, when it does take this excursion, it does so at some set velocity, that is not dependent on the applied force. This is comparable to a digital versus analog electrical signal. If the bead velocity behaved in an analog fashion, during the retrograde excursions, the velocity would decrease based on the amount of opposing force applied. However we see that when the excursions do occur, the velocity is not affected, making it a more digital, on or off feature.

6.7 Conclusion

I have presented a protocol to introduce 1 μ m particles into the intracellular environment. Although I have not used it with other cell types I am confident that it would have uses for other cell types and for other forms of force application, particularly AFM. Upon gaining entry to the cytoplasm, the 1 μ m bead is enveloped in a pinched off portion of the cell membrane, forming an early endosome. Molecular motors attach to this endosome and the bead begins to undergo active transport, similar to the bi-directional transport of an organelle. I have shown the temperature dependence of the microbead transport, with increases in mean velocity and excursions as high as 170% and 354% respectively. I have shown how the intracellular position of the bead can be shown

with stacks of fluorescently labeled cells reconstructed as 3-dimensional isosurfaces. The beads can be shown to be undergoing active transport based by comparing the mean displacements based on the probability distribution of a diffusing bead. The mean squared displacement of the beads also confirms that the beads are being actively transported. There are a variety of different responses that can be observed when attempting to stall an actively transported microbead *in vivo*, which have been detailed here. By ramping the forces exerted on a microbead, I have shown a decrease in retrograde displacement with respect to force. By fitting an exponential curve to these data I have determined that forces in excess of 29.09pN are sufficient to arrest the retrograde transport of the bead. This equates to a minimum of 6 dynein motors being attached to the microbead at one time, based on the shared load model of motor transport. I have also shown that when a bead does undertake retrograde excursions under the influence of an external opposing force, the velocity that the bead travels during that excursion is not affected by that force.

Chapter 7

Probing of Intracellular Mechanics with 1 μ m Paramagnetic Microspheres

7.1 Overview

This chapter will outline some of the rheological observations I have made during motor stalling experiments. Though not a focus of this dissertation, there are interesting findings that serve as preliminary results for future study.

Materials can be classified based upon physical characteristics that they possess. For instance, a diamond is clearly understood to be a solid. It does not exhibit any of the properties of a gas or liquid such as the ability to expand or flow. Holding a diamond in your hand, you can exert a compressive force upon it and it will not deform in any way. With the use of machinery compressive, shear, or tensional forces can be exerted upon it and still the diamond will not deform. The tight, regular conformation of carbon atoms makes this material the hardest substance known on the earth. The vast majority of materials in everyday life will not exhibit this level of material integrity and will in fact

show a variety of effects when acted upon by outside forces. A rubber band will deform when it is stretched out, and when the force is removed from the rubber band it returns to its original conformation. As long as the force applied is below the point of failure the material should return to its native state. This type of phenomenon is considered elastic behavior. Some materials can be deformed, but do not recover from the deformation once the force is removed. When a boat is pushed away from a dock, the boat does not return to the dock once the force has been removed, it will continue to float in the water some distance away from the dock. The water is designated as a viscous material. Elasticity and viscosity are terms that express the behavior of a material when a force is acted upon it. However many materials, especially in biological systems, do not fall cleanly into either of these categories. These materials can be classified as viscoelastic materials, possessing properties of both viscous and elastic materials. Viscoelastic materials can exhibit varying levels of viscosity and elasticity which effect how it responds under stress, and classifying them is done by applying forces on them and measuring their response. This is the work of the field of rheology, and as it applies to biology, can provide explanations for phenomena, as mechanical properties become better characterized. As biological rheology is further studied, it will advance the understanding of how the systems of the body work, the mechanisms of health and pathology, and elucidate novel means by which diseases can be treated and potentially cured.

7.2 Mechanical Models

As previously stated, viscoelastic materials exhibit both viscous and elastic behavior. To model behavior mathematically, models are comprised of springs and

dashpots connected in series and parallel. Springs represent the elastic responses of the materials and dashpots represent the viscous components. Arranged in different configurations, these models represent different types of viscoelastic response to force.

7.2.1 Springs

Elastic behavior is represented as a Hookian spring, in which the force is linearly dependent to the displacement of the spring, and is represented mathematically in Hooke's law expressed in Equation 7.1:

$$f = -kx \quad (7.1)$$

where f is force on the spring, k is Hooke's constant, and x the displacement of the spring.

In model diagrams springs are represented as shown in Figure 7.1.



Figure 7.1 Schematic diagram of a spring. G is the elastic modulus representing the stretchiness of the spring.

This relationship can be similarly expressed in terms of stress and strain, as shown in equation 7.2.

$$\sigma = G\varepsilon \quad (7.2)$$

Stress (σ) is analogous to pressure, the amount of force exerted over a given cross-sectional area. Strain (ε) is the ratio of the extension over the length and G is the elastic modulus.

7.2.2 Dashpots

Dashpots or Newtonian dashpots represent the viscous component of a viscoelastic material. It is an idealized element that is fixed at one end and responds to a force with by lengthening at a constant velocity. Dashpots represent the characteristics of the material that behave like a Newtonian fluid.

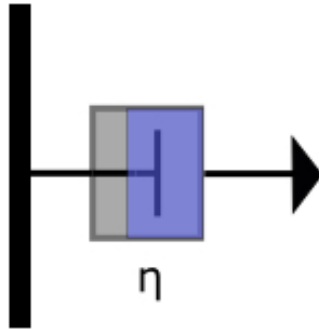


Figure 7.2 Schematic diagram of a dashpot. η is the viscosity of the dashpot which represents the fluid (viscous) component of the material

The extension of the dashpot increases linearly with time as force is applied. The stress (σ) is proportional to the strain rate ($\dot{\varepsilon}$) as shown in equation 7.3.

$$\sigma = \eta\dot{\varepsilon} \quad (7.3)$$

where η represents the viscosity of the fluid. The dashpot and spring can be connected in series and parallel to form systems that represent the mechanical properties of different viscoelastic materials. The Kelvin-Voight model will be described in the following section.

7.2.3 Kelvin-Voight Model

The Kelvin-Voight Model is modeled as a spring and dashpot connected in parallel. It is represented schematically in Figure 7.3.

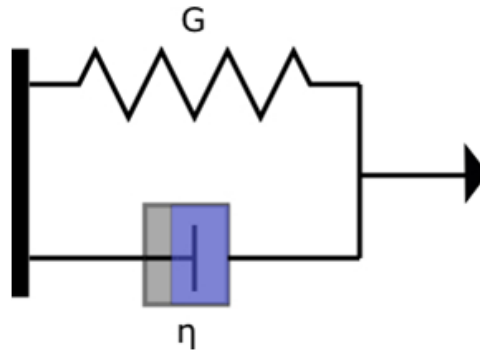


Figure 7.3 Schematic drawing the Kelvin-Voight model, of a spring a dashpot connected in parallel.

This system is modeled mathematically in equation 7.4.

$$\sigma = G\epsilon + \eta \frac{d\epsilon}{dt} \quad (7.4)$$

7.3 Intracellular Rheology Measurements

Once intracellular beads have been identified, forces can be brought to bear to manipulate the bead *in vivo*. I use the 3DFM to apply forces to the microbeads as described in section 6.5. Instead of attempting to stall the motors with the low force

regimes, I apply forces in the higher end of the spectrum, in the 20-150pN range or higher. The Kelvin-Voight model is used to model the viscoelastic response of microbeads pulled with the 3DFM. To calculate the shear modulus we first calculate the compliance by equation 7.5.

$$J = \frac{1}{G} = \frac{6\pi r x(t)}{F} \quad (7.5)$$

The Kelvin-Voight model is then fit via a least squares regression to the plot of compliance vs. time, to determine the viscosity and elastic modulus.

7.4 Cytoplasm Rheology

When a microbead is in between the nucleus and the membrane edge, the cell cytoplasm can be probed for rheology experiments. If the bead is close to the membrane edge, the bead will be probing the cortical actin of the inner membrane. If it is near the nucleus, depending on the position of the bead with respect to the direction of force, the nucleus mechanics will be probed. An example of proper bead positioning to probe the cytoplasm is shown in Figure 7.4.

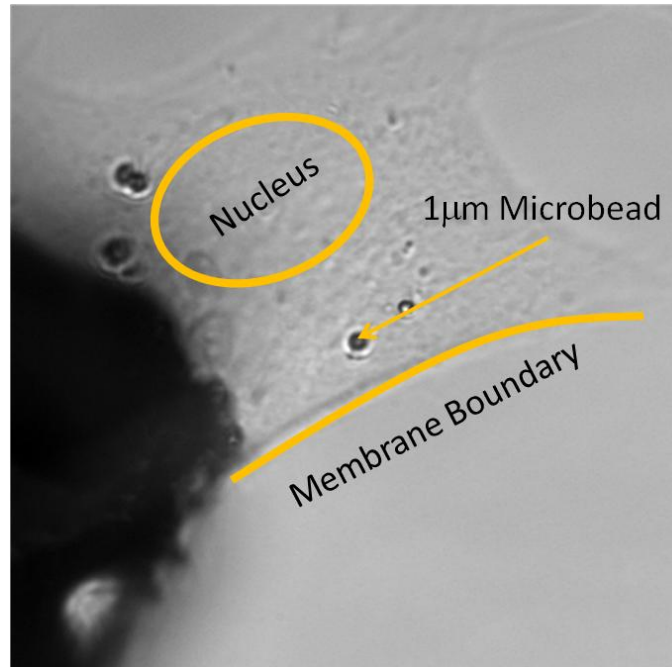


Figure 7.4 To measure cytoplasm rheology, the probe must be between the nucleus and the membrane boundary.

Data was collected from 14 beads in a total of 6 cells. The beads were pulled 3 consecutive times for a 10 second on/off interval. The measured elastic moduli and viscosity are shown in Figure 7.5.

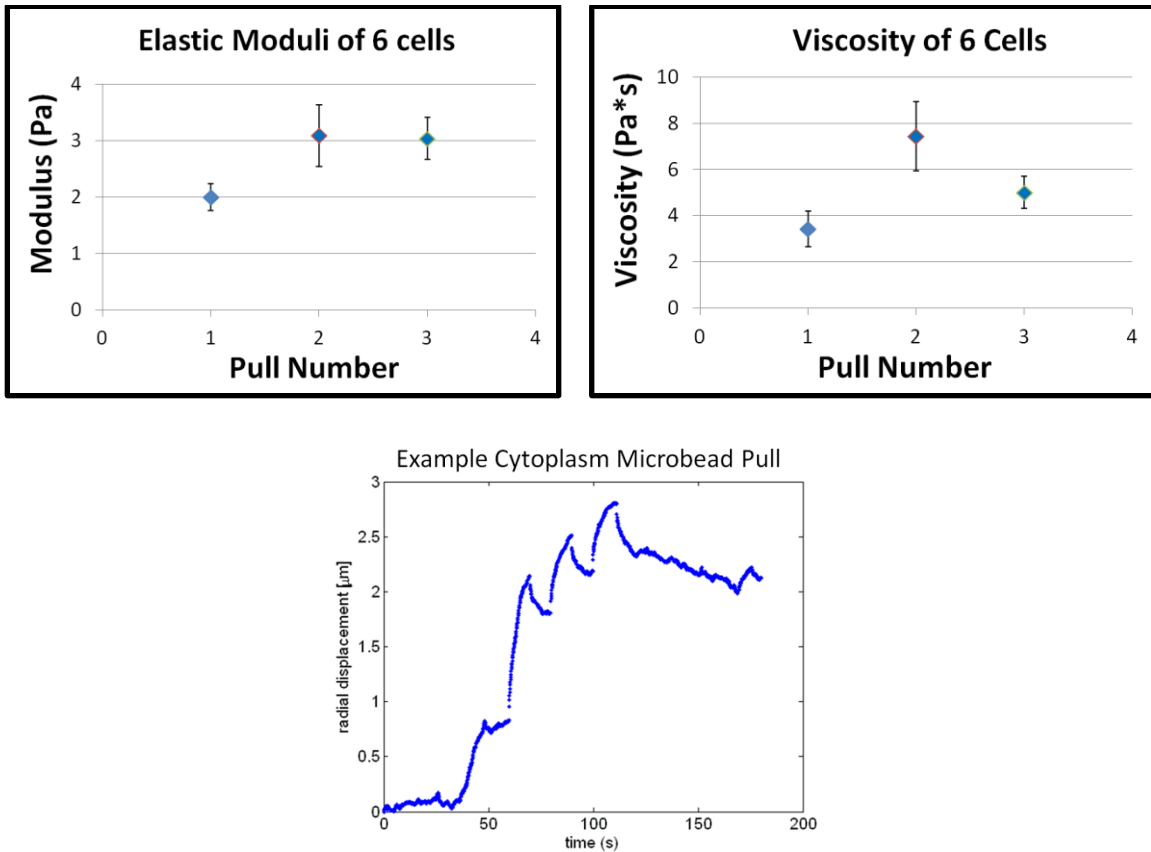


Figure 7.5 (Top Left and Right) The elastic moduli and viscosity of 6 cells are plotted for each of the 3 consecutive pulls of ten seconds each (10 seconds on/off). There is a slight increase in elastic modulus from pull 1 to pull 2, but not from pull 2 to pull 3. Viscosity increases on pull 2 but decreases on pull 3. (Bottom) A typical bead pulling radial displacement track. The magnets are programmed for 3 consecutive pulls after 60 seconds.

The elastic moduli increases by 55% after the first pull but does not change for the second and third pull. This may indicate some strain stiffening, but only after the first pull. Pulling on 3 beads within another single cell yields additional insight. In this experiment the respective beads are pulled a total of 12 times, as shown in Figure 7.6.

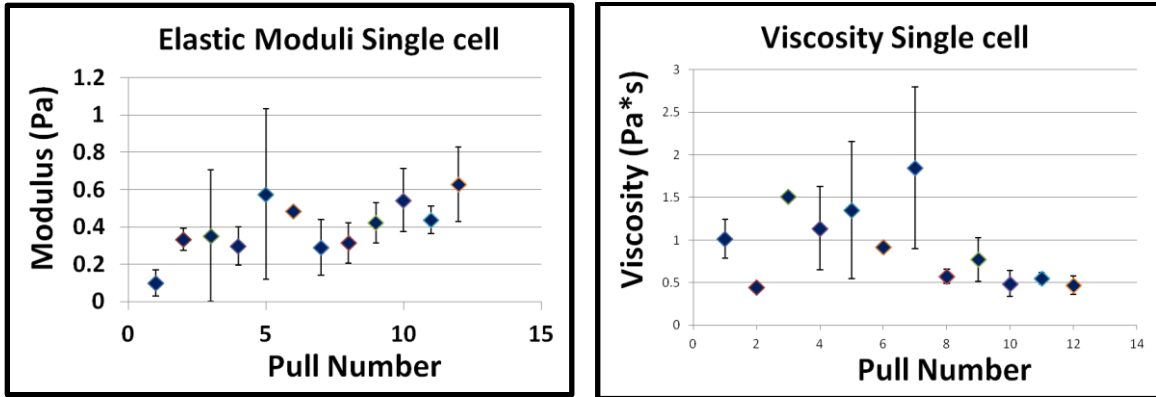


Figure 7.6 Collected moduli and viscosity of 1 cell measured by 3 microbeads. Generally speaking there is an upward trend in the value of the elastic moduli, showing some degree of strain stiffening. The viscosity doesn't appear to have a similarly distinctive trend.

Over the course of 12 pulls the elastic modulus increases by 523% going from 0.1Pa to 0.63Pa. These data appear to indicate that the cytoplasm of the cell strain stiffens with applied external force.

7.5 Cytoskeletal Disruption

In an instance when a bead is translated through the cytoskeleton, it distorts the cytoskeleton along the path that it travels. This can be seen when on a second microbead is pulled along the same trajectory as the first bead. When the second bead travels through the disrupted cytoskeleton, the elastic modulus as measured by the second bead is significantly less than what is measured from the first bead, along the same trajectory.

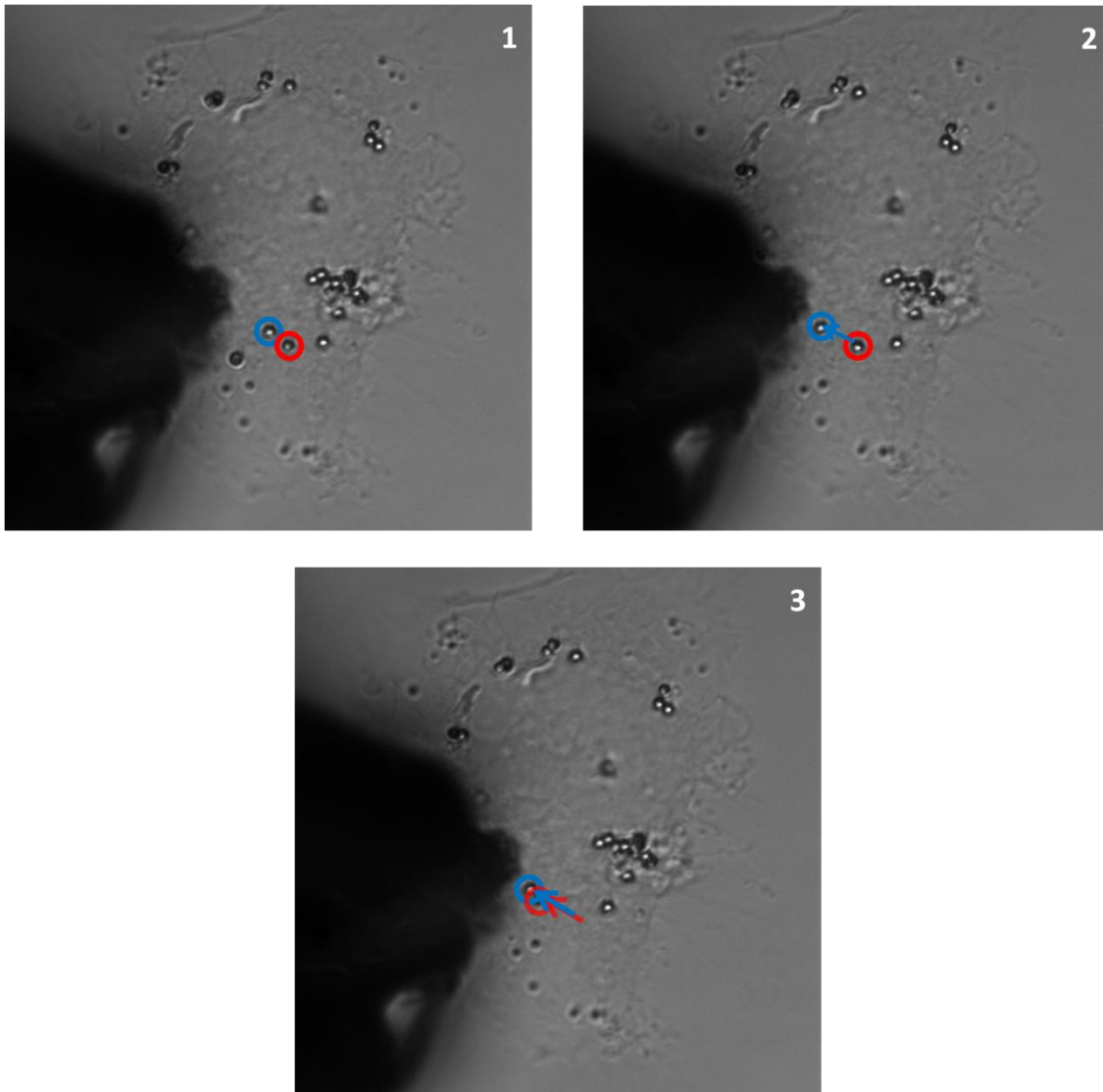


Figure 7.7 Example of microbead manipulation disrupting the cytoskeleton. Image 1 shows two beads prior to force application. Image 2 shows the first force application, and the blue bead which is closer to the pole tip translates towards it. In image 3 the second (red) bead moves towards the pole tip, eventually following the same path as the first bead. The disruption of the cytoskeleton can be seen by the severe reduction in elastic modulus as measured by the second bead. Data are shown in Figure 7.8.

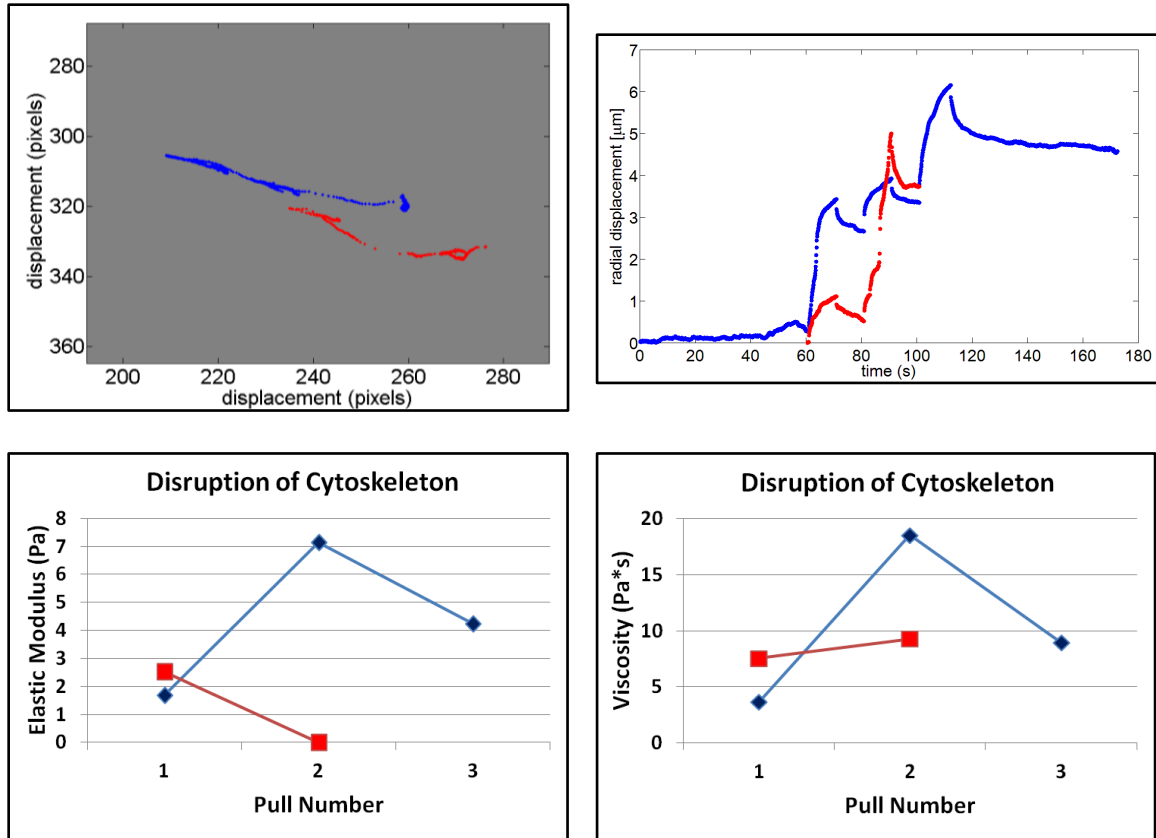


Figure 7.8 Top Left: X-Y plot of two beads in proximity to one another. Force is applied with 3 separate pulls of 10 seconds on and then off. After the first bead (blue) pulls in front of the second bead (red), the bead follows the trajectory of the first bead on the second pull. Top Right: radial plot of both beads. Bottom Left: The elastic modulus measured by the second bead on the second pull decreases 6 orders of magnitude to nearly zero, indicating that the elastic component of the material is removed. Bottom Right: The viscosities are still within a similar range, as it should be, since the viscous component of the material is still present.

In Figure 7.7 the bead marked with the blue circle measures an elastic modulus of 1.68 Pa. It disrupts the local cytoskeletal environment to such an extent that when the red bead follows along its path, it experiences an elastic modulus that has decreased to .0000196, a decrease of 6 orders of magnitude. The red bead is basically travelling through a cytoskeletal tunnel of cytosol, vacant of structural elements. This is seen in the measurements of viscosity, which does not experience a similar drop. On the first pull,

the first (blue) bead measures a viscosity of 3.6 Pa·s, but on the second pull, the second bead (red) measures a viscosity of 7.54 along the same path as the first bead. There is no decrease in viscosity, which tells us the viscous component of the cell remains in that region.

7.6 Probing of the Cortical Actin of the Inner Cell Membrane

With a bead in proximity to the membrane it is possible to probe the mechanics of the cortical actin. If the bead is not near the membrane, it is sometimes possible to translate the bead to the edge of the cell with sufficient applied force. Such is the case in Figure 7.9. The bead is near the nucleus before the force is applied, and with an applied force of 18.5pN the bead is transported to the edge of the cell. Once at the edge of the cell the bead is pulled on an additional 13 times. The resulting elastic moduli and viscosity are shown in Figure 7.9.

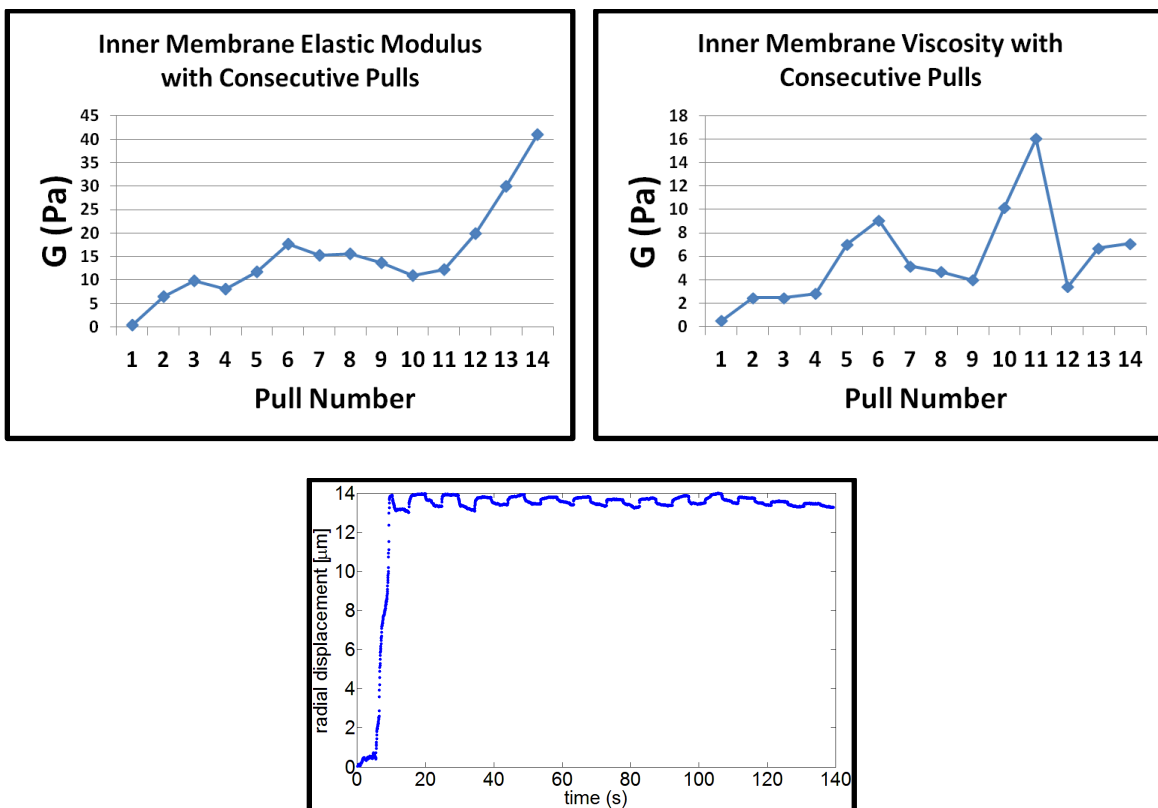
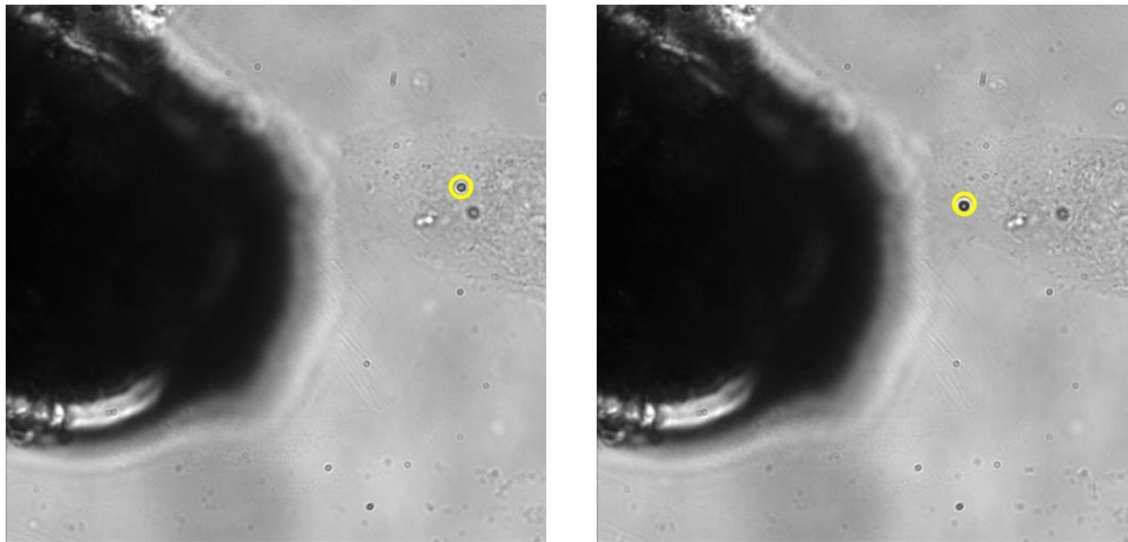


Figure 7.9 (Top Row) A bead is translated through the cytoplasm to the edge of the cell membrane. The first pull translates the bead 13 microns. Subsequent pulls probe the cortical actin. (Middle Row) Membrane modulus increases by a factor of 530%, indicating strain stiffening. (Bottom Left) Displacement plot of bead track.

The first pull measures a modulus and viscosity of 0.4Pa and 0.5Pa·s, within the range of the results found in 7.4. The first pull at the cell boundary yields a modulus of 6.5Pa.

The final pull yields a modulus of 41Pa, an increase of 530%. It appears that both the cytoplasm and cortical actin strain stiffen, but the majority of strain stiffening is due to the cortical actin.

7.7 Conclusion

This chapter describes some of the rheological phenomena that have been observed in the course of attempted *in vivo* motor stalling experiments. Cell cytoplasm and cortical actin appear to strain stiffen, although to a greater extent in the cortical actin. A microbead appears to disrupt the local cytoskeleton, as indicated by the sharp decreases in elasticity in the region of the bead translation. The introduction of microbeads to the interior of the cell provides a probe that is nicely uniform and sufficiently paramagnetic so as to permit relatively high forces for measurements. These data provide groundwork for further quantification of intracellular rheology and the responses of cells to externally applied forces.

Chapter 8

Appendix

8.1 Appendix One: Instrumentation

This section will describe the instruments that have been used in the experiments described in this dissertation. These include optical microscopes, 3-dimensional force microscopes (3DFM), and an environmental microscope with a motorized 3DFM stage. I designed the motorized stage and will describe its design and assembly.

8.1.1 3-Dimensional Force Microscope

The basic design of the 3-Dimensional Force Microscope consists of wire coils wrapped around an iron core. There are 6 cores oriented in a hexagonal orientation in this current design of the instrument. The 6 cores can be individually and independently activated by sending desired signals through the amplifier, to which it is connected. One core activates to magnetize the pole tip, and the opposite 3 cores activate the flat. The pole and flat are activated at opposite polarities in terms of the voltages. For example, if a pole is activated at 1V, then the 3 cores on the flat would each be activated at -0.33V.

Alternatively six pole-flats could be positioned on each core providing force application in 3 dimensions. The pole-flat geometry produces force in one direction, which for the purposes of many cell mechanics studies is sufficient. For intracellular active transport experiments, a multidirectional array may be preferable, due to the bi-directional transport involved. An example 3DFM lid is shown in Figure 8.1.

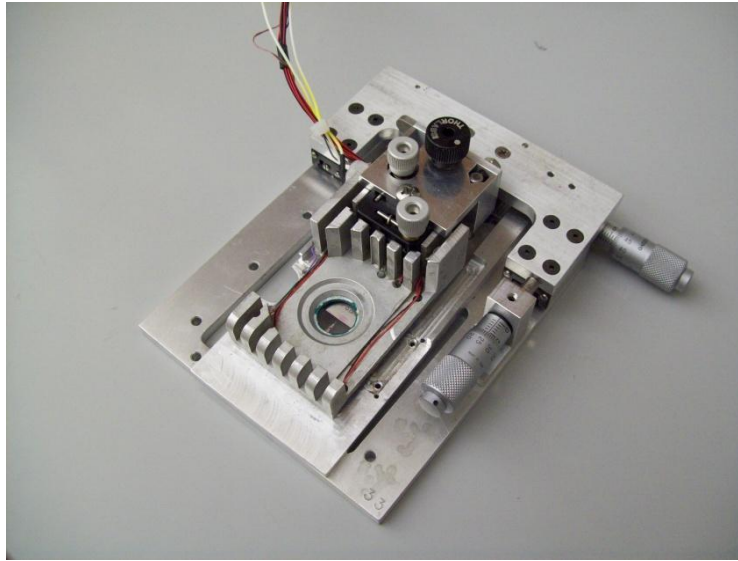


Figure 8.1 Image of a 3DFM lid placed on a stage. The sample will be placed between the lid and the stage. The entire unit is then screwed into the microscope stage.

To activate the pole tips, MATLAB is used to communicate with a DAQ board that has been installed in the PC. This board sends an appropriate signal to an amplifier based on the voltage, duration, and frequency programmed into MATLAB. The amplifier then produces the desired voltage in the designated cores to produce the magnetization of the pole and flat.

The pole and flat materials are composed of soft thin magnetic foils produced by Magnetic Shield Corporation. The foils are characterized as Netic and Co-netic AA

based on their composition. Each material has distinct magnetic properties that make them useful for distinct experiments. (Fisher, Vicci et al. 2006) The Netic material has a higher magnetic saturation point than the Co-Netic material, which means that the Netic material is capable of higher forces. The Co-Netic material has a lower saturation so a pole tip made from it will have a lower overall maximum force. Because of its lower saturation the Co-Netic material will also have a lower remnant magnetization than the Netic material. The Co-Netic also has a higher permeability meaning that it will achieve its maximum force more quickly than the Netic. The pole tips are typically 15-20 μ m in diameter. Further sharpening by hand will decrease this radius which results in higher forces. Magnetic data on the two materials is shown in Table 8.1.

Material	Saturation Induction (Tesla)	Permeability	Coercivity (Oersteds)
Netic	2.1	200	1.0
Co-Netic AA	0.8	30,000	0.015

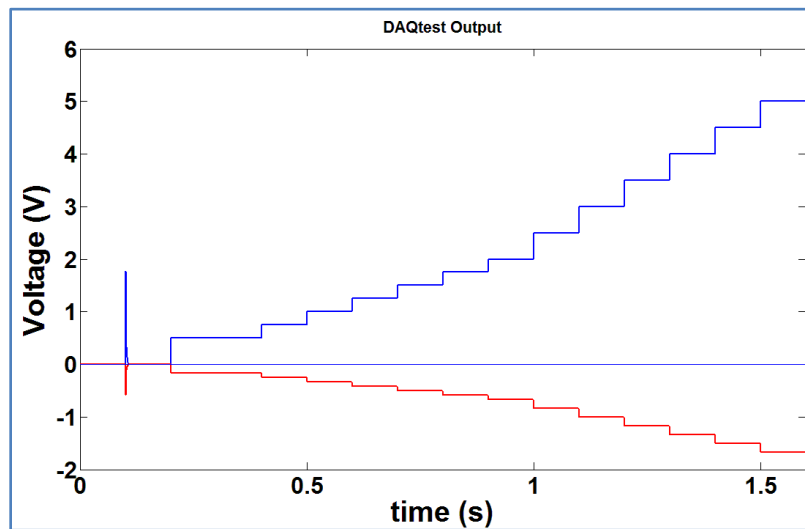
Table 8.1. Magnetic Materials Used in 3DFM Pole/Flat

To calibrate the 3DFM, paramagnetic beads are placed in a solution of a Newtonian fluid. The calibration is based on Stokes' law of force applied to a bead being pulled through a fluid of known viscosity. This law is expressed mathematically in equation 8.1:

$$F_d = 6\pi r\eta v \quad (8.1)$$

where F_d is the drag force, r is the radius of the bead, η is the viscosity of the Newtonian fluid, and v is the velocity of the bead. The 1 μ m beads to be used in the experiment are added to a solution of 2.5 μ M sucrose in water. The viscosity of the sucrose solution is

characterized via a cone and plate rheometer and found to be 0.142 Pa·s. The beads are added so as to comprise <5% of the total volume. A 24X50mm 1½ glass coverslip is placed on the microscope stage and 30 µl of the bead/sucrose solution is added to the coverslip. The 3DFM lid is placed over the sample and the pole tip is brought into focus on the microscope. For calibration purposes, the z-position of the in-focus pole tip is considered the “origin” or 0µm position, and z-positions below that are referred to as “X”µm below the sample. For instance, if one focuses at the pole tip and then adjusts the microscope focus 20µm below that point, then that point would be called “20µm below the pole tip”. While calibration of the tip is being done, it is done at distances below the pole tip at which experiments will be performed. Once the microscope is focused at the desired z-height, the 3DFM is sent a ramp of voltages ranging from 0V to 5V. The signal is shown in the Figure 8.2.



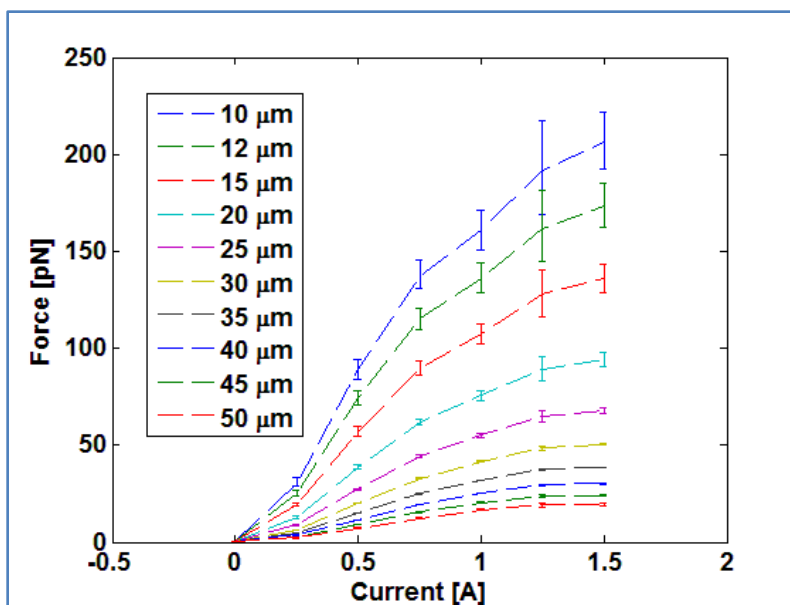


Figure 8.2 Top shows the voltage signal sent to the 3DFM for a typical calibration. The blue line shows the voltage sent to the pole and red line shows the signal sent to the flat. Below is a saturation plot of force vs. current for a netic pole tip 15mm below the sample.

The blue line indicates the voltage sent to the pole tip and the red line indicates the voltage sent to each of the 3 cores of the flat. Beads in the sample will accelerate towards the pole tip is activated. Video is captured at 120 or 60 frames per second. The beads are spot tracked and edited with a MATLAB program called evt_gui. This program enables tracks to be edited to remove portions of the bead motion prior to and after the tip magnetization.

8.1.2 Nikon Eclipse TE 2000-E

A Nikon Eclipse TE 2000-E inverted optical microscope (Tokyo, Japan) was used for many of the motor transport, rheology, and transfection experiments. These were used with a 100X 1.3NA CFI Plan Fluor oil objective and a 40X 0.6NA Plan Fluor ELWD objective. The microscope is also equipped with a 1.5X multiplier. Fluorescent

images were taken using a Photometrics Cascade II 512 electron multiplying CCD digital camera. (Roper Scientific, Inc., Tuscon, AZ) This camera was also used in motor stalling and rheology experiments. The camera and filters were controlled using IPLab 4.0. (BD Biosciences Bioimaging, Rockville, MD) For motor stalling and rheology experiments a Jai-Pulnix model PTM-6710CL was used. This camera has a maximum 120 frames per second at the full 648x484 pixel resolution. This camera was used only for bright field applications.

8.1.3 Environmental Microscope

The environmental microscope is an Olympus IX81 motorized inverted microscope. It has been set up to provide transmitted bright field as well as epifluorescence illumination. Imaging is achieved using a QImaging Rolera EM-C² emccd 14-bit digital camera. The microscope, filters, shutters, and camera are all controlled via Metamorph from Molecular Devices.

Environmental control is achieved using an Air Therm ATX-H Heater Controller. This environmental chamber provides us with the ability to maintain samples at a desired temperature for extended periods of time during an experiment. It is also capable of pH control via introduction of CO₂ as well as relative humidity control.

8.1.4 Motorized 3DFM Stage

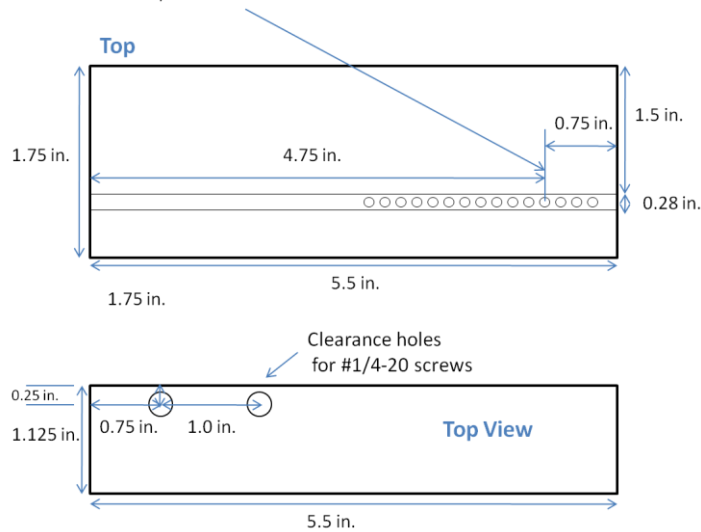
I designed a motorized 3DFM stage to be used in the Olympus IX81 environmental scope. The design for the motorized stage is centered on a ½ inch travel translation stage from Thorlabs (MT3). The z-axis micrometer is removed and two side-

mounted actuator kits are attached to both sides of the translation stage. To provide the motorized z-translation, I chose the Thorlabs motorized actuator (Z812B). This device is a ½ inch motorized micrometer stepper motor with a 26nm calculated resolution. The motor and the previously removed micrometer are attached to the translation stage via the actuator kits, pointed in opposite directions. They are attached in such a way as to produce movement in the + and – directions along the z-axis. When the motor is actuated in the –z direction the translation stage moves in the –z direction. The motor is controlled with a Thorlabs T-Cube DC Servo Controller (TDC001).

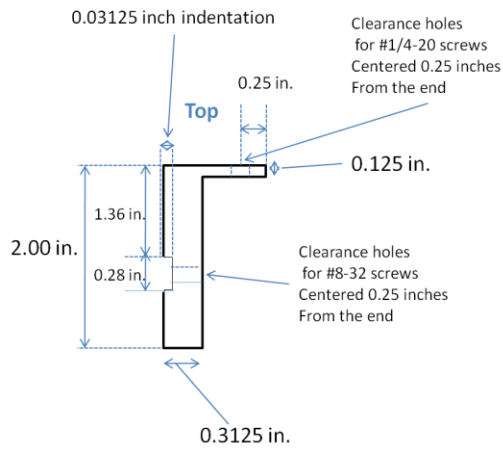
To attach the 3DFM lid to the XYZ stage an adapter had to be designed to accommodate the new way it was to be connected to the microscope. I designed a new adapter that would connect to the XYZ stage and extend the 3DFM to the microscope objective. A component of the 3DFM is a Thorlabs compact kinematic mirror mount. The rear of this component has a mounting hole for a #8-32 screw. The adapter was designed with slot wide enough to accommodate this component and a clearance holes for #8-32 screws. The 3DFM is screwed into adapter and the size of the slot is designed so as to not allow the kinematic mount to move once in place. The adapter is shown in Figure 8.3.

Top and Front View of Adapter

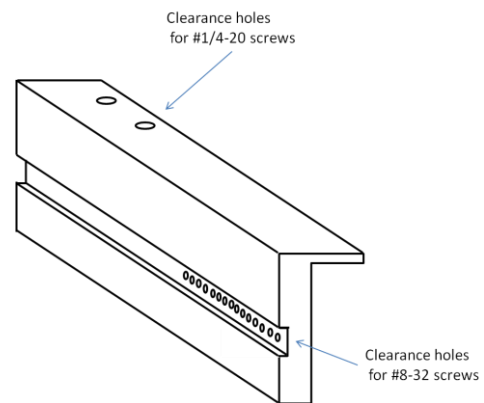
Clearance holes for #8-32 screws
 "Main" hole (4th from right) is 0.75 inch from the end.
 Other holes are spaced $\frac{1}{2}$ inch from each other



Side View of Adapter



Isometric View of Adapter



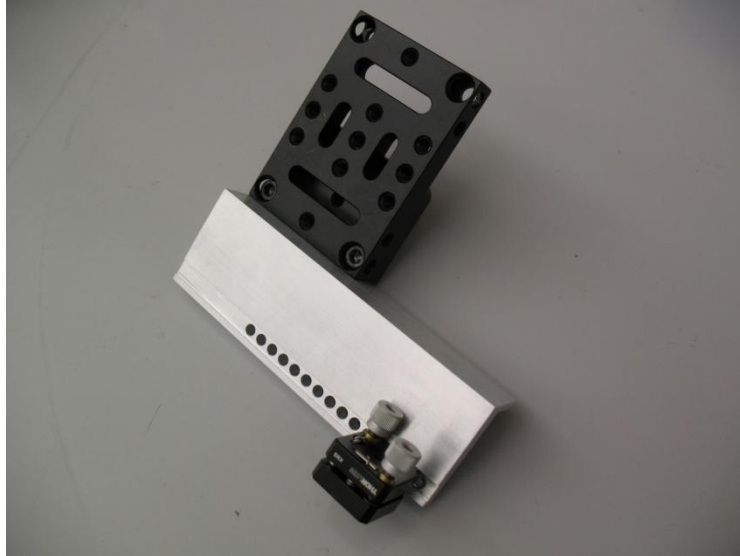


Figure 8.3 Schematic drawings of the 3DFM lid adapter. The bottom image is the adapter connected to a Thorlabs construction plate which attaches to an XYZ stage. The 3DFM connects through one of the holes, as shown with the mirror mount at the bottom of the photo.

In order to incorporate the 3DFM in the environmental chamber, I designed an adapter to affix to the microscope stage that would serve as a platform to mount the device. To do this I designed a 1.0X0.49X8.0 inch construction rail, with clearance holes for 2 M4 screws. The adapter was designed with mounting holes for #1/4-20 screws. A 2.5X3.5 in. construction plate is screwed into the adapter via 2 #1/4-20 screws.

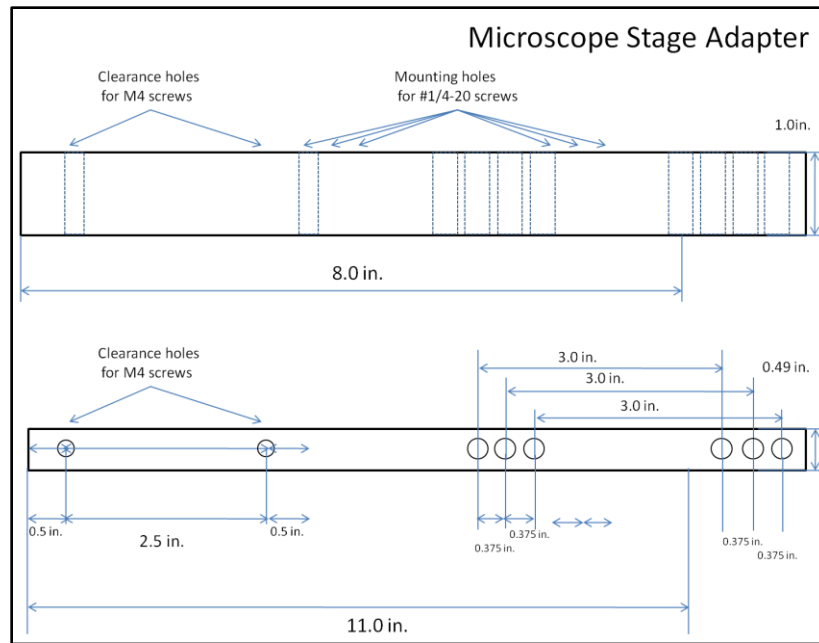


Figure 8.4 Stage adapter for the Olympus IX81 environmental microscope. This is screwed into the microscope stage and the XYZ stage is screwed into the adapter.

The construction rail and adapters for the 3DFM lid were machined out of aluminum at the UNC Physics Department machine shop. The XYZ Translation stage is bolted into

the construction plate through the stage base plate. These three components, assembled, form the basic modular unit for the motorized 3DFM as shown in Figure 8.5.

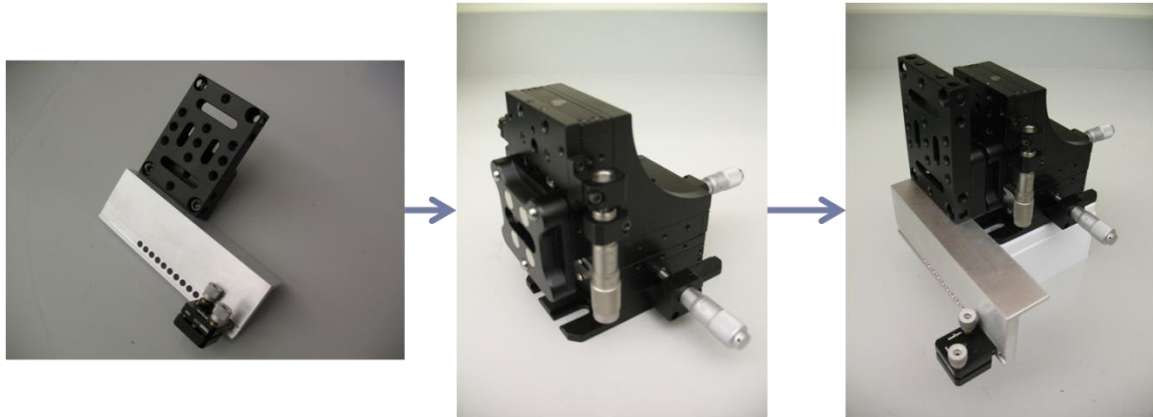


Figure 8.5 Assembly of the motorized 3DFM.

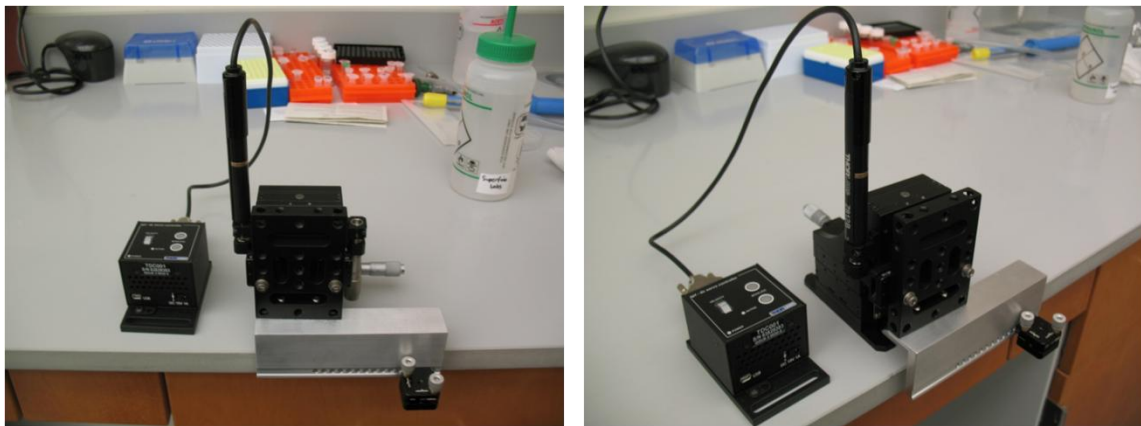
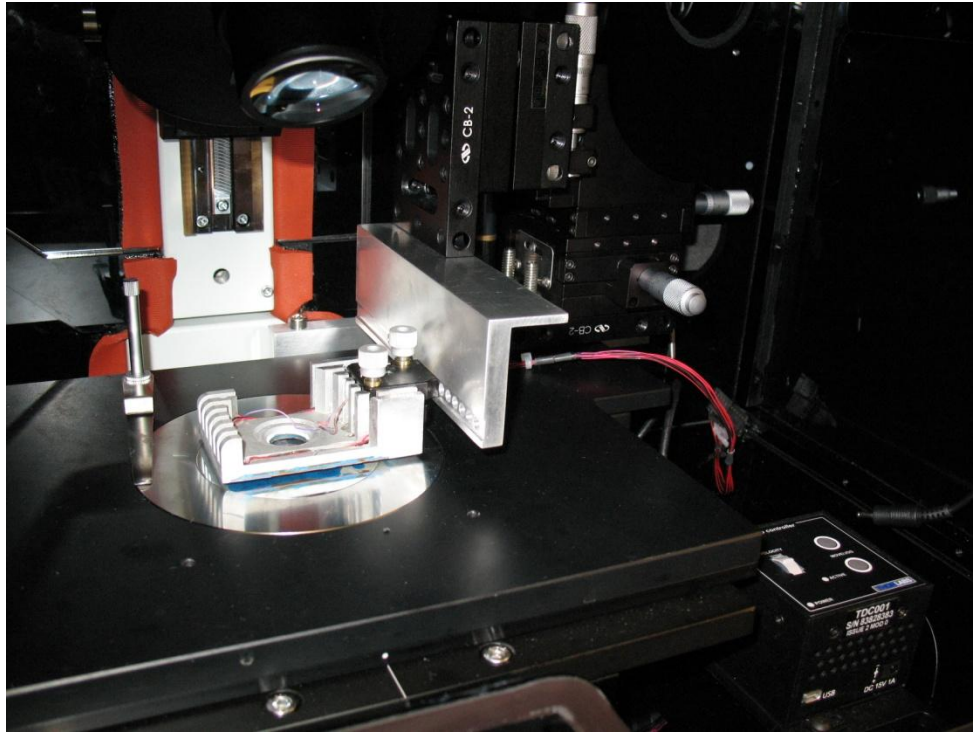


Figure 8.6. Assembled motorized stage. Controller is attached to the motor. The device is ready to be installed in the microscope chamber.

With the motor attached, the unit is ready to be installed onto the microscope. The rear of IX81 microscope stage is connected to the microscope stage with two M4 screws. These screws were removed, and the adapter was screwed into the microscope stage using 2 new M4 screws, sufficiently long enough to reach through the adapter and screw into the stage. With the 3DFM stage in place, the motor can be attached to the T-Cube DC Servo Controller. The power supply for the motor and the 3DFM are pulled

through a gasket on the side of the environmental chamber and connected to the respective components. The final installation is shown in Figure 8.7.



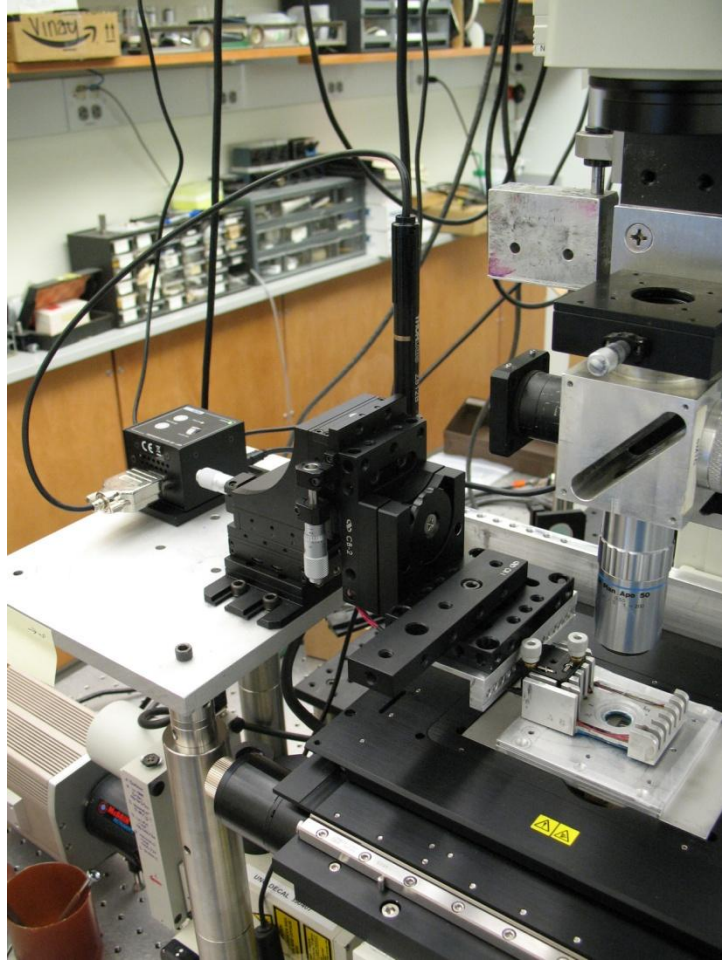


Figure 8.7 Final installation of the 3DFM. The top image shows the installation inside of the environmental chamber. The bottom image shows the installation on the Nikon Eclipse TE.

This design was also implemented on the Nikon Eclipse TE 2000-E microscopes with modifications to the adapter to accommodate the different dimensions of those scopes. The benefit of this system is a greatly improved resolution for translating the pole tip along the z-axis. The micrometers and the motor allow for a much easier and repeatable positioning of the pole tip. When changing the sample, the lid can be lifted off and lowered back down to the same z-position in a repeatable manner. Positioning the pole tip in z was previously a more time consuming, but necessary part of the experiment.

This device makes it incredibly quick and experiments can begin within a minute of placing the sample onto the microscope.

8.2 Appendix Two: Cell Lines

There are several types of HeLa cells that are used in transfection experiments as well as a several specially modified to express fluorescent cytoskeletal components. They are described in this section.

8.2.1 HeLa Wild Type, Luc-705 and EGFP-654

The cell line used in these studies is the cervical cancer HeLa cell line, and is provided by Ryszard Kole and Rudy Juliano of the University of North Carolina, Chapel Hill Department of Pharmacology. HeLa cells are named after Henrietta Lacks, a woman who died from cervical cancer in 1951 Baltimore, Maryland. (Lucey, Nelson-Rees et al. 2009) Cancer cells as a result of a biopsy resulted in the establishment of the first immortalized human cell. Cervical cancer is a malignancy of the cervix. There are 3 genotypes used in the studies covered in this dissertation. HeLa wild type cells, HeLa Luc-705, and HeLa EGFP-654 were used for transfection and cell mechanics studies. HeLa wild type cells are the characteristic cells of cervical cancer. Cervical cancer is characterized as a malignant neoplasm of the cervix uteri. HeLa Luc-705 are HeLa wild type cells that have been stably transfected with a luciferase gene bearing an intron possessing an aberrant mutation typical of the autosomal recessive disease, β -Thalassemia. (Kang, Cho et al. 1998) Modeling the aberrant splicing of hemoglobin pre-mRNA, the luciferase protein is aberrantly expressed, resulting in very low levels of fluorescence. When the splice correcting antisense oligonucleotides are successfully

delivered to the cell nucleus, the aberrant splicing is corrected, resulting in properly expressed luciferase. EGFP is similarly used as a marker for expression in the HeLa EGFP-654 cells. The cell lines are grown at 37.0°C and 5.0% CO₂. HeLa wild type and HeLa EGFP-654 cells are maintained in DMEM/F12 with L-glutamine and HEPES buffer supplemented with 10% fetal bovine serum. Growth media was further supplemented with antibiotic-antimycotic. (Penicillin-Streptomycin and Amphotericin B, Invitrogen) HeLa Luc-705 cells are grown in DMEM supplemented with 10% fetal bovine serum.

β -Thalassemia is an autosomal recessive disorder of the blood which results from improper expression of hemoglobin in red blood cells. (Busslinger, Moschonas et al. 1981) That is, the trait must be carried by both the mother and father and both parents must pass the gene on to the child in order for the child to express the phenotype. Hemoglobin consists of two types of protein, a α -globin and a β -globin. β -Thalassemia is a disorder affecting the β -globin component of the protein.

8.2.2 HeLa GFP-Actin and RFP Tubulin

For single cell studies, fluorescence microscopy enables us to observe intracellular organelle activity that is not visible via bright field microscopy. Typically speaking, organelles are not visible through bright field microscopy, save for the nucleus. Sometimes darkly colored organelles can be observed, such as the pigment bearing melanosomes in *Xenopus melanophores*. In general, it is necessary to fluorescently label cells with fluorescent stains or antibodies that are targeted to the cellular components of interest. This is made possible by the wide range of fluorescent labels designed to

illuminate the cell since the early 1970's. To observe cytoskeletal behavior, HeLa cells were transfected with Fluorescent Protein Cellular Labels: Cellular Lights™ Reagents. These reagents use baculoviruses to introduce DNA into the host cell that codes for the cytoskeletal monomer subunits associated with fluorescent proteins. HeLa cells were transfected for GFP-Actin and RFP-Tubulin in separate cell cultures.

To transfect with the cellular lights reagents, HeLa cells were grown to ~80% confluence in two T-75 cell culture flasks. One flask was designated for GFP-Actin and the other designated for RFP-Tubulin. According to the manufacturer's specifications, 25µl of DMSO was added to the provided "enhancer" solution. Two ml of the Cellular Lights™ reagent was added to 3.0ml of PBS without Ca^{2+} or Mg^{2+} . The cell culture media from each flask was removed and Cellular Lights™ transduction reagent for GFP-Actin and RFP-Tubulin was added to the respective flask. The flasks were then allowed to incubate at room temperature, 23.0°C, for 4 hours. The transduction reagent was aspirated from the flasks, and replaced with DMEM F12 with 10% serum and 0.1% enhancer solution. The cells were then incubated at 37.0°C and 5.0% CO_2 for two hours. After the two hours, the cells were aspirated and replaced with DMEM F12 and 10% serum and allowed to incubate at 37.0°C and 5.0% CO_2 overnight (~20 hours). At the completion of the transfection, the cells were trypsinized and frozen in DMEM F12 with 10% DMSO. Since the transfection is not stable, it is necessary to preserve the fluorescence via cryopreservation. Cells were divided into aliquots of 100µl in 500µl cryotubes. Cell number was counted via a hemocytometer and the final concentration was 3000 cells/µl. The low volume in the cryotube is intended to facilitate easy plating of the cells for experimentation directly out of the -80.0°C freezer. The HeLa cells were

found to be able to survive multiple freeze/thaw cycles, enabling usage of the majority of the cells in the cryotube.

To verify the transfection results, images and z-stacks were taken of both cell types. Both coverslips exhibited essentially 100% transfection. Scanning the coverslip produced no examples of cells not expressing the fluorescent cytoskeletal component that it had been transfected for. Cells were imaged at 40X, 60X, and 100X. At 100X and 0% neutral density filtering, it was observed that the fluorescence had a tendency to fade and deleteriously affect the cells, resulting in blebbing of the cells. Upon application of an 80% neutral density filter, cell death was not observed. Example images are shown below.

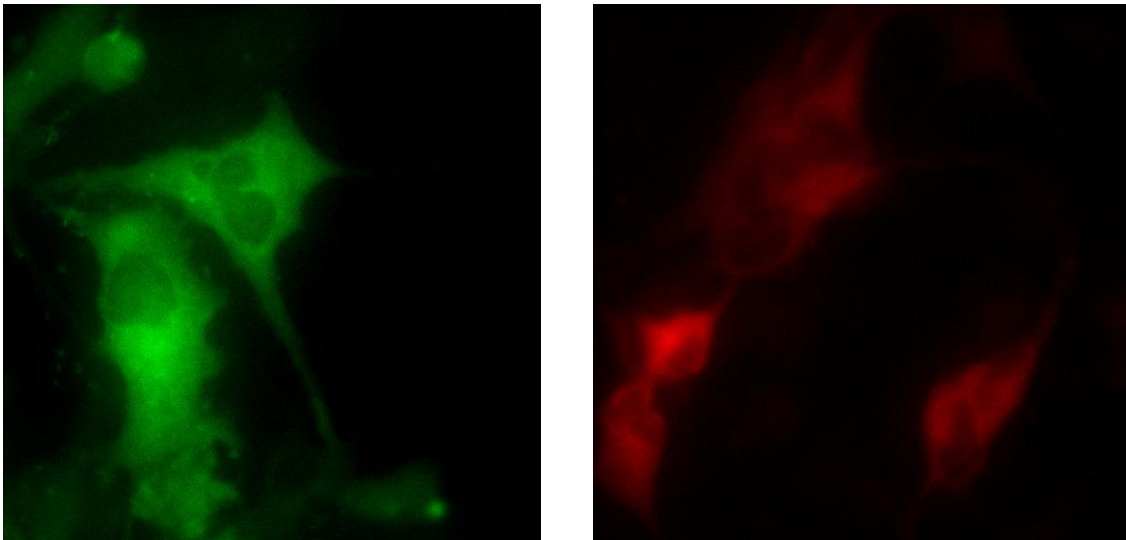


Figure 8.8 Images to verify efficacy of fluorescent actin and tubulin transfection. (Left) GFP-Actin HeLa cells. (Right) RFP-Tubulin HeLa Cells

8.3 Appendix Three: Chapter 2

8.3.1 Polyethylenimine/Nanoparticle Functionalization

PEI is functionalized to the particles via an EDAC (1-ethyl-3-(3-dimethylaminopropyl)-carbodiimide hydrochloride) reaction. To prepare the carboxylic acid functionalized beads, a 10 mg/ml concentration of EDAC is made by adding crystalline powder to 1 ml of 0.1M MES (2-[N-Morpholino]ethane-sulfonic acid) buffer at pH 4. Then 250 μ l of EDAC/MES are added to 50 μ l of particles in a 1.5 ml microcentrifuge tube. The beads are sonicated for 15 minutes and vortexed. Concurrently, 60mg of PEI are measured out into another 1.5 ml microcentrifuge tube. To this was added 1 ml of MOPS (3-[N-Morpholino] Propane Sulfonic Acid) at a pH 12. It is vortexed vigorously to ensure it is well mixed. The beads and PEI are allowed to rotate overnight at room temperature. After 12 hours, 150 μ l of the PEI solution (60mg/ml) is added to the particles, vortexed, and allowed to rotate for 4 hours. The particles are centrifuged into a pellet and excess PEI is decanted. The particles are washed 3 times in Dulbecco's phosphate buffered saline (PBS) to remove excess PBS. The particles are resuspended in 500 μ l of PBS for a final particle concentration of 1 mg/ml. This protocol was used for all particles with the exception of the Chemicell particles, which come from the manufacturer already functionalized for transfection, and the Micromod PEI 250nm particles.

8.3.2 Cell Plating

To test for the effectiveness of the different particle types they were used to transfect HeLa-Luc 705 cells. HeLa-Luc 705 cells are grown in T-75 cell culture plates in DMEM to roughly 80% confluence before passaging. The DMEM is supplemented with 4.5mg/ml glucose, L-glutamine, and sodium pyruvate, and further supplemented with 10% fetal bovine serum. The cells are washed once with PBS, trypsin is added, and re-suspended with DMEM. A sample of the cells is removed for the purpose of counting cells with an electronic cell cytometer, to determine the number of cells/ml. Once this is done the cells are plated at a density of 125,000 cells per well in two 12-well TPP cell culture plates 24 hours prior to transfection. The cells are plated in the DMEM formulation described above. These plates are specially treated to facilitate cell adhesion and growth at the bottom of the well. One plate is intended for magnetic transfection and the other is a control for nonmagnetic transfection. The 12-well plates are incubated at 37.0°C and 5.0% CO₂.

For the post particle transfections, HeLa EGFP-654 cells were plated at 5000 cells per well 24 hours before transfection in a Nunc 384 well plate. Before transfection cell media was replaced with Opti-MEM I Reduced-Serum Medium (Invitrogen, Carlsbad, CA).

8.3.3 Cell Culture

HeLa Luc-705 cells are grown at 36.5°C and 3.5% CO₂ in Dulbecco's Modified Eagle Medium with F-12 nutrient mixture (Invitrogen, Carlsbad, CA) with L-glutamine and HEPES buffer supplemented with 10% fetal bovine serum.

HeLa EGFP-654 cells are grown at 36.5°C and 3.5% CO₂ in Dulbecco's Modified Eagle Medium with F-12 nutrient mixture (Invitrogen, Carlsbad, CA) with L-glutamine and HEPES buffer supplemented with 10% fetal bovine serum. Growth media was further supplemented with antibiotic-antimycotic (Penicillin-Streptomycin and Amphotericin B, Invitrogen).

8.3.4 Luciferase Assay

To assay the cells the cell lysate must be collected for analysis in a luminometer and protein concentration. The cells were lysed for analysis of luciferase expression in the manner prescribed by the Promega Luciferase Assay Kit. Briefly, the Promega 5X lysis buffer is diluted 1 to 4 by volume in water, allowed to come to room temperature. Cell culture medium is removed and the cells are washed with PBS, after which, 200µl of lysis buffer are added to each well. After 15 minutes the wells are scraped and collected into individual 1.5ml centrifuge tubes. These tubes are placed in a dry ice and ethanol bath for 5 minutes to freeze the cells and fracture the cell membrane. After freezing, the tubes are allowed to come back to room temperature, vortexed, and centrifuged at 14000×g for 2 minutes. After properly priming and calibrating the luminometer, 20 µl of cell lysate from each sample is transferred individually into a glass luminometer tube. To this tube is added 100 µl of Promega Luciferase Assay Reagent. The tube is placed in the luminometer, and fluorescence is measured. This returns a measure of luciferase expression in terms of Relative Light Units (RLU).

8.3.5 BCA Protein Assay

To normalize the values obtained from the luminometer, a BCATM (bicinchoninic acid) Protein Assay is performed. Six dilutions of BSA (bovine serum albumin) are prepared in triplicate in the first 18 wells of a 96-well plate as a standard for protein concentration. For each sample of cell lysate 10 µl are placed into a well of the 96-well in triplicate. To these wells, 200 µl of a 50:1 solution of BCATM Reagent A to BCATM Reagent B are added. The plate is placed in the incubator for 30 minutes at 37°C. The plate is removed from the incubator and placed in the 96 well plate reader where absorbance is measured at 562nm to return the protein concentration. Using the data retrieved from the luminometer reading, a calculation of RLU/µg protein made, normalizing across all samples. The BCA measures total protein concentration in the cell lysate not just the luciferase concentration. The concentrations of the transfected cells are compared with that of untreated cells, and the two should be similar. Significant decreases in concentration below that of the untreated cells are indications of toxicity in the cell culture.

8.3.6 Transfection Reagent Preparation

For the Chemicell particles, 2.8 µl of beads were combined with 5 µl of oligonucleotide as recommended in the online protocol. For the other 9 samples, 20 µl of beads were mixed with 10 µl of oligonucleotide. To all were added 100 µl of PBS. These were allowed to rotate for an hour. After an hour Opti-MEM[®] 1 Reduced-Serum Medium (1X) was added to each to produce a final volume of 1 mL in each tube. When added to the cell cultures the final oligo concentration was 500nM. A sufficient amount

of sample was produced for both the magnetic and the non-magnetic transfection. Concurrent with this, Lipofectamine-2000 and oligonucleotide were mixed in Opti-MEM at a ratio of 5:5:90. (Ming, Sato et al. 2011) The Lipofectamine solution was placed on a rotator for 30 minutes. This solution was added to the cell culture in triplicate to achieve a 50nM concentration.

8.3.7 Dose Response Reagent Preparation

To conjugate the antisense oligonucleotide to the particles, 50 μ l of oligonucleotide (50 μ M) is added to 250 μ l of the 130nm particles (1mg/ml) and 200 μ l of sterile PBS. The mixture was vortexed for 5 seconds and then placed on a rotator to mix for 1 hour. Concurrently, Lipofectamine-2000 and oligonucleotide were mixed in Opti-MEM at a ratio of 5:5:90. The Lipofectamine solution was placed on a rotator for 30 minutes. While the transfection reagents were being mixed the cell culture media was replaced with Opti-MEM low serum culture media. The oligo/bead conjugates were added to individual wells of the 12 well plate to achieve oligo concentrations of 2.5, 12.5, 25, 50, 75, 100, 125, 250, 500 nM. A single concentration of 50 μ M Lipofectamine 2000 sample was used and performed in triplicate. At this stage of the experiments, the primary focus was to establish useful dosages for the bead/oligo conjugates to achieve optimal transfection and minimal toxicity. Therefore the bead concentrations were not being directly compared with the Lipofectamine. The Lipofectamine served as a control to verify that the cells would express when transfected using a previously established methodology.

8.3.8 Imaging/Segmentation

Treated and untreated cells were imaged using a Nikon Eclipse TE 2000-E inverted optical microscope (Tokyo, Japan) with a 40x objective. Images were taken using a Photometrics Cascade II 512 electron multiplying CCD digital camera (Roper Scientific, Inc., Tuscon, AZ) and background fluorescence was established by performing segmentation imaging on highest intensity cells in untreated samples. Imaging and segmentation was performed with IPLab 4.0 (BD Biosciences Bioimaging, Rockville, MD). Cells measuring above this background fluorescence in treated samples were measured for mean intensity using segmentation. Mean background fluorescence was subtracted to determine the true mean intensities above background for treated cells. An average of 20 images is taken of each well and weighted mean intensities were summed over all images.

8.3.9 Size Uniform 200nm Fe Post Particles

Size-uniform 200nm Fe_3O_4 particles were fabricated by L. Mair as described in our paper “Size-uniform 200nm particles: Fabrication and application to magnetofection”. Briefly, these particles are lithographically defined metallic particles and grown via thermal deposition. SEM images of the particles are shown in Figure 8.9.

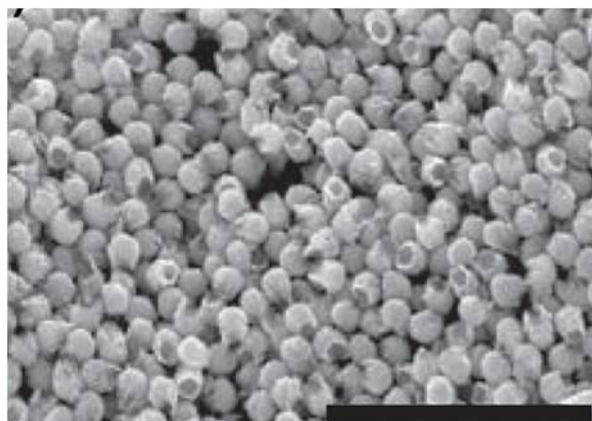


Figure 8.9 Scanning electron micrograph of the size-uniform 200nm Fe_3O_4 . Scale bar is 20 μm .

To make the particles useful for transfection, the particles had to be surface functionalized with PEI. PEI was bound to the Fe Post-Particles by mixing the particles (1mg/ml) with 0.1mg PEI for 4 hours in a DI water adjusted to pH 10 using 0.1M NaOH. At this pH the zeta potential of the particles is sufficiently low to electrostatically bind cationic PEI to the particle surface.

8.4 Appendix Four: Chapter 4

8.4.1 Cell Plating

To perform AC transfections, HeLa EGFP-654 cells are plated at a density of 125,000 cells per well in a 12 well plate 24 hours prior to transfection. To test the frequency dependence and vibration effects, cells are plated in 96 well plates at a density of 12,000 cells per well. Cells are counted with a hemacytometer and plated in DMEM/F12 with L-glutamine and HEPES buffer supplemented with 10% fetal bovine serum. Growth media was further supplemented with antibiotic-antimycotic (Penicillin-Streptomycin and Amphotericin B, Invitrogen). Cells are grown at 37.0°C and 5.0%

CO₂. One hour prior to transfection, the cell culture media is replaced with Opti-MEM low serum media

8.4.2 Transfection Reagent Preparation

To conjugate the antisense oligonucleotide to the particles, 130nm particles (1mg/ml) are mixed with the oligonucleotide (50μM) and phosphate buffered saline at a 25:5:70 volume ratio. Total volume is adjusted to accommodate the volume needed for the experiment. Simultaneously, oligos are mixed with Lipofectamine 2000 and Opti-MEM at a 5:5:90 ratio by volume. The nanoparticle and Lipofectamine solutions are added to their respective wells of the 12-well plates to achieve 50nM concentrations.

8.4.3 Cell Imaging and Counting Assay

The cells are stained with SYTO 82 nucleic acid stain and imaged for EGFP expression on an Olympus IX81 confocal microscope. The cells are imaged at 10X, 0.3NA, and imaged consecutively in the Texas Red and GFP channels using Metamorph. To analyze the results fluorescent cells were counted in ImageJ. The SYTO 82 stains all of the cells in the sample red, enabling us to count the total number of cells in an image. By imaging the untransfected cells, we can establish the baseline fluorescence. The cell counting protocol goes as follows. The image is opened in ImageJ and using the color picker tool a bright pixel is selected. The paintbrush tool is then used to “paint” a dot onto a cell with the same intensity chosen with the color picker. A dot is placed over every cell in the image. This is shown in Figure 8.10.

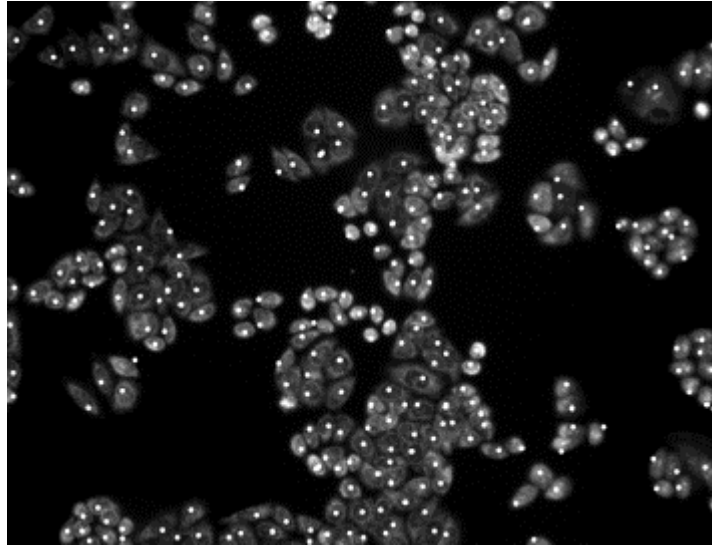


Figure 8.10 Example of SYTO 82 stained cells. The white dots are placed in ImageJ to count the cells.

With all of the cells labeled with a dot the image threshold is adjusted using the Image→Adjust→Threshold tool. This tool converts the image to black and white and allows the user to isolate only the pixels above or below a certain threshold. With the dots at a high intensity value the threshold is adjusted to a high pixel value, leaving only the dots in the image. (Figure 8.11)

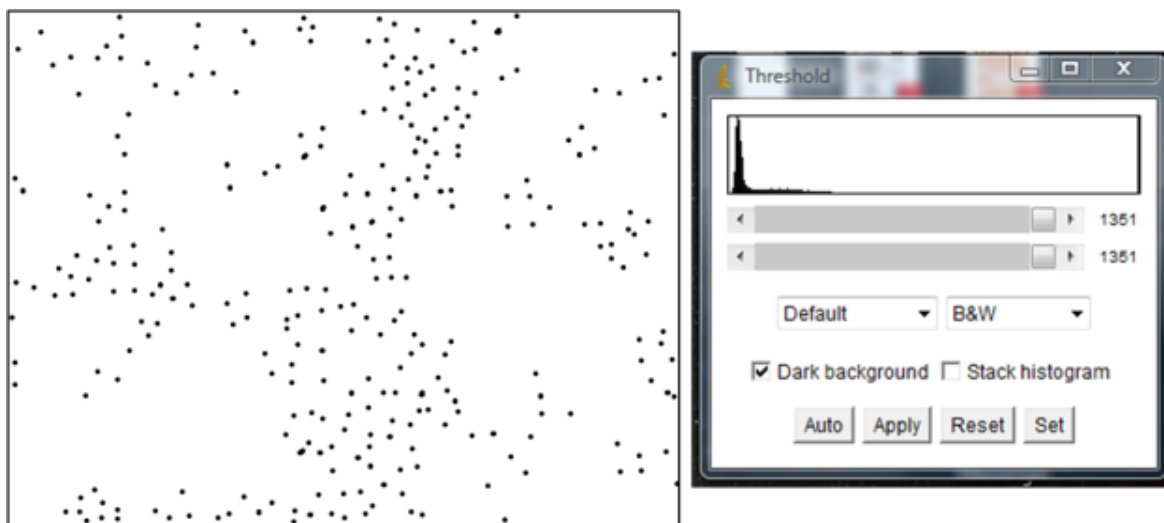


Figure 8.11 ImageJ screenshot where threshold is adjusted cell image. Adjusting the threshold removes everything from the image except the dots, which act as proxies for the cells.

The dots serve as proxies for the counted cells. It is possible for ImageJ to count cells without this step, but the non-uniformity of pixel intensities caused multiple parts of a single cell to be counted as individual objects, causing the cell count to be inflated. By “non-uniformity of pixel intensities”, I am referring to certain features of the cell being brighter or darker in an uneven manner, and not in a monotonic or concentric way. This technique ensured that each cell would be counted only once. Once the threshold is suitably adjusted, then ImageJ is ready to count the objects in the image. I wrote a small macro that would accomplish this by converting the image into a binary image and then count the dots. (Figure 8.12)

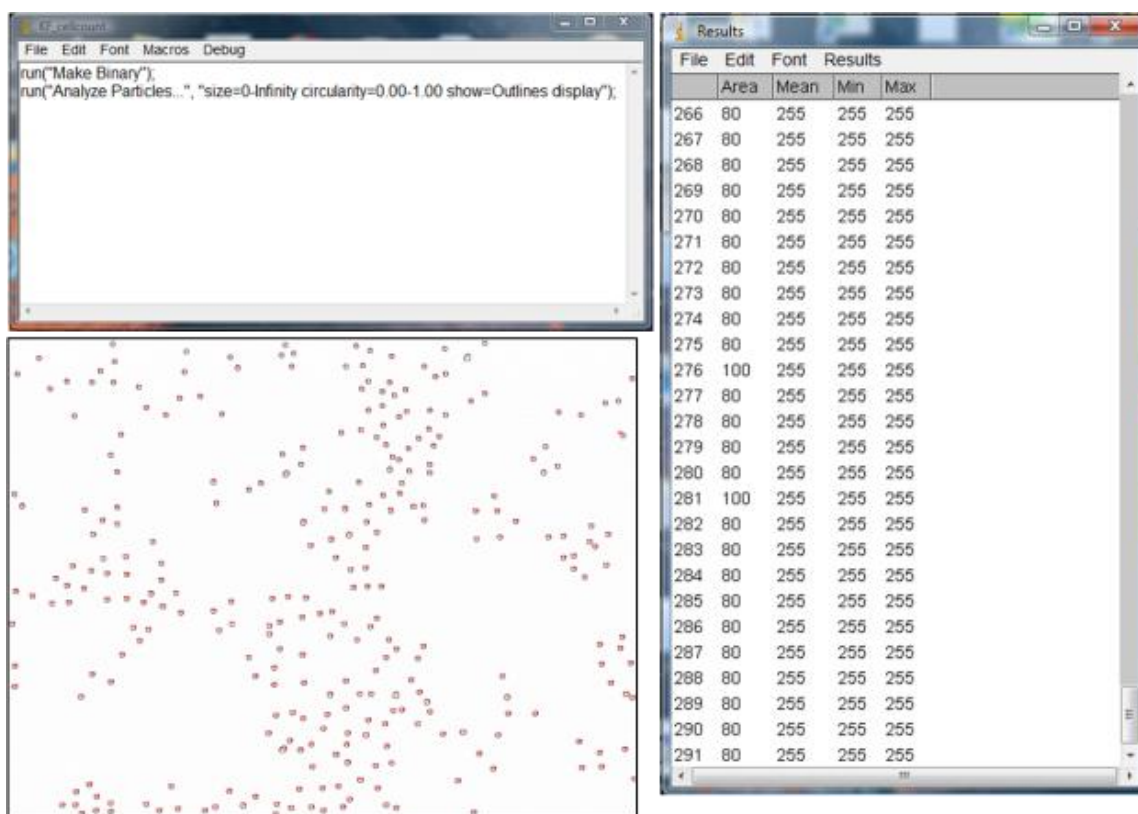


Figure 8.12 ImageJ screenshot showing cells being counted. The box on the right displays the results.

In Figure 8.12 the window at the top left shows the macro for cell counting and the window on the right shows the results of the cell count. Because it is counting uniform dots the area is uniformly 80 pixels, with a few exceptions when the paintbrush tool is slightly dragged in the counting process. Also uniform are the pixel intensities as shown by the pixel intensities of 255. The value at the bottom of the leftmost column of the results window shows the total number of cells in the image, and this value is entered into an Excel spreadsheet.

To count the cells that are expressing the EGFP as a result of transfection, a similar process is followed. The untreated HeLa EGFP-654 cells produce a low level of

background fluorescence; due to the fact that is producing an aberrantly expressed EGFP protein. For untreated cells images it was found that adjusting the threshold of the image above a pixel intensity of 450 removed all cells from the images, indicating that the untreated cells did not fluoresce above this intensity. To select for transfected cells in the images, the threshold was adjusted to show pixel intensities above 500. This effectively isolated the fluorescent cells for counting. An image of the threshold adjusted image and actual image were looked at simultaneously. Using the threshold image as a guide, dots were placed on the expressing cells. (Figure 8.13)

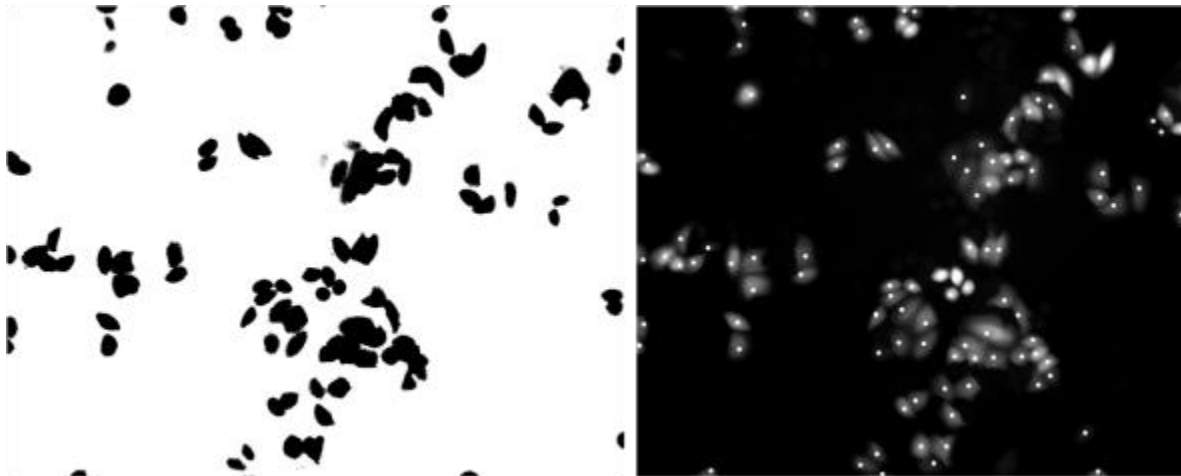


Figure 8.13: Image of EGFP expressing cells in the cell counting pipeline

With the dots placed on the cells these cells are counted as described previously and then the number is recorded in the same spreadsheet. For each sample (Lipofectamine, AC, etc.) at least 2000 cells were counted. A ratio of the EGFP expressing cells to the total cells is calculated to produce a transfection rate. Data are presented as transfection rate \pm SE, with the standard error calculated on the transfection rate among all the images. The images are also colorized in ImageJ to match the color of the respective fluorophore.

The images are merged together and in the merged examples the expressing cells can be seen as yellow.

8.4.4 Oscillating Field Effects are not Due to Vibration of the Sample

Any time moving components are incorporated into a device, it is logical to assume that there is some level of resonant vibration being produced by the moving parts. If a cell culture is placed on such a device the sample will also experience a vibrational force due to the movement of the array. The effects on the vibration are thus tested to verify that they do or do not have an effect on the transfection.

Prior to transfection, the cell media is replaced with Opti-MEM reduced serum media. Nanoparticle/oligo solution is added to the cell cultures to achieve 200 μ M concentrations. After dosing with particles, the cell media is mixed by gently pipetting up and down several times to evenly distribute the particles. Both samples are placed on a permanent magnet to sediment the particles for 30 minutes. After the 30 minute sedimentation time, the magnet is removed and the cell media is changed to DMEM/F12 with 10% FBS to remove free nanoparticles from solution.

To test for vibration effects, the magnet array that is used for the oscillating magnetic field experiments is replaced with non-magnetic aluminum components of approximately equivalent mass. This is done to simulate the mass that is rotating with the magnet array and the level of vibration that would be produced. After the initial particle sedimentation and media change, the cell culture is placed over the rotating non-magnetic aluminum array. This array is rotated at a speed equivalent to the 10 Hz oscillating application. One of the cell cultures undergoes this vibration test for 30 minutes, as is done with the magnetic transfections. The other sample receives no additional

stimulation. After the vibration application, the cells are allowed to incubate for 24 hours before imaging.

The results of the vibration effects are shown in Figure 8.14.

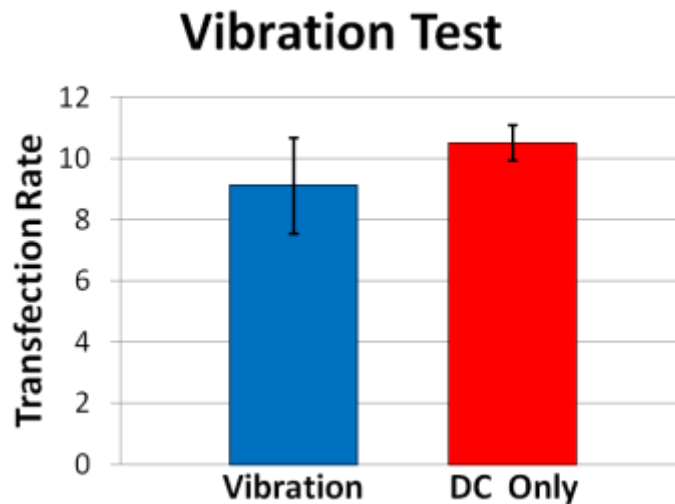


Figure 8.14 Vibration of the sample does not produce a improvement of transfection efficiency.

The transfection efficiency of the DC only sample was $10.51\% \pm 0.58$ as compared to $9.12\% \pm 1.56$ for the vibration test. These data indicate that there is no impact in enhancing the transfection efficiency due to oscillation of the moving components of the array.

8.5 Appendix Five: Chapter 5

8.5.1 Cell Plating

To perform the Latrunculin B experiments, HeLa EGFP-654 cells are plated at a density of 5,000 cells per well in a 384 well plate 24 hours prior to transfection. Cells are counted with a hemacytometer and plated in DMEM/F12 with L-glutamine and HEPES

buffer supplemented with 10% fetal bovine serum. Growth media was further supplemented with antibiotic-antimycotic (Penicillin-Streptomycin and Amphotericin B, Invitrogen). Cells are grown at 37.0°C and 5.0% CO₂.

For pathway inhibition studies, HeLa EGFP-654 cells are plated on 96-well plates at a density of 12,000 cells per well 24 hours prior to experimentation. Cells are cultured in DMEM/F12 media as described previously. Prior to transfection experiments, cell culture media is replaced with Opti-MEM low serum medium. Inhibitory drugs are added to Opti-MEM to achieve the desired concentrations. Chlorpromazine (14μM), Nystatin (200IU/mL), and Amiloride (100μM) were used to inhibit the Clathrin-mediated, lipid raft, and macropinocytosis pathways respectively. Dynamin, a motor protein that is necessary for multiple endocytic pathways, was inhibited with Dynasore (80μM).

8.5.2 Transfection Reagent Preparation

To conjugate the antisense oligonucleotide to the particles, 130nm particles (1mg/ml) are mixed with the oligonucleotide (50μM) and phosphate buffered saline at a 25:5:70 volume ratio. Total volume is adjusted to accommodate the volume needed for the experiment. Simultaneously, oligos are mixed with Lipofectamine 2000 and Opti-MEM at a 5:5:90 ratio by volume. The nanoparticle and Lipofectamine solutions are added to their respective wells to achieve 50nM concentrations.

8.5.3 Endocytic Pathway Inhibition

The cell line used in these studies is the cervical cancer HeLa EGFP-654 cell line, provided by Ryszard Kole of the University of North Carolina, Chapel Hill Department of Pharmacology, described in section 8.2.1. HeLa EGFP-654 cells have been stably transfected with an EGFP gene bearing an intron possessing an aberrant mutation typical of the autosomal recessive disease, β -Thalassemia (Kang, Cho et al. 1998). The cell lines are grown at 37.0°C and 5.0% CO₂ and are maintained in DMEM/F12 with L-glutamine and HEPES buffer supplemented with 10% fetal bovine serum. Growth media was further supplemented with antibiotic-antimycotic (Penicillin-Streptomycin and Amphotericin B, Invitrogen).

Twenty-four hours prior to experimentation, the cells are plated on 96-well plates at a density of 12,000 cells per well. Cells are cultured in DMEM/F12 media as described previously. Prior to transfection experiments, cell culture medium is replaced with Opti-MEM low serum medium. For endocytosis pathway studies, inhibitory drugs are added to Opti-MEM to achieve the desired concentrations.

8.5.4 Cell Staining and Imaging

The cells are stained with SYTO 82 nucleic acid stain (Invitrogen, 500nM) or DAPI (Invitrogen, 2.85 μ M) and imaged for EGFP expression on an Olympus IX81 confocal microscope. The stains are diluted in Opti-MEM, added to the cells, and incubated for 10 minutes. The staining media is replaced with fresh Opti-MEM prior to imaging. The cells are imaged with a 10X, 0.3NA, Olympus air objective. Cell images are captured consecutively in the Texas Red and GFP channels using Metamorph. To

analyze the results, cells were counted in ImageJ. The total number of cells in the field of view is counted via the Texas Red channel and cells fluorescing above background fluorescent levels are counted in the GFP channel. The untreated HeLa EGFP-654 cells produce a low level of background fluorescence. To quantify the background level of untransfected cells, the threshold of the images is adjusted until the cells are no longer visible. This intensity value is averaged over several images. To count a cell as expressing above background fluorescence, it must exceed this threshold by 11%. For example, if untreated cells are no longer visible by adjusting the threshold to 450, cells that have intensities of 500 or greater are counted as EGFP expressing. Transfection efficiency is determined by calculating the ratio of EGFP expressing cells to the total number of cells in the field of view. A minimum of 2000 cells were counted for each sample and standard error of the mean (SEM) is calculated over multiple fields of view of the sample.

8.5.5 Imaging and Cell Counting

Twenty-four hours after transfection the cells are stained with SYTO 82 nucleic acid stain. Cells are imaged for EGFP expression on an Olympus IX81 confocal microscope. The cells are imaged at 10X, 0.3NA, and imaged consecutively in the red and green channels. To analyze the results fluorescent cells were counted using ImageJ. The SYTO 82 stains all of the cells in the sample red, enabling us to count the total number of cells in an image. By imaging the untransfected cells, we can establish the baseline fluorescence. To measure for transfection in the transfected samples, the threshold for the images was adjusted above the intensity levels for the baseline samples. Cells fluorescent above this threshold were counted as the expressing cells. For each

sample at least 2000 cells were counted. The images are merged and in the merged examples the expressing cells can be seen as yellow.

8.6 Appendix Six: Chapter 6

8.6.1 Cell Culture and Plating

To plate cells for the active transport experiments, 22X50 mm 1½ glass coverslips were sterilized by removing them from a 100% ethanol bath and igniting them with a butane lighter. Polystyrene cloning rings (4.7mm inner diameter, Fisher Scientific) were affixed to the center of the coverslips using high vacuum silicon grease, forming the cell culture well. DMEM with F12, supplemented with 10% fetal bovine serum and antibiotic/antimycotic (Penicillin-Streptomycin and Amphotericin B, Invitrogen), was added to the inside of the cloning rings (300 µl). The DMEM is also buffered with HEPES (4-(2-hydroxyethyl)-1-piperazineethanesulfonic acid) to maintain the pH when the sample is out of the incubator. HeLa WT cells are seeded inside of the cloning rings to an approximate 10% confluence level. The cells are allowed to incubate overnight to allow for the cells to come down and adhere to the coverslip.

8.6.2 1µm Bead Dosing and Imaging

The 15µl of the 1µm MyOne beads with Lipofectamine are added to the cells. The cells are then incubated in the presence of the beads for 2-4 hours. This allows enough time for the beads to sediment to the bottom of the cell culture dish and for endocytosis to commence.

The cells are then placed into the Olympus IX81 environmental chamber. Prior to imaging, the environmental chamber has been set to 37.0°C. Imaging is performed at 100X magnification. The cell culture is visually scanned to find examples of cells with MyOnes that have undergone endocytosis and can be seen as undergoing active transport. Often multiple beads can be seen in a single cell. Transport can be easily observed as bi-directional transport characteristic of molecular motor transport. Once a suitable candidate is found, time lapse video is captured at 60 frames per second.

Bibliography

- Akinc, A., M. Thomas, et al. (2005). "Exploring polyethylenimine-mediated DNA transfection and the proton sponge hypothesis." The Journal of Gene Medicine **7**(5): 657-663.
- Alberts, B., A. Johnson, et al. (2002). Molecular biology of the cell, Garland Science Taylor & Francis Group.
- Banerjee, A. G., S. Chowdhury, et al. "Survey on indirect optical manipulation of cells, nucleic acids, and motor proteins." Journal of Biomedical Optics **16**(5).
- Boussif, O., F. Lezoualch, et al. (1995). "A VERSATILE VECTOR FOR GENE AND OLIGONUCLEOTIDE TRANSFER INTO CELLS IN CULTURE AND IN-VIVO - POLYETHYLENIMINE." Proceedings of the National Academy of Sciences of the United States of America **92**(16): 7297-7301.
- Busslinger, M., N. Moschonas, et al. (1981). "BETA+ THALASSEMIA - ABERRANT SPLICING RESULTS FROM A SINGLE POINT MUTATION IN AN INTRON." Cell **27**(2): 289-298.
- Chapman, S. W. K., P. O. Hassa, et al. (2008). "Application of pulsed-magnetic field enhances non-viral gene delivery in primary cells from different origins." Journal of Magnetism and Magnetic Materials **320**(8): 1517-1527.
- Chesnoy, S. and L. Huang (2000). "Structure and function of lipid-DNA complexes for gene delivery." Annual Review of Biophysics and Biomolecular Structure **29**: 27-47.
- Chini, B. and M. Parenti (2004). "G-protein coupled receptors in lipid rafts and caveolae: how, when and why do they go there?" Journal of Molecular Endocrinology **32**(2): 325-338.
- D. Vainauska, M. B. (2011). "Improved Technique of Non-viral Gene Delivery into Cancer Cells." World Academy of Science, Engineering and Technology(58): 95-99.
- De Haes, W., G. Van Mol, et al. (2012). "Internalization of mRNA Lipoplexes by Dendritic Cells." Molecular Pharmaceutics **9**(10): 2942-2949.
- Desai, M. P., V. Labhasetwar, et al. (1997). "The mechanism of uptake of biodegradable microparticles in Caco-2 cells is size dependent." Pharmaceutical Research **14**(11): 1568-1573.
- Fawcett, D. W. (1965). "SURFACE SPECIALIZATIONS OF ABSORBING CELLS." Journal of Histochemistry & Cytochemistry **13**(2): 75-&.
- Fisher, J. K., L. Vicci, et al. (2006). "Magnetic force micromanipulation systems for the biological sciences." Nano **1**(3): 191-205.
- Footer, M. J., J. W. J. Kerssemakers, et al. (2007). "Direct measurement of force generation by actin filament polymerization using an optical trap." Proceedings of the National Academy of Sciences **104**(7): 2181-2186.

- Freed, J. J. and M. M. Lebowitz (1970). "ASSOCIATION OF A CLASS OF SALTATORY MOVEMENTS WITH MICROTUBULES IN CULTURED CELLS." Journal of Cell Biology **45**(2): 334-&.
- Gagliano, J., M. Walb, et al. (2009). "Kinesin velocity increases with the number of motors pulling against viscoelastic drag." European Biophysics Journal with Biophysics Letters **39**(5): 801-813.
- Gao, Z., L. Zhang, et al. "Nanotechnology applied to overcome tumor drug resistance." Journal of Controlled Release **162**(1): 45-55.
- Gennerich, A., A. P. Carter, et al. (2007). "Force-Induced Bidirectional Stepping of Cytoplasmic Dynein." Cell **131**(5): 952-965.
- Goncalves, C., E. Mennesson, et al. (2004). "Macropinocytosis of polyplexes and recycling of plasmid via the clathrin-dependent pathway impair the transfection efficiency of human hepatocarcinoma cells." Molecular Therapy **10**(2): 373-385.
- Hancock, J. F. (2006). "Lipid rafts: contentious only from simplistic standpoints." Nat Rev Mol Cell Biol **7**(6): 456-462.
- Henry, C. B. S. and B. R. Duling (1999). "Permeation of the luminal capillary glycocalyx is determined by hyaluronan." American Journal of Physiology - Heart and Circulatory Physiology **277**(2): H508-H514.
- Heslop, J. P. and E. A. Howes (1977). "SALTATORY MOVEMENTS OF ORGANELLES IN INTACT NERVES OF RHODNIUS-PROLIXUS STAL." Journal of Experimental Biology **70**(OCT): 247-&.
- Hewlett, L. J., A. R. Prescott, et al. (1994). "THE COATED PIT AND MACROPINOCYTIC PATHWAYS SERVE DISTINCT ENDOSOME POPULATIONS." Journal of Cell Biology **124**(5): 689-703.
- Hill, D. B., M. J. Plaza, et al. (2004). "Fast vesicle transport in PC12 neurites: velocities and forces." European Biophysics Journal with Biophysics Letters **33**(7): 623-632.
- Howard, J. (2001). Mechanics of motor proteins and the cytoskeleton. Sunderland, MA 01375, Sinauer Associates, Inc.
- Hsu, S.-h., T.-T. Ho, et al. (2012). "Nanoparticle uptake and gene transfer efficiency for MSCs on chitosan and chitosan-hyaluronan substrates." Biomaterials **33**(14): 3639-3650.
- Jenkins, S. I., M. R. Pickard, et al. (2011). "Magnetic Nanoparticle-Mediated Gene Transfer to Oligodendrocyte Precursor Cell Transplant Populations Is Enhanced by Magnetofection Strategies." Acs Nano **5**(8): 6527-6538.
- Jolly, A. L. and V. I. Gelfand (2011). "Bidirectional intracellular transport: utility and mechanism." Biochemical Society Transactions **39**: 1126-1130.

- Juliano, R. L., X. Ming, et al. (2012). "Cellular Uptake and Intracellular Trafficking of Antisense and siRNA Oligonucleotides." Bioconjugate Chemistry **23**(2): 147-157.
- Kafil, V. and Y. Omid (2011). "Cytotoxic Impacts of Linear and Branched Polyethylenimine Nanostructures in A431 Cells " BiolImpacts **1**(1): 23-30.
- Kamau, S. W., P. O. Hassa, et al. (2006). "Enhancement of the efficiency of non-viral gene delivery by application of pulsed magnetic field." Nucleic Acids Research **34**(5): 8.
- Kang, S. H., M. J. Cho, et al. (1998). "Up-regulation of luciferase gene expression with antisense oligonucleotides: Implications and applications in functional assay developments." Biochemistry **37**(18): 6235-6239.
- Kim, A. J., N. J. Boylan, et al. (2012). "Non-degradative intracellular trafficking of highly compacted polymeric DNA nanoparticles." Journal of Controlled Release **158**(1): 102-107.
- Kiss, A. L. and E. Botos (2009). "Endocytosis via caveolae: alternative pathway with distinct cellular compartments to avoid lysosomal degradation ?" Journal of Cellular and Molecular Medicine **13**(7): 1228-1237.
- Kulic, I. M., A. E. X. Brown, et al. (2008). "The role of microtubule movement in bidirectional organelle transport." Proceedings of the National Academy of Sciences of the United States of America **105**(29): 10011-10016.
- Kural, C., H. Kim, et al. (2005). "Kinesin and dynein move a peroxisome in vivo: A tug-of-war or coordinated movement?" Science **308**(5727): 1469-1472.
- Kural, C., A. S. Serpinskaya, et al. (2007). "Tracking melanosomes inside a cell to study molecular motors and their interaction." Proceedings of the National Academy of Sciences of the United States of America **104**(13): 5378-5382.
- Lee, E. and D. A. Knecht (2002). "Visualization of actin dynamics during macropinocytosis and exocytosis." Traffic **3**(3): 186-192.
- Liu, J., Y. D. Sun, et al. (2009). "The Mechanochemistry of Endocytosis." Plos Biology **7**(9).
- Loschi, M., C. C. Leishman, et al. (2009). "Dynein and kinesin regulate stress-granule and P-body dynamics." Journal of Cell Science **122**(21): 3973-3982.
- Lucey, B. P., W. A. Nelson-Rees, et al. (2009). "Henrietta Lacks, HeLa Cells, and Cell Culture Contamination." Archives of Pathology & Laboratory Medicine **133**(9): 1463-1467.
- Mair, L., K. Ford, et al. (2009). "Size-Uniform 200 nm Particles: Fabrication and Application to Magnetofection." Journal of Biomedical Nanotechnology **5**(2): 182-191.
- Mallik, R., B. C. Carter, et al. (2004). "Cytoplasmic dynein functions as a gear in response to load." Nature **427**(6975): 649-652.

- McBain, S. C., U. Griesenbach, et al. (2008). "Magnetic nanoparticles as gene delivery agents: enhanced transfection in the presence of oscillating magnet arrays." Nanotechnology **19**(40).
- Medina-Kauwe, L. K. (2007). ""Alternative" endocytic mechanisms exploited by pathogens: New avenues for therapeutic delivery?" Advanced Drug Delivery Reviews **59**(8): 798-809.
- Ming, X., K. Sato, et al. (2011). "Unconventional internalization mechanisms underlying functional delivery of antisense oligonucleotides via cationic lipoplexes and polyplexes." Journal of Controlled Release **153**(1): 83-92.
- Mukherjee, S., R. N. Ghosh, et al. (1997). "Endocytosis." Physiological Reviews **77**(3): 759-803.
- Nanbo, A., M. Imai, et al. "Ebola virus Is Internalized into Host Cells via Macropinocytosis in a Viral Glycoprotein-Dependent Manner." Plos Pathogens **6**(9).
- Nijenhuis, N., D. Mizuno, et al. "High-resolution microrheology in the pericellular matrix of prostate cancer cells." Journal of the Royal Society Interface **9**(73): 1733-1744.
- Nilsson, H., W. Steffen, et al. (2001). "In vitro reconstitution of fish melanophore pigment aggregation." Cell Motility and the Cytoskeleton **48**(1): 1-10.
- Pawlik, J. R. (1993). "MARINE INVERTEBRATE CHEMICAL DEFENSES." Chemical Reviews **93**(5): 1911-1922.
- Pelkmans, L. and A. Helenius (2002). "Endocytosis Via Caveolae." Traffic **3**(5): 311-320.
- Pelkmans, L., J. Kartenbeck, et al. (2001). "Caveolar endocytosis of simian virus 40 reveals a new two-step vesicular-transport pathway to the ER." Nature Cell Biology **3**(5): 473-483.
- Pelkmans, L., D. Puntener, et al. (2002). "Local actin polymerization and dynamin recruitment in SV40-induced internalization of caveolae." Science **296**(5567): 535-539.
- Pickard, M. and D. Chari (2010). "Enhancement of magnetic nanoparticle-mediated gene transfer to astrocytes by 'magnetofection': effects of static and oscillating fields." Nanomedicine **5**(2): 217-232.
- Prabha, S., W. Z. Zhou, et al. (2002). "Size-dependency of nanoparticle-mediated gene transfection: studies with fractionated nanoparticles." International Journal of Pharmaceutics **244**(1-2): 105-115.
- Reck-Peterson, S. L., A. Yildiz, et al. (2006). "Single-molecule analysis of dynein processivity and stepping behavior." Cell **126**(2): 335-348.
- Reitsma, S., D. W. Slaaf, et al. (2007). "The endothelial glycocalyx: composition, functions, and visualization." Pflügers Archiv-European Journal of Physiology **454**(3): 345-359.
- Rejman, J., V. Oberle, et al. (2004). "Size-dependent internalization of particles via the pathways of clathrin- and caveolae-mediated endocytosis." Biochemical Journal **377**: 159-169.

- Rosenfeld, S. S. and H. Lee Sweeney (2004). "A Model of Myosin V Processivity." Journal of Biological Chemistry **279**(38): 40100-40111.
- Roth, T. F. and K. R. Porter (1964). "YOLK PROTEIN UPTAKE IN THE OOCYTE OF THE MOSQUITO *AEDES AEGYPTI*. L." The Journal of Cell Biology **20**(2): 313-332.
- Scherer, F., M. Anton, et al. (2002). "Magnetofection: enhancing and targeting gene delivery by magnetic force in vitro and in vivo." Gene Therapy **9**(2): 102-109.
- Schmoller, K. M., C. Semmrich, et al. "Slow down of actin depolymerization by cross-linking molecules." Journal of Structural Biology **173**(2): 350-357.
- Sheetz, M. P. and J. A. Spudich (1983). "MOVEMENT OF MYOSIN-COATED STRUCTURES ON ACTIN CABLES." Cell Motility and the Cytoskeleton **3**(5-6): 485-489.
- Shtridelman, Y., G. M. Holzwarth, et al. (2009). "In vivo Multimotor Force-Velocity Curves by Tracking and Sizing Sub-Diffraction Limited Vesicles." Cellular and Molecular Bioengineering **2**(2): 190-199.
- Simons, K. and D. Toomre (2000). "Lipid rafts and signal transduction." Nature Reviews Molecular Cell Biology **1**(1): 31-39.
- Svoboda, K. and S. M. Block (1994). "FORCE AND VELOCITY MEASURED FOR SINGLE KINESIN MOLECULES." Cell **77**(5): 773-784.
- Swanson, J. A. (2008). "Shaping cups into phagosomes and macropinosomes." Nature Reviews Molecular Cell Biology **9**(8): 639-649.
- Swanson, J. A. and C. Watts (1995). "Macropinocytosis." Trends in Cell Biology **5**(11): 424-428.
- Teller, J. and C. Grüttner. (2012, October 24, 2012). "Technical Data Sheet." Version 2.2. from http://www.micromod.de/pdf/aktuell/09-02-252_tds_en.pdf.
- Weinbaum, S., J. M. Tarbell, et al. (2007). The structure and function of the endothelial glycocalyx layer. Annual Review of Biomedical Engineering. Palo Alto, Annual Reviews. **9**: 121-167.
- Yamamoto, M., Y. Toya, et al. (1998). "Caveolin Is an Activator of Insulin Receptor Signaling." Journal of Biological Chemistry **273**(41): 26962-26968.
- Yasuda, R., H. Miyata, et al. (1996). "Direct measurement of the torsional rigidity of single actin filaments." Journal of Molecular Biology **263**(2): 227-236.
- Zenni, M. K., P. C. Giardina, et al. (2000). "Macropinocytosis as a mechanism of entry into primary human urethral epithelial cells by *Neisseria gonorrhoeae*." Infection and Immunity **68**(3): 1696-1699.
- Zhang, X. X., P. G. Allen, et al. (2011). "Macropinocytosis Is the Major Pathway Responsible for DNA Transfection in CHO Cells by a Charge-Reversal Amphiphile." Molecular Pharmaceutics **8**(3): 758-766.

Zhou, R., B. Xiong, et al. (2011). "Slowed diffusion of single nanoparticles in the extracellular microenvironment of living cells revealed by darkfield microscopy." Analytical and Bioanalytical Chemistry **399**(1): 353-359.